Università degli Studi di Napoli "Federico II"

FACOLTÀ DI INGEGNERIA

Corso di Dottorato in Ingegneria dei Prodotti e dei Processi Industriali

LOOKING AT THE INTERFACE:
Novel Microscopy Techniques for Quantitative Phase Imaging in
Total Internal Reflection

COORDINATORE
CH.MO PROF. GIUSEPPE MENSITIERI

TUTOR
CH.MO PROF. GIUSEPPE MENSITIERI
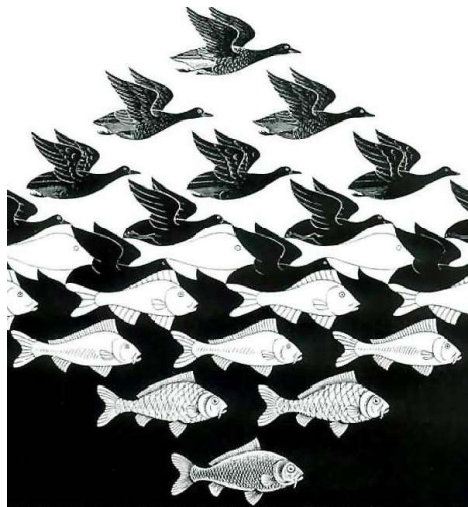DOTT. PIETRO FERRARO

CANDIDATO
BIAGIO MANDRACCHIA

LOOKING AT THE INTERFACE

Novel Microscopy Techniques for Quantitative Phase Imaging in Total Internal Reflection

BIAGIO MANDRACCHIA, PH.D.

UNIVERSITY OF NAPLES "FEDERICO II"
ENGINEERING OF INDUSTRIAL PRODUCTS AND PROCESSES

c. XXIX

SUPERVISORS
Dr. Pietro Ferraro
Prof. Giuseppe Mensitieri

ABSTRACT

Looking at the interfaces is very important for many biological and chemical applications: from the imaging of thin polymeric films to the study of cell/substrate interactions. Total Internal Reflection (TIR) microscopy and Surface Plasmon Resonance imaging (SPRi) are usually the preferred techniques when high sensitivity of measurement is required. They use super critical illumination to create evanescent waves at the sample/substrate boundary. The very short range of penetration of these evanescent waves allows to retrieve information about few hundreds of nanometers from the contact surface.

Evanescent wave microscopy has proven itself as a good tool for the characterization of thin films, cellular focal adhesions and biomolecular binding events. However, despite the high sensitivities achieved so far, each technique alone has a limited detection range with optimal sensitivity. The main goal of this work is to show how these techniques can benefit from the exploitation of the phase response of the evanescent waves, both in terms of sensitivity and reliability.

In this thesis we show the versatility of Digital Holography Microscopy for the development of innovative and compact systems for quantitative phase imaging and, in particular, the implementation of through-the-objective configurations for Holographic TIR microscopy and SPRi. Advantages, issues, and applications are discussed throughout the work. At the same time, possible implementations and future perspectives are also presented with the aim to show the potential and raise interest for the development of new techniques for label-free imaging of interfaces.

This thesis project was performed in the frame of a collaboration between the Department of Chemical Engineering, Materials, and Industrial Production, DICMaPI, and the Institute of Applied Sciences and Intelligent Systems, CNR - ISASI.

PUBLICATIONS

- Vittorio Bianco*, Biagio Mandracchia*, Valentina Marchesano, Vito Pagliarulo, Federico Olivieri, Sara Coppola, Melania Paturzo, and Pietro Ferraro. "Endowing a plain fluidic chip with micro-optics: a holographic microscope slide", *Light: Science Applications* (just accepted).

- Sara Coppola, Veronica Vespini, Federico Olivieri, Giuseppe Nasti, Michele Todino, Biagio Mandracchia, Vito Pagliarulo, Pietro Ferraro. "Direct self-assembling and patterning of semiconductor quantum dots on transferable elastomer layer". *Applied Surface Science* 12/2016, DOI:10.1016/j.apsusc.2016.12.071

- Biagio Mandracchia, Oriella Gennari, Valentina Marchesano, Melania Paturzo, Pietro Ferraro. "Label free imaging of cell-substrate contacts by holographic total internal reflection microscopy". *Journal of Biophotonics* 11/2016;, DOI:10.1002/jbio.201600177

- Biagio Mandracchia, Vito Pagliarulo, Melania Paturzo, Pietro Ferraro. "Surface Plasmon Resonance Imaging by Holographic Enhanced Mapping". *Analytical Chemistry* 03/2015; 87(8). DOI:10.1021/acs.analchem.5b00095

- Sara Coppola, Giuseppe Nasti, Biagio Mandracchia, Veronica Vespini, Simonetta Grilli, Pagliarulo Vito, Paola Pareo, Michele Manca, Luigi Carbone, Giuseppe Gigli, Pietro Ferraro. "Twofold Self-Assembling of Nanocrystals Into Nanocomposite Polymer". *IEEE Journal of Selected Topics in Quantum Electronics* 01/2015; PP(1-99)., DOI:10.1109/JSTQE.2015.2449657

CONTENTS

ACRONYMS

AS: Angular Spectrum

BS: Beam Splitter

CCD: Charge-Coupled Device

DH: Digital Holography

DHM: Digital Holography Microscopy

DMEM: Dulbecco's Modified Eagle Medium

EHD: Electro-Hydrodynamic

FFT: Fast Fourier Trasform

FOV: Field of View

HOLOTIR: Holographic Total Internal Reflection

HOLOSPRI: Holographic Surface Plasmon Resonance imaging

LOC: Lab-on-a-Chip

MEMS: Micro-Electro-Mechanical System

NA: Numerical Aperture

PDMS: Polydimethylsiloxane

SNR: Signal-to-Noise Ratio

TIR: Total Internal Reflection

TIRF: Total Internal Reflection Fluorescence

SPP: Surface Plasmon Polariton

SPR: Surface Plasmon Resonance

SPRI: Surface Plasmon Resonance imaging

THE STUDY of phenomena at the interface is a common topic for many fields of investigation, from chemistry to biology, to engineering. Its applications embrace the high-throughput characterization of thin polymeric structures, the monitoring of cell activity at the basal membrane, or the development of increasingly sensitive biosensors. An accurate three-dimensional mapping of a very thin layer (<100nm) at the boundary between two different dielectric media is a challenging task and often even the most accurate techniques of surface profilometry are not feasible. Along the years, many solutions have been proposed to face this problem. Nonetheless, there is not yet a single tool that can handle all the different demands. There is, instead, a plethora of available techniques, each one with a range of optimal applications.

Super-resolution techniques, such as confocal microscopy and ground state depletion microscopy, have reached lateral resolutions down to few nanometers but lose a lot of their resolving power in the third dimension. Furthermore, they are rather complex to set up and still severely low-throughput, which makes their use still impractical for many applications in the study of interfaces.

So far, the techniques of choice for the imaging of interfacial systems rely upon the formation evanescent waves. Evanescent waves have a very short penetration depth along the third dimension (from 70 to 250nm) and, conversely, a greater sensitivity for three dimensional mapping. We can think of evanescent wave microscopy as the ensemble of the imaging configurations that take advantage of this property of the evanescent wave to image a thin layer at the interface between two media. This is usually accomplished by super-critical illumination of the sample, Total Internal Reflection (TIR) microscopy or by exciting the collective motion of the electrons of a metal, Surface Plasmon Resonance imaging (SPRi).

The applications of evanescent wave microscopy can be divided in three big categories:

- study of the cell adhesion dynamics;

- mapping of surface features in thin films;

- measurement of binding kinetics.

All these subjects have in common the fact that they usually require the adoption of imaging techniques able to give quantitative information over a large area of the sample.

The temporary formation of adhesion contacts between cells and substrate is of considerable interest in the study of cell motility [1, 2], mechano-transduction [3–5] and

biocompatibility [6–8]. Furthermore, the determination of contact area is central in the understanding of how biomaterials properties influence cell adhesion [9]. As an example, blood contacting materials need to minimize platelet adhesion; conversely, the replacement and repair of tissues involve the adhesion of growth of cells within a polymeric matrix.

The cell membrane is usually separated from the supporting substrate by 100-150 nm. In the case of cell/substrate adhesion two different types of contacts have been described: focal contacts and close contacts [10–12]. Focal contacts are small regions (1μm width and 2–10μm length) where the cell membrane closely approaches the substrate in the range by 10–15 nm. In correspondence of close contacts, conversely, broad areas of a lamellipodium are separated from the substrate by 30 nm.

Fluorescence microscopy techniques such as epifluorescence and Total Internal Reflection Fluorescence (TIRF) Microscopy are now routinely performed to study many aspects of cellular biology. TIRF has been used extensively in the imaging of different systems, including single-molecule detection [13, 14], imaging endocytic and exocytotic events [15, 16] and analysis of cell–substrate interactions [9, 17].

However, it is important to be aware of some problems associated with these techniques [18–20]. Stable fluorescent labelling of nanostructures necessitates the development of new protocols, whereas the use of the label is invasive and induces risk of photobleaching and additional phototoxicity to the cell, making long-term studies harder to achieve. Clearly, there is a strong need for imaging cell/substrate and cell/colloidal particle interactions with high lateral and temporal resolution avoiding the incorporation of a fluorescent label.

Currently, the most used non-fluorescent technique for imaging cell–substrate contact is reflection interference contrast microscopy (RICM) [21–23]. RICM derives its contrast by interfering light reflected from the sample with a reference reflection from the sample cover slip or substrate [10, 24]. Nonetheless, interference contrast images of the interface are usually complicated by the reflection image of the cell body and its contents, thus allowing only a qualitative interpretation of the surface profile. In particular, semi-quantitative data interpretation is possible only where the thickness of cytoplasmic layer is at least 1μm [25] and a remarkable loss of sensitivity was demonstrated at small separation distances, up to 100 nm or more [26].

SPRi has proven itself another powerful tool to image subtle interfacial features by means of refractive index contrast. Studies of cell adhesion on gold or aluminium substrates have been performed taking advantage of the high resolution power of this technique in the axial direction [27, 28]. Lately, furthermore, applications to label-free tracking of cell features are seeing the light [29, 30]. In this framework, another implementation has seen the combination of SPRi with Raman spectroscopy in a SPRi-SERS platform [31, 32]. This is noteworthy because it compensates the lack of specificity of label-free imaging with Raman fingerprinting capability.
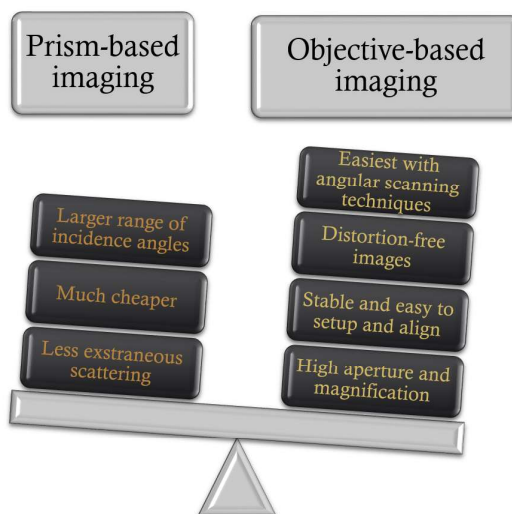
Prism-based systems are very easy to build but they imaging capabilities are fairly limited. They are, however, well suited for the development of sensors' prototypes.

SPRi, on the other hand, has seen a much wider application to characterize thin films or to read biomolecular binding events [33–35]. Many kinds of SPR imaging systems have been developed in order to obtain instruments for high-throughput analysis with low detection limits. The majority of the current SPRi methods can be divided into two groups, based on amplitude and phase contrast, respectively [36]. The amplitude contrast imaging methods detect the intensity distribution of the reflected light beam directly [37–40], while phase contrast imaging methods detect the interference pattern between the reflected beam and a reference beam [41–44]. Each technique has a different range of sensitivity and a different response to the same sample depending on the experimental conditions and, in general, one is more effective where the other is not.

Recently, it has been demonstrated that evanescent wave microscopy can take advantage of this complementarity of reflectivity and phase response. Taking simultaneous reflectivity and phase contrast images, it is possible to obtain more information about the sample and to address some critical problems, namely: i) the lack of sensitivity in the very short range (10-30nm) for TIR microscopy, and ii) the non bijective transfer function of SPRi that requires angular scanning to produce quantitative results.

Digital holography microscopy (DHM) is an interferometric technique that is normally used for quantitative phase imaging. The phase delay due to the presence of the sample induces a variation in the interferometric pattern produced with an appropriate reference beam. Numerical processing, then, is able to retrieve all the complex field of the light wave that passed through the object.

DHM is widely used for imaging of microstructures and biological systemsbecause of its excellent approach in obtaining intensity and quantitative phase information of a light-wave [45–50]. Prism-based configurations have been used to prove the suitability of DHM with TIR microscopy and SPRi [51–53]. Unfortunately, the physical constraint of the prism limits both numerical aperture and magnification of an imaging system. Hence, it yields a poor spatial resolution compared to that achievable with optical microscopy. Moreover, resolution in prism-based imaging is mainly governed by geometrical aberrations, which distort SPR images [54]. Finally, the prism also limits the compatibility with conventional microscopes and causes the images to move when the incident angle is changed, thus limiting the use of angular scanning techniques.

Starting from the concept of DHM, we have designed a Holographic TIR microscope for label-free quantitative phase imaging of total internal reflection. As a proof of concept, we studied the formation of focal contacts of fibroblasts on three substrates with different levels of affinity for cell adhesion. An improvement of HoloTIR detection sensitivity in comparison with standard TIR microscopy has been demonstrated.

We have also implemented an Objective-based Holographic SPRi microscope. This technique offers the possibility of simultaneous detection of reflectivity and phase changes in SPR images. It extends, thus, the range of detectable samples and, in particular, we have shown that it is possible to measure quantitatively thin film thickness without any angular or planar scanning, thanks to the complementary nature of the two contrast methods.

In comparison with previous works, we show that our through-the-objective designs avoid geometrical aberrations and limitations due to the use of a prism. Finally, the employment of configurations similar to the widely used objective-type TIR, and the modular design keep it compatible with conventional microscopes, paving the way for an easy implementation with other optical techniques, from standard bright field microscopy to fluorescence.

The thesis is organized as follows:

PART I reviews digital holography in general. The founding principles of interferometry and holographic recording are summarized in Chapter 1. DHM in particular, and the practical issues to avoid in order to obtain diffraction limited performance, are addressed in Chapter 2. Two applications developed in the course of the doctoral period are also presented.

PART II presents the work about HoloTIR microscopy. The phenomenon of TIR is detailed in Chapter 3. The properties of phase imaging of TIR and the specifics of HoloTIR setup are discussed in Chapter 4. This chapter also shows the application to cell adhesion studies of our system with enhanced accuracy.

PART III addresses the application of holography to SPRi. Chapter 5 explains the concept of surface plasmon resonce and reviews the state-of-art optical techniques for plasmon excitation. Chapter 6 is about the HoloSPRi microscope and the implications of the technique in terms of resolution and reliability of the measurement.

Part I

DIGITAL HOLOGRAPHY MICROSCOPY

THE BASICS OF DIGITAL HOLOGRAPHY

1

Optical holography consists of the acquisition of images from diffracted optical field measurements. Holographic imaging was initially proposed by Gabor [55] for electron microscopy. Holograms were recorded on high resolution photographic plates. Due to the subsequently-called in-line configuration, holograms were stained with twin-image and zero-order contributions, which overlapped with the signal image [56]. Originally recorded with the red radiation of Mercury lamps, holograms were increasingly recorded with laser light sources, which gave much more reliable results.

Holography is made of two separate steps: the recording of the hologram, and the object retrieval (also referred to as hologram reconstruction). In order to record the hologram of an object on a photographic plate, an interference has to be produced between two light waves derived from the same coherent source. A first wave is scattered by the object, while a second wave goes directly toward the recording surface and acts as a reference. Since the two waves are allowed to interfere, they form a fringe pattern on the photographic plate, i.e. the hologram. Since the intensity at any point in this interference pattern also depends on the phase delay of the object wave, the resulting hologram contains information on the phase as well as the amplitude of the object wave. The second stage is the formation of the object's image. If the hologram is illuminated once again with the original reference wave, it reconstructs the object wavefront.

In 1962, Leith and Upatnieks proposed to introduce an off-axis reference beam [57] to separate, in the spatial frequency domain, the real image from the twin-image and zero-order diffraction terms. However, holograms were still to be reconstructed by optical means.

The first digital reconstructions of optically measured holograms were realized by Goodman [58] and further by Kronrod [59] in the early 1970's. Here, optically magnified parts of the holograms are digitally sampled and then reconstructed using Fourier-transform based routines. Digitalization of optical holograms allowed, for instance, to improve reconstruction quality [60], to retrieve information about the phase of the recording wave [61, 62], and to treat holograms without reconstruction [63]. One of the major breakthroughs in holographic imaging was initiated, by Schnars, with direct recording

of digital holograms [64]. Charge-Coupled Device (CCD) and Complementary Metal Oxide Semiconductor (CMOS) digital sensor arrays enabled the acquisition and numerical processing of high-resolution holograms at fast rates.

Digital holographic microscopy (DHM) has become a technique utilized widely for sample inspection, having many applications in different fields of science and technology. The capability for recovering the complex amplitude distribution scattered by the sample permits a postacquisition numerical refocus and a quantitative measurement of the sample phase. These are two of the features that make DHM a very versatile microscopy technique. With the benefit of such special characteristics, DHM is used for particle tracking [65], micro-electromechanical systems (MEMS) characterization [66], and biological-samples inspection [67–69], among many other applications. The standard DHM system is based on a Mach–Zehnder interferometer that can be configured for operating in transmission or reflection modes, working in either the in-line or off-axis architecture.

1.1   OPTICAL FOUNDATIONS OF HOLOGRAPHY

1.1.1   *The wave equation*

Light is a transverse, electromagnetic wave characterized by time-varying electric and magnetic fields. Electromagnetic waves obey the Maxwell equations, from which is deduced the wave equation that describes the propagation of light. The wave equation for propagation of light in vacuum is:

$$\nabla^2 \mathbf{E} - \frac{1}{c^2} \frac{\partial^2 \mathbf{E}}{\partial t^2} = 0 \tag{1.1}$$

where E is the electric field strength, ∇^2 is the Laplace operator.

The wave may vibrate horizontally, vertically, or in any direction combined of these. Such effects are called polarization effects. Fortunately for most applications it is not necessary to use the full vectorial description of the fields, so we can assume a wave vibrating in a single plane. Such a wave is called plane polarized. For a plane polarized wave field propagating in the z-direction the scalar wave equation is sufficient:

$$\frac{\partial^2 E}{\partial x^2} - \frac{1}{c^2} \frac{\partial^2 E}{\partial t^2}. \tag{1.2}$$

It is easily verified that

$$E(z,t) = f(z - ct); \quad E(z,t) = g(z + ct) \tag{1.3}$$

are solutions to the equation. The equation (1.2) is a linear differential equation, then, for the *superposition principle*:

$$E(z,t) = \alpha f(z - ct) + \beta g(z + ct) \tag{1.4}$$

is likewise a solution to the equation.

The most important solution of (1.2) is the *harmonic wave*:

$$E(z,t) = \frac{1}{2} E_0 e^{i(kz - \omega t + \phi)}, \tag{1.5}$$

where E_0 is the real amplitude of the wave, the term $k_z - \omega t$ the phase of the wave; if we have not the maximum amplitude at $x = 0$ and $t = 0$, the relative phase is present. The wave number k is associated to the wavelength λ by the relation $k = 2\pi/\lambda$, while the angular frequency ω corresponds to the frequency f of the light wave by $\omega = 2\pi f$. Frequency f and the wavelength λ are related by the speed of light $c = \lambda f$.

A wavefront refers to the spatial distribution of the constant phase surfaces, as these surfaces propagate. The wavefronts are normal to the direction of propagation.

A notable waveform is the *plane wave*, whose wavefront is flat and orthogonal to the propagation direction for each given time t:

$$E(\mathbf{r},t) = E_0 e^{i(\mathbf{k}\cdot\mathbf{z} \mp \omega t + \phi)}. \tag{1.6}$$

According to the *Huygens principle*, each point on a propagating wavefront can be considered as radiating itself a spherical wave. Another relevant waveform often used in optics is, then, the *spherical wave*:

$$\frac{1}{r}\frac{\partial^2}{\partial r^2}(rE) - \frac{1}{c^2}\frac{\partial^2 E}{\partial t^2} = 0. \tag{1.7}$$

The wave equation can be described in polar coordinates (r, θ, ψ), transformed by $x = r\sin\theta\cos\psi$, $y = r\sin\theta sin\psi$, $z = r\cos\theta$. Due to the spherical symmetry, a spherical wave is not dependent on θ and ψ.

The only parameter of light directly measurable by sensors is the *intensity*. The intensity of light is defined as the energy flux per unit area per unit time:

$$I = \varepsilon_0 c E^2. \tag{1.8}$$

Since there is no sensor which can follow the frequency of light the only actually measurable quantity is the intensity integrated over the measuring time T_m:

$$I = \frac{\varepsilon_0 c}{T_m} \int_{t-T_m/2}^{t-T_m/2} E(r,\tau) E^*(r,\tau). \tag{1.9}$$

1.1.2 *Interference of light*

The basis of holography is the superposition of two or morecoherent light waves, namely the *interference.*

Let's consider in the following the superposition of two wave having the same wavelength, frequency, and polarization direction but differ in the directions (k_1 and k_2) and the phases (ϕ_1 and ϕ_2). The complex amplitude of the wave is given by

$$E_1(r,t) = E_0 \exp i(k_1 r - \omega t + \phi_1); \quad E_2(r,t) = E_0 \exp i(k_2 r - \omega t + \phi_2) \quad (1.10)$$

The whole complex amplitude is given by the sum of the individual amplitudes . The intensity thus becomes:

$$I(r) = (E_1 + E_2)(E_1 + E_2)^* = E_{01}^2 + E_{02}^2 + 2E_0^2 \cos^2(2k'r + 2\Delta\phi), \quad (1.11)$$

where $k' = (k_1 - k_2)/2$ and $\Delta\phi$ the difference between the two phases.

Consequently the resulting intensity is given by the intensity of the two beams (E_{01}^2 and E_{02}^2) plus a space varying interference term depending on the phase difference between the waves ($2E_0^2 \cos^2(2k'r + 2\Delta\phi)$). Intensity reaches its maximum (constructive interference) where

$$k'r + \Delta\phi = n\pi, \quad n \in \mathbb{Z} \quad (1.12)$$

and its minimum when (destructive interference)

$$k'r + \Delta\phi = (2n+1)\frac{\pi}{2}, \quad n \in \mathbb{Z}. \quad (1.13)$$

The resulting time independent pattern is called interference pattern. For plane waves the interference fringes whose spacing is equal to $\pi/|k'|$. The integer n is the inference order. An interference pattern consists then of dark and bright fringes as a result of the constructive and destructive interference.

We have discussed so far the case of two parallelly polarized waves. The complementary situation consists of orthogonally polarized waves: in this case there is no interference and the only effect of the superposition is the addition of the intensities $I(r) = E_{01}^2 + E_{02}^2$.

1.1.3 *Coherence*

The resulting intensity of two different sources, e. g. two electric light bulbs directed on a screen, is in general additive. Instead of dark and bright fringes as expected by Eq.(1.10) only a uniform brightness according to the sum of the individual intensities becomes visible. In order to generate interfere fringes the phases of the individual waves must be correlated in a special way . This correlation property is named coherence. Roughly

speaking, coherence is the ability of light to interfere. We can distinguish two aspects of this phenomenon, namely temporal and spatial coherence. Temporal coherence describes the correlation of a wave with itself at different instants. Spatial coherence, instead, depicts the mutual correlation of different parts of the same wavefront.

1.1.3.1 *Temporal coherence*

Temporal coherence describes the correlation of a wave with itself considering its behavior at different time instants. To better explain this concept, let's introduce the Michelson's interferometer, see Fig.1.1. A light source is splitted by the beam splitter BS, the two resulting beams are back-reflected by the mirrors M1 and M2, and superimpose on a screen. The two beams are usually not travelling exactly on the same direction but are slightly angled. On the screen a two-dimensional interference pattern is visible.

The optical path experienced by the two beams is respectively s_1 and s_2. In the experiment we can easily verify that the inference occurs only if the difference $s_1 - s_2$ does not exceed a certain length L, otherwise the inference pattern disappears and the resulting intensity showed will be the addiction of the incoming beams. This is due to the fact that interference fringes can only appear if the two waves have a well-defined phase relation. In fact the phase difference between waves emitted by independent sources varies randomly thus preventing the interference.

The atoms of the light source emit wave trains with finite length L. If the optical path difference exceeds this wave train length, the partial waves belonging together do not overlap on the screen and interference is not possible. This critical path length difference or, equivalently, the length of a wave train is named *coherence length*. The corresponding emission time for the wave train is the time of coherence is called *coherence time*.

By means of the formalism of Fourier a relation between the spectral width and the coherence length can be found

$$L = \frac{c}{\Delta f}. \tag{1.14}$$

Light having a long coherence length is named highly monochromatic. The coherence length is then a measure for the spectral width. The length of coherence of thermal light e.g. light bulbs is of the order of micrometers while some laser used for research aims have coherence light of hundredth of kilometers.

The visibility of the interference pattern is defined by

$$V = \frac{I_{max} - I_{min}}{I_{max} + I_{min}}. \tag{1.15}$$

Using equations (1.10) and (1.11), visibility can be redefined, considering $\Delta\phi = 0$ for I_{max} and $\Delta\phi = \pi$ for I_{min}:

$$V = \frac{2\sqrt{I_{max}I_{min}}}{I_{max} + I_{min}}. \tag{1.16}$$

In order to evaluate the self-coherence of E the following parameter is defined

$$\Gamma(\tau) = \langle E(t+\tau)E^*(t) \rangle = \lim_{T_m \to \infty} \frac{1}{T_m} \int_{-T_m/2}^{T_m/2} E(t+\tau)E^*(t)dt, \qquad (1.17)$$

where $E(t)$ and $E(t+\tau)$ are the two partial waves of the interferometer delayed of a time τ. The degree of coherence, thus, is defines as:

$$\gamma = \frac{\Gamma(\tau)}{\Gamma(0)}. \qquad (1.18)$$

Through simple calculation eq.(1.16) becomes

$$V = \frac{2\sqrt{I_{max}I_{min}}}{I_{max} + I_{min}} |\gamma|. \qquad (1.19)$$

The degree of coherence in then related to the contrast of the fringe pattern and so to the ability of the two beams to interfere. $|\gamma| = 1$ describes a monochromatic light i.e. a light with infinite length of coherence, while $|\gamma| = 0$ is related to a completely incoherent light. For partially coherent light $0 < |\gamma| < 1$.

1.1.3.2 *Spatial coherence*

The mutual correlation of different parts of the same wavefront is described by the spatial coherence. To define this property the Young's interferometer, in Fig.1.2, can be used. The light source is extended thus emitting light from different points. An aperture with two transparent holes is mounted between light source and screen. Under certain conditions, interference of the ray light coming from the upper and the lower hole are visible on the screen. The interference will be present if the distance between the holes will be keep lower than a critical limit, named coherence distance. This is due to the different optical path length for light rays emerging from different source points. Generally the contributions from all source points compensate themselves and the contrast vanishes. Nevertheless in some condition this compensation is avoided.

$$r_1 - r_2 < \frac{\lambda}{2}, \qquad (1.20)$$

where

$$r_1 = R^2 + \frac{(a-h)^2}{2}; \quad r_2 = R^2 + \frac{(a+h)^2}{2} \qquad (1.21)$$

and using the assumption that $a << R$ and $h << R$ eq.(1.20) becomes

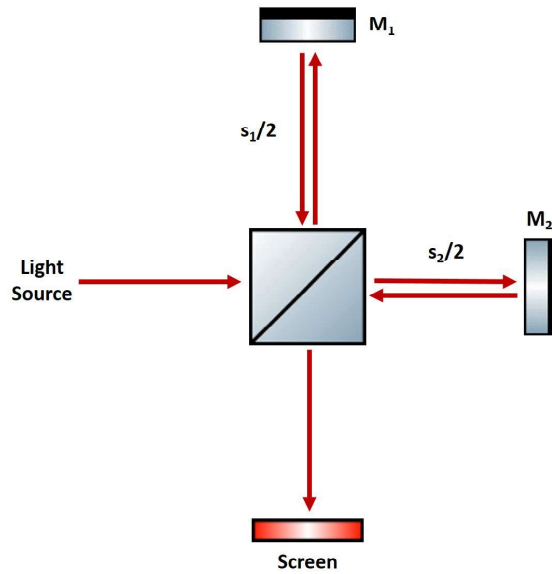$$r_1 - r_2 \approx \frac{ah}{2R} << \frac{\lambda}{2}. \qquad (1.22)$$

FIGURE 1.1: Schematic rapresentation of Michelson interferometer.
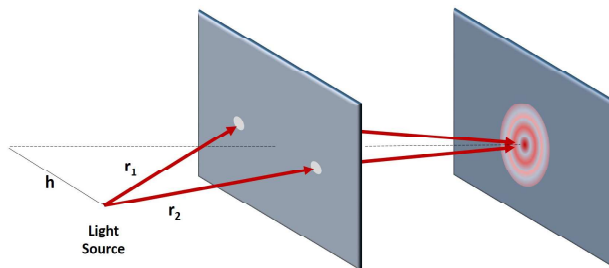

FIGURE 1.2: Schematic rapresentation of Young's interferometer

The coherence length a_k has then to fulfill the relation

$$\frac{ah}{2R} = \frac{\lambda}{2}. \tag{1.23}$$

The spatial coherence is thus not only a property of the light beam but it's depending on the geometry of the interferometer too. The general *spatio-temporal coherence function* is:

$$\Gamma(r_1, r_2, \tau) = \langle E(r_1, t + \tau)E^*(r_2, t) \rangle = \lim_{T \to \infty} \frac{1}{2T} \int_{-T}^{T} E(r_1, t + \tau)E^*(r_2, t)\mathrm{d}t \tag{1.24}$$

r1 and r2 being the spatial vectors of the two holes. The normalized cross function is, then:

$$\gamma(r_1, r_2, \tau) = \frac{\Gamma(r_1, r_2, \tau)}{\sqrt{\Gamma(r_1, r_1, 0)\Gamma(r_2, r_2, 0)}} \tag{1.25}$$

being $\Gamma(r_1, r_1, 0)$ and $\Gamma(r_2, r_2, 0)$ the intensity at $r1$ and $r2$. $\gamma(r_1, r_2, \tau)$ describes the degree of correlation between the light field at r_1 at time $t + \tau$ with the light field at r_2 at time t. $\gamma(r_1, r_2, \tau = 0)$ measures the correlation between the field amplitudes at r_1 and r_2 at the same time and is named complex degree of coherence.

1.2 DIGITAL HOLOGRAPHY

1.2.1 *Hologram formation*

In this section we will describe in detail the whole process of hologram formation and reconstruction in order to derive the relation between the real object field and the reconstructed field. Since the physical processes determining the hologram formation and the DH image reconstruction are linear, the sought relation has to assume the form of a convolution product [70].

Considering a reference system of coordinates $\{x, y\}$, attached to the principal surface of a real object, and a z-axis, perpendicular to this surface, that corresponds to the propagation direction of the diffracted light beam, we can model the holographic process as a Linear Space Invariant system (LSI) with an impulse response $T(x, y)$, transforming the real object signal $U(x, y)$ in the reconstructed field

$$U_R(x, y) = U(x, y) \otimes T(x, y), \tag{1.26}$$

where $\otimes$ is the spatial convolution operator. Processes of interference, diffraction, spatial integration, sampling and digital reconstruction determine the shape of the impulse response $T(x, y)$. Let

$$U(x, y) = |U(x, y)| \exp(j\varphi_U(x, y)) \tag{1.27}$$

be the complex wavefront produced in the plane (x, y) when the object is illuminated by a coherent beam. According to the diffraction theory [71], the diffracted field in a generic plane (x', y') orthogonal to the optical axis is expressed by the Rayleigh-Sommerfeld's integral as [72]:

$$O\left(x', y', d_0\right) = \frac{1}{j\lambda} \iint_{\mathbb{R}^2} U\left(x, y\right) \frac{exp\left(jk\rho\right)}{\rho} cos\Omega dx dy \,, \tag{1.28}$$

where λ is the source wavelength, d_0 is the distance between the planes (x, y) and (x', y'), i.e. the propagation distance of the diffracted wavefront, $k = 2\pi/\lambda$ is the wavenumber, $cos\Omega$ is the obliquity factor, usually set to unity due to the small angles assumption, and

$$\rho = \sqrt{d_0^2 + \left(x' - x\right)^2 + \left(y' - y\right)^2} \tag{1.29}$$

is the distance between a generic point in the plane (x', y') and a given point belonging to (x, y). If the Taylor series expansion of the square root formula in (1.29) is performed, excluding the terms of higher order than the first two, the distance ρ takes the form

$$\rho \approx d_0 \left(1 + \frac{1}{2} \frac{\left(x' - x\right)^2}{d_0^2} + \frac{1}{2} \frac{\left(y' - y\right)^2}{d_0^2}\right) \,, \tag{1.30}$$

which is valid under the assumption of large propagation distances, precisely when d_0 satisfies the Fresnel zone sufficient condition:

$$d_0^3 \gg \frac{\pi}{4\lambda} \left[\left(x' - x\right)^2 + \left(y' - y\right)^2\right]_{max}^2 \,. \tag{1.31}$$

Applying this approximation to the exponent of the spherical factor in (1.28) (which is the most critical factor due to the presence of the wavenumber amplifying approximation errors), while dropping all terms but the first in the denominator, the diffraction integral reduces to:

$$O\left(x', y', d_0\right) = \frac{j e^{j\frac{2\pi}{\lambda}d_0}}{\lambda d_0} \iint_{\mathbb{R}^2} U\left(x, y\right) exp\left\{j\frac{\pi}{\lambda d_0} \left[\left(x' - x\right)^2 + \left(y' - y\right)^2\right)\right]\right\} dx dy \,. \tag{1.32}$$

After some trivial manipulations, (1.32) can be written in terms of Fourier transform:

$$O\left(x', y', d_0\right) = \left|O\left(x', y', d_0\right)\right| exp\left[j\varphi\left(x', y', d_0\right)\right] = \\ = Z\left(x', y', d_0\right) \mathcal{F}\left\{U\left(x, y\right) W\left(x, y, d_0\right)\right\} \,, \tag{1.33}$$

where $\varphi\left(x', y', d_0\right)$ is the object phase signal, and we defined

$$\begin{cases} Z\left(x',y',d_0\right) = \frac{j}{\lambda d_0} exp\left\{\frac{2\pi}{\lambda}\left[d_0 + \frac{x'^2+y'^2}{2d_0}\right]\right\} \\ W\left(x,y,d_0\right) = exp\left\{\frac{j\pi}{\lambda d_0}\left(x^2+y^2\right)\right\} \end{cases} \tag{1.34}$$

Equation (1.33) well describes the relation between the wavefront in the object plane and the diffracted wavefront in whatever plane along the optical axis satisfying the sufficient condition in (1.31). This is a distribution of complex values, and both the amplitude and phase contain useful object information, depending on the acquisition configuration. However, any employable sensor can only register intensity distributions, so that a recording device placed in the plane (x',y') would only capture the 2D signal $|O\left(x',y',d_0\right)|^2$, thus losing the phase information. In order to recover the phase, this should affect in some way the recorded intensity distribution. Holography exploits the phenomenon of interference between two waves to code the phase information in an intensity signal, specifically as a modulated fringe pattern. Thus, a reference wave has to be introduced to allow interference with the object wave. Let

$$R\left(x',y',d_0\right) = a_R exp\left\{j2\pi(u_R x' + v_R y') + j\Gamma\left(x',y'\right)\right\} \tag{1.35}$$

be the reference wave in the acquisition plane (x',y'), modeled as a plane wave oscillating with spatial frequencies u_R and v_R. In (1.35), $\Gamma\left(x',y'\right)$ represents the wavefront aberration factors in the acquisition plane (x',y'). The object wave interferes with the reference in the recording plane to produce the hologram

$$\begin{aligned} H\left(x',y',d_0\right) &= \left|O\left(x',y',d_0\right) + R\left(x',y'\right)\right|^2 = \\ &= \left|O\left(x',y',d_0\right)\right|^2 + \left|R\left(x',y'\right)\right|^2 + \\ &\quad + R^*\left(x',y'\right)O\left(x',y',d_0\right) + R\left(x',y'\right)O^*\left(x',y',d_0\right), \end{aligned} \tag{1.36}$$

where * denotes the conjugate operator. In the right hand side of (1.36), four terms are present, that are usually called the diffraction orders. The first two terms are only intensity signals, of little interest because the phase information is lost due to the square module operation. These can be grouped in a signal

$$D_0(x',y',d_0) = \left|O(x',y',d_0)\right|^2 + \left|R(x',y')\right|^2 \tag{1.37}$$

referred to as the zero-th diffraction order. The third and the fourth term are the +1 and -1 orders of diffraction, hereafter denoted with $H^{+1}\left(x',y',d_0\right)$ and $H^{-1}\left(x',y',d_0\right)$ and representing the real image and the virtual image of the object respectively. Applying (1.35), the +1 order takes the form:

$$\begin{aligned} H^{+1}\left(x',y',d_0\right) &= R^*\left(x',y'\right)O\left(x',y',d_0\right) = \\ &= a_R\left|O\left(x',y',d_0\right)\right|\exp\left[j\varphi\left(x',y',d_0\right)\right]\exp\left[-j2\pi\left(u_R x' + v_R y'\right) - j\Gamma\left(x',y'\right)\right] \end{aligned} \tag{1.38}$$

Since it results $H^{+1}(x',y',d_0) = \{H^{-1}(x',y',d_0)\}^*$, we can rewrite (1.36) in a different form

$$
\begin{aligned}
H(x',y',d_0) &= \\
&= D_0(x',y',d_0) + H^{+1}(x',y',d_0) + H^{-1}(x',y',d_0) = D_0(x',y',d_0) + \\
&+ 2a_R \left| O\left(x',y',d_0\right) \right| \cos\left\{2\pi\left(u_R x' + v_R y'\right) + \Gamma\left(x',y'\right) - \varphi\left(x',y',d_0\right)\right\},
\end{aligned}
\tag{1.39}
$$

where it is apparent that the amplitude and phase of the object wave are encoded as amplitude and phase modulation, respectively, of a set of interference fringes equivalent to a carrier with spatial frequencies u_R and v_R. This gives us a good chance to recover the phase. The spatial frequencies are proportional to the angles between the reference and the object beam, $(\theta_x,\ \theta_y)$, according to the relation

$$
u_R = \frac{\sin\theta_x}{\lambda} \ ; \ v_R = \frac{\sin\theta_y}{\lambda} \ .
\tag{1.40}
$$

This clarifies the advantage of using an off-axis configuration because, if the angles $(\theta_x,\ \theta_y)$ are large enough, the three diffraction orders can be properly separated [57].

1.2.2 Digital recording of holograms

The aim of digital holography is the recording of holograms by digital sensors, e.g. CCDs or CMOS cameras. Such holograms can be, then, stored in a computer and numerically reconstructed. The recording process is the sampling of an interference pattern consisting of spatial frequencies, the highest of which is given by the largest angle between object and reference wave. The limited resolution of the CCD chip and similar digital devices decides the maximum frequency allowed for sampling and severely restricts the experimental set-up configuration, see Fig.1.3.

Let's consider a square CCD array of $N \times N$ pixels, and be $\Delta\xi$ and $\Delta\eta$ the pixel pitch in the x and y direction, respectively. Assuming $\Delta\xi = \Delta\eta$, we can restrict the analisys to the x-z plane only. The distance p between two consecutive interference fringes forming the hologram at H is:

$$
p = \frac{\lambda}{2\sin\left(\frac{\theta}{2}\right)} ,
\tag{1.41}
$$

where θ is the angle between the reference beam and the object wave emitted by a point P.

A meaningful sampling of the intensity distribution constituting the hologram is dictated by the *sampling theorem*. This requires that the period p must be sampled with more than two pixels, see Fig.1.4:
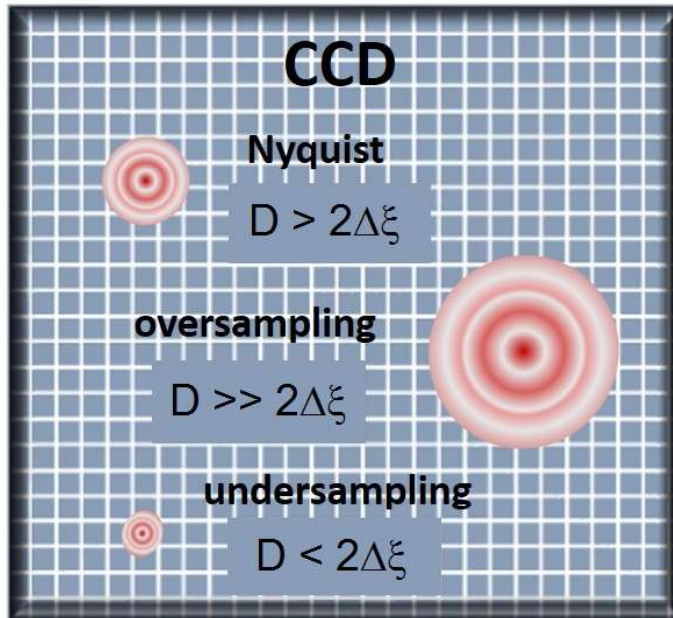
$$
p > 2\Delta\xi .
\tag{1.42}
$$

FIGURE 1.3: The discrete resolution of CCD cameras limits the sampling of the signal. Experimental parameters should be adjusted in order to obtain the most efficient configuration. This happens when the smallest resolvable object is sampled accordingly to Nyquist criterion.
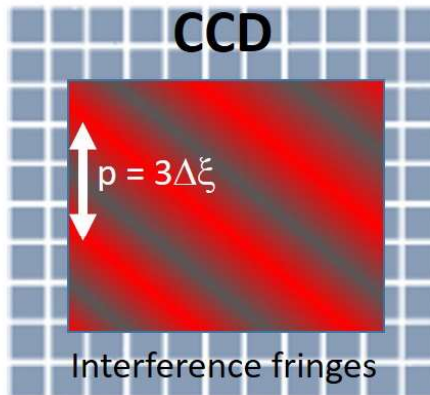

FIGURE 1.4: Interference fringes should be sampled by at least two pixels. Maximum optimization of the setup would require $p = 2\Delta\xi$. For any practical purpose, however, a good practice is setting the fringes' period to thrice the pixel size: $p = 3\Delta\xi$.

This can be expressed using the spatial frequency f of the holographic fringes:

$$f < \frac{1}{2\Delta\xi} \, . \tag{1.43}$$

In practical applications the CCD array is given, and it sets a limit to the the angle θ:

$$\theta \leqslant \arcsin\left(\frac{\lambda}{2\Delta\xi}\right) \approx \frac{\lambda}{2\Delta\xi}, \tag{1.44}$$

because θ in general remains small.

Further geometrical evaluations lead to the conclusion that if the distance d_0 between the CCD and the object is

$$d_0 = \frac{2p_x}{\lambda}D \, , \tag{1.45}$$

where D is the width of the object, the maximum bandwidth is obtained without violating the sampling theorem. This is prominent of the crucial role that pixel size plays in digital holography and imaging in general.

1.3 NUMERICAL RECONSTRUCTION

Digital reconstruction of an hologram consists in a *a posteriori* refocusing over the original object, which can be performed by calculating backward propagation of the light from the hologram to the reconstruction plane. This process is equivalent to positioning the recorded hologram back into the reference beam.

Under Fresnel approximation, the complex wavefront reconstructed in a plane (x_R, y_R), at a generic distance d from the hologram plane, (x', y'), can be written as:

$$C(x_R, y_R, d) = \frac{je^{j\frac{2\pi}{\lambda}d}}{\lambda d} \iint\limits_{\Sigma_0} R(x', y') H(x', y') e^{\left\{j\frac{\pi}{\lambda d}\left[(x_R - x')^2 + (y_R - y')^2\right]\right\}} dx'dy', \tag{1.46}$$

that can be rearranged in terms of a Fourier transform:

$$\begin{aligned} C(x_R, y_R, d) &= Z(x_R, y_R, d) \, \mathcal{F}\left\{R(x', y')H(x', y')W(x', y', d)\right\} = \\ &= \mathcal{F}r\{H; d\}. \end{aligned} \tag{1.47}$$

The operation described in the right hand side of (1.46) is generally referred to as the Fresnel transform, $\mathcal{F}r\{H; d\}$, or the hologram propagation. Similarly, the reconstruction method that adopts the formulation written above is called the Fresnel method. The reconstructed wavefront $C(x_R, y_R, d)$ is a complex field containing the three diffraction

orders, propagated at distance d, from which the intensity and the phase signals can be extracted:

$$I(x_R, y_R, d) = C(x_R, y_R, d) \, C^*(x_R, y_R, d)$$

$$\Psi(x_R, y_R, d) = \tan^{-1} \frac{Im\{C(x_R, y_R, d)\}}{Re\{C(x_R, y_R, d)\}}, \tag{1.48}$$

where $Im\{\ldots\}$ and $Re\{\ldots\}$ respectively take the imaginary part and the real part of a complex signal. If d is the object best-focus distance for the given optical system used to capture the hologram, then the signal $C(x_R, y_R, d)$ is the object image reconstruction. However, direct implementation of (1.46) is a time consuming process and more efficient computational schemes can be designed to implement digital holographic reconstruction.

It possible to separate reconstruction methods into two main families:

- the Fourier based approaches, based on the use of a single fast Fourier transform (FFT);

- the convolution methods, computed by using two or three FFTs.

It can be seen that Fourier based approaches are well suited for imaging extended objects localized far from the CCD or CMOS sensor. Convolution methods, on the other hand, are well adapted for the reconstruction of holograms, of small lateral dimensions, recorded near the imaging device. This makes them especially suitable to the case of digital holography microscopy. Alternative methods can be considered when an adjustable magnification or advanced filtering techniques are needed but they fall outside the scope of this book.

1.3.1 *Convolution method*

A different way to demodulate the object distribution is to think to the Rayleigh-Sommerfeld diffraction formula as a convolution integral, i.e.

$$C(x_R, y_R, d) = \frac{1}{j\lambda} \iint\limits_{\Sigma_0} R(x', y') \, H(x', y') \, \frac{\exp(jk\rho_R)}{\rho_R} \cos\Omega \, dx' dy' =$$

$$= \iint\limits_{\Sigma_0} R(x', y') \, H(x', y') \, g(x_R - x', y_R - y'; d) \, dx' dy' = \tag{1.49}$$

$$= [R(x', y')H(x', y')] \otimes g(x', y'; d)$$

where

$$g(x', y'; d) = \frac{1}{j\lambda} \frac{\exp(jk\rho_R)}{\rho_R} \cos\Omega \approx \frac{1}{j\lambda} \frac{\exp jk\sqrt{d^2 + x'^2 + y'^2}}{\sqrt{d^2 + x'^2 + y'^2}} \tag{1.50}$$

is the Point Spread Function (PSF) of the diffraction process from the hologram plane to the reconstruction plane under Fresnel approximation, and ρ_R is the distance between a generic point in the plane (x', y') and a given point belonging to (x_R, y_R). Standing the convolution property of the $\mathcal{F}\{\dots\}$ operator, the diffracted wavefront is given by:

$$C_{conv}(x_R, y_R, d) = \mathcal{F}^{-1}\left\{\mathcal{F}\left\{R(x', y')H(x', y')\right\}\mathcal{F}\left\{g(x', y'; d)\right\}\right\}_{(x_R, y_R)}, \quad (1.51)$$

which can be numerically calculated by three FFTs. Hence, the digital wavefront reconstructed at distance d using the convolution method takes the form

$$C_{conv}\left(n\rho_{Cx}, m\rho_{Cy}, d\right) =$$
$$= \mathcal{FFT}^{-1}\left\{\mathcal{FFT}\left\{R_s\left(kp_x, lp_y\right)H_S^{+1}\left(kp_x, lp_y\right)\right\}\mathcal{FFT}\left\{g\left(kp_x, lp_y; d\right)\right\}\right\}, \quad (1.52)$$

where $G = \mathcal{FFT}\{g; d\}$ has a known distribution independent on the input hologram, and can be calculated just once for a more rapid computing:

$$G = \mathcal{FFT}\{g; d\} = \exp\left\{\frac{j2\pi d}{\lambda}\sqrt{1 - \frac{\lambda^2\left(n + \frac{N_x^2 p_x^2}{2\lambda d}\right)^2}{N_x^2 p_x^2} - \frac{\lambda^2\left(m + \frac{N_y^2 p_y^2}{2\lambda d}\right)^2}{N_y^2 p_y^2}}\right\}. \quad (1.53)$$

Noteworthy, differently from the Fresnel method, the convolution method yields a wavefront reconstruction with pixel pitches independent on the propagation distance, i.e.

$$\begin{cases} \rho_{Cx} = p_x \\ \rho_{Cy} = p_y \end{cases}. \quad (1.54)$$

This is an advantage of the convolution method with respect to the Fresnel strategy, as no resolution loss occurs when the reconstruction distance increases. On the other hand, the price to pay is an increase of the computational time required for calculating three FFTs.

1.3.2 Angular Spectrum method

Both the Fresnel and the convolution method discussed above are valid under Fresnel approximation, which stands for propagation distances higher than the threshold value reported in (1.31). In practice, this limits the minimum reconstruction distance. A way

to avoid the limitations deriving from the Fresnel approximation is to adopt the Angular Spectrum (AS) method. Considering the hologram plane located in the origin of the optical axis, $z = 0$, the AS of the hologram $H(x', y', z = 0)$ in this plane is given by

$$G_A(k_x, k_y, 0) = \iint\limits_{\Sigma_0} H(x', y', 0) \, e^{[-j(k_x x' + k_y y')]} dx' dy' = \mathcal{F}\{H(x', y', 0)\}_{(k_x, k_y)},$$

(1.55)

where we indicated with k_x and k_y the spatial frequencies corresponding to x' and y', respectively. As discussed above, if the spatial carrier is properly adjusted, the three diffraction orders are spatially separated in the AS domain and the +1 order can be extracted by band-pass filtering the signal G_A. We will indicate with G_A^{+1} the version of the AS obtained after filtering out the diffraction orders out of interest, and we will refer to $H^{+1}(x', y', 0)$ as the object signal in the plane $z = 0$. This can be rewritten as the inverse Fourier transform of its filtered AS, i.e.

$$H^{+1}(x', y', 0) = \iint\limits_{\Sigma_0} G_A^{+1}(k_x, k_y, 0) \exp\left[+j(k_x x' + k_y y')\right] dk_x dk_y.$$

(1.56)

The exponential function $exp\left\{j(k_x x' + k_y y')\right\}$ can be thought as the projection onto the plane $z = 0$ of a plane wave propagating along the optical axis with a wave vector

$$k = \left(k_x, k_y, k_z = \sqrt{k^2 - k_x^2 - k_y^2}\right)$$

(1.57)

Thus, the wavefront propagated from the hologram plane to the reconstruction plane can be written as

$$C_{AS}(x_R, y_R, z) = \iint\limits_{\Sigma_0} G_A^{+1}(k_x, k_y, 0) \exp\left[+j(k_x x' + k_y y' + k_z z)\right] dk_x dk_y =$$

$$= \iint\limits_{\Sigma_0} \left[\mathcal{F}\{H^{+1}(x', y', 0)\}_{(k_x, k_y)} \exp(jk_z z)\right] \exp\left[+j(k_x x' + k_y y')\right] dk_x dk_y =$$

$$= \mathcal{F}^{-1}\left\{\mathcal{F}\{H^{+1}(x', y', 0)\}_{(k_x, k_y)} exp(jk_z z)\right\}_{(x_R, y_R)}.$$

(1.58)

If z=d is the object best-focus distance, then C_{AS} is the DH reconstruction of the object. This can be numerically obtained by calculating two FFTs, so that the numerical image reconstruction at distance d using the AS method is given by:

$$C_{AS}(n\rho_{ASx}, m\rho_{ASy}, d) = \mathcal{FFT}^{-1}\left\{\mathcal{FFT}\left\{H_S^{+1}(kp_x, lp_y, 0)\right\} exp(jk_z d)\right\},$$

(1.59)

where

$$
\begin{cases}
\rho_{ASx} = p_x \\
\rho_{ASy} = p_y
\end{cases}
\tag{1.60}
$$

are the pixel pitches in the reconstruction plane, which are independent on the propagation distance, similarly to the convolution method. Noteworthy, the AS method allows to save one FFT with respect to the convolution method and, above all, this works for short propagation distances too.

OFF-AXIS DIGITAL HOLOGRAPHY MICROSCOPY

D igital holographic microscopy (DHM) has become a technique utilized widely for sample inspection, having many applications in different fields of science and technology. The capability for recovering the complex amplitude distribution scattered by the sample permits a post-acquisition numerical refocus and a quantitative measurement of the sample phase. These are two of the features that make DHM a very versatile microscopy technique. The applications of DHM span from particle tracking [65], microelectromechanical systems (MEMS) characterization [66], to biological samples inspection [67–69].

Standard DHM systems are based on a Mach-Zehnder interferometer. Configurations for operating in transmission or reflection modes have been developed for either the inline and off-axis architecture. For the purposes of this book we will address in detail only off-axis architecture, for a more detailed overview of in-line holography see [73, 74].

A regular imaging microscope is formed by an *infinity-corrected* microscope objective and a *tube lens*. The distance between objective and tube lens can change the curvature of the incoming wavefront. The presence of the objective alone introduces a phase distortion. In conventional light microscopy, where just the irradiance is captured, this spherical phase factor has no effect on the imaging process. However, this phase distortion can produce unwanted effects not only in the retrieved phase of the sample but also in the conditions of recording of the digital hologram to achieve diffraction-limited DHM.

Many works have been performed in recent years in order to compensate this phase factor, both numerically and physically . Computational methods are widespread and commonly used for compensating the all the defects introduced by the optical components in DHM systems [75–80]. In spite of the correction produced in the phase images, those methods cannot avoid the fact that such phase curvature is physically present in the imaging system during the recording process. This presence produces ruining effects that cannot be removed by computational methods. Nevertheless, some design precautions minimize or even eliminate the phase curvature introduced by the imaging system in DHM.

2.1 DESIGN PARAMETERS TO OPERATE AT DIFFRACTION LIMIT

In off-axis DHM the sample information is encoded in the $+1$ and -1 diffraction orders. This feature imposes the need for separating them from the DC diffraction order. The spreading of the diffraction orders, then, limits the utilization of the space bandwidth of the hologram. For this reason it is necessary to study how the design of the optical arrangement influences the shape and the size of those terms.

The diffraction-limit performance of the DHM can be achieved whatever wavefront curvature is chosen for the object wave, provided that the proper spatial filtering of the DC, $+1$, and -1 diffraction orders is possible.

However, to make possible the proper spatial filtering, no overlapping of the diffraction orders has to be guaranteed. In the case in which the orders are overlapped, $+1$ and -1 diffraction orders cannot be isolated completely from the DC term, which introduces noises and contrast variations in the reconstructed holograms.

Let us study the case of a plane wave coming out from the microscope (infinite curvature radius), Fig.2.1. To establish the optimal conditions to make the best use of the space bandwidth, let us consider a circular pupil function of r radius measured in the pupil plane. Mathematically, the pupil function appearing in the Fourier space is

$$p(\lambda f \mathbf{u}) = \text{circ}\left(\frac{\lambda f}{r}|\mathbf{u}|\right) . \tag{2.1}$$

The radius of the pupil function in the Fourier space is $\rho = r/(\lambda f)$. The radius of the pupil written as a function of NA and lateral magnification of the objective is $\rho = NA/(\lambda M)$ [81], see Fig.2.2. From the consideration of this size, it is possible to select the appropriate objective that can be utilized in a particular DHM setup, such that the use of space bandwidth is optimized.

Given a square camera with $N \times N$ pixels of size $\Delta \xi \times \Delta \xi$, the maximum space bandwidth is utilized to record the whole information of the wave-field if:

$$\rho \leq \frac{1}{\sqrt{2}(3+\sqrt{2})\Delta\xi} . \tag{2.2}$$

which leads to:

$$\frac{NA}{M} \leq \frac{\lambda}{\sqrt{2}(3+\sqrt{2})\Delta\xi} . \tag{2.3}$$

This condition assumes complete separation between the diffraction orders. Such separation is achieved choosing the proper value of the angle between the reference and the object waves, which should be satisfy the relation:

$$\arcsin\left(\frac{3}{2\sqrt{2}\pi}\frac{NA}{M} \leq \theta \leq \frac{\lambda}{2\Delta p}\right). \tag{2.4}$$
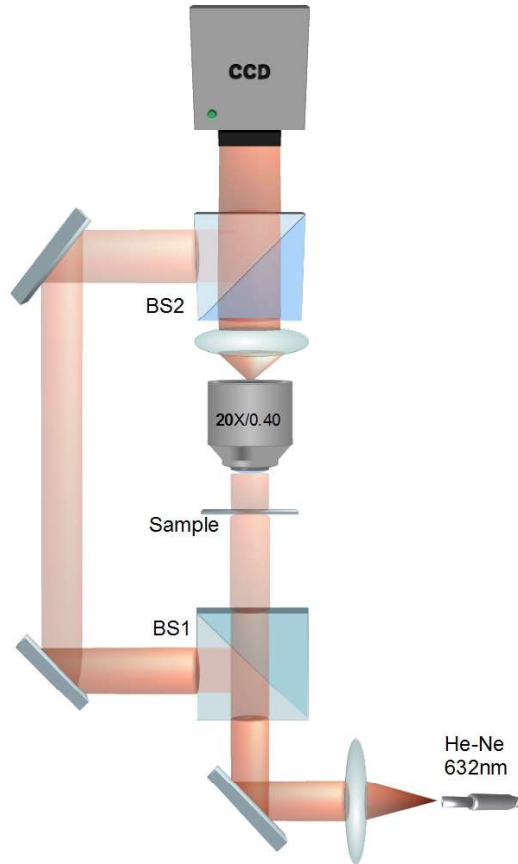
FIGURE 2.1: Schematic representation of a DHM setup. In this configuration the illumination laser coming out from a fiber is divided by Beam-splitter cube (BS). Part of the light impinges on the sample and then is collected by a microscope objective. A tube lens collimates the light from the objective before this encounters the reference beam on the camera plane. Here the interference pattern is recorded by a CCD camera. The difference of optical path between the two beams must be lower then the coherence of the laser.
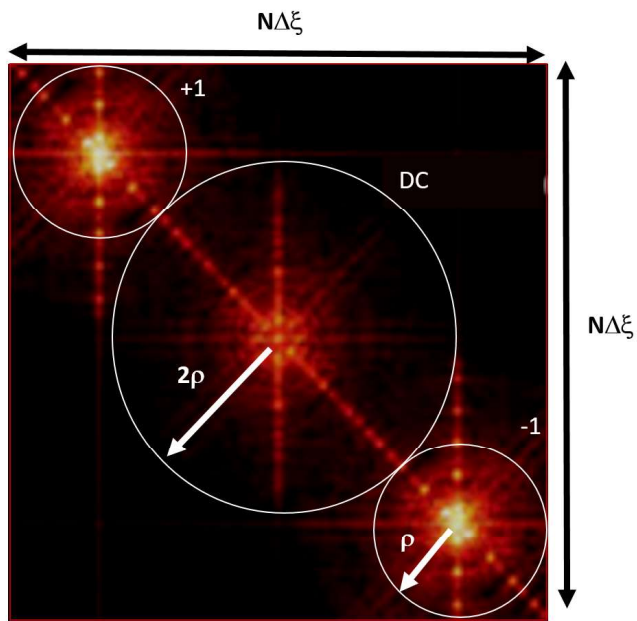
FIGURE 2.2: Fourier transform of the digital hologram. The sizes and shapes of diffraction orders are illustrated. The DC diffraction order is placed at the center of the Fourier spectrum of the digital hologram; its size indicates the achievable resolution of the DHM. The shape and size of the +1 an -1 diffraction orders are controlled by the value of the wavefront curvature

Whenever the condition states on (2.3) and (2.4) are met, the DHM can be considered as diffraction limited because there is enough space bandwidth in the Fourier domain for filtering the diffraction orders without losing spatial frequencies or introducing noise.

These calculations are valid whenever the recorded wavefront is a plane wave, which is the case of in-focus acquisitions when using an infinity corrected microscope objective. When this is not possible, however, diffraction limited performance can be maintained provided that the radius of curvature C satisfies the relation:

$$C \geq \left(\frac{\sqrt{2} N \Delta \xi}{2 \lambda \rho} \right).$$
(2.5)

In summary, the higher the curvature, the better the resolution of the microscope.

2.2 APPLICATION I: MICROLENS CHARACTERIZATION

Microlenses are nowadays being incorporated in many devices with a large area of application fields. In the recent years, a lot of commercial applications such as optoelectronics, photonic and biomedical devices, as well as image processing require the fabrication of adaptive and adjustable microlens array. For that reason a lot of attempts have been conducted in order to support the growing interest in the production of lens arrays for sensors or optical communications devices for parallel data transmission.

Several fabrication techniques and a large variety of process have been proposed for polymer based microlenses but the preparation of moulds, masks or metal layers with very accurate dimensions and shapes is generally required. The drawbacks and the rigidity of template-based manufacturing processes strongly stimulated the investigation of alternative and direct approaches such as those based on printing techniques. A novel nozzle-less approach the fabrication of tunable size microlens arrays exploits the pyro-electrohydrodynamic (Pyro-EHD) effect activated onto a ferroelectric crystal (Lithium Niobate) [82], see Fig.2.3.

The pyro-dispensing process shows great flexibility making possible the formation of polymer microlens arrays overpassing the viscosity border of the conventional ink-jet printing systems. Controlling the experimental parameters tunable arrays of microlenses can be produced in a direct way. To improve the printing process in terms of precision and ink properties, a study of the optical and geometrical features is due. Using non-interferometric microscopy we can estimate the optical performances of the micro-elements but we cannot obtain quantitative details. Such properties were characterized by DHM inspection. This can show even small defects that could remain unnoticed otherwise.

The sample was put into the object arm of a Mach-Zehnder interferometer, provided with a continuous laser source emitting at a wavelength of 532nm. The light coming from the array is collected by a microscope objective while, the interference patterns with a
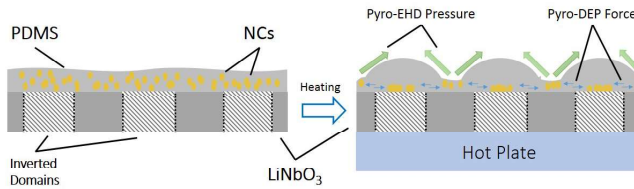
FIGURE 2.3: Cartoon depicting the process of microlens fabrication by Pyro-EHD. A layer of PDMS is spun on top of a poled crystal of Lithium Niobate. Heating the crystal generate a movement of charges and the consequent formation of microlenses in correspondence of the inverted domains.

reference beam are captured by a CCD camera. By appropriate numerical manipulation of the interferograms recorded by the CCD it is possible to obtain the wavefront curvature transmitted by the sample at a given distance. We report here an interferometric analysis focusing the attention on three microlens arrays fabricated at 4.000, 6.000 and 8.000 rpm, respectively.

Microlenses surface profiles and geometrical properties have been reconstructed by transmission plane-wave test. The lens surface profiles were reconstructed from the wavefront curvature at the image plane, the interferometric technique used was based on Digital Holography in microscope configuration set-up [83, 84]. We have recovered the geometrical parameters by fitting the wavefront curvature as depicted in Fig.2.4, where the focal length is calculated from the radius of curvature of the wavefront. Moreover it is important to note that the shape of the lens is not perfectly spherical especially those spinned at 4.000 and 8.000 rpm. In both cases the shape deviates from a sphere having a slight concave surface at the centre, see Fig.2.4 and 2.5. It seems possible that these concave profiles are due to the kinetic behavior of slowly solvent evaporation process in the droplet and it is well known in literature [85].

2.3 APPLICATION II: ON-CHIP DH MICROSCOPY

Lab-on-a-chip (LoC) devices are extremely promising to bring diagnostic functions at the point-of-care. The LoC paradigm can be resumed in the will to emulate all the functionalities of a modern analysis lab onboard a portable platform, or at least a compact system, realizable at contained costs. At this scope, an important goal is the design of imaging schemes able to work out of the lab.
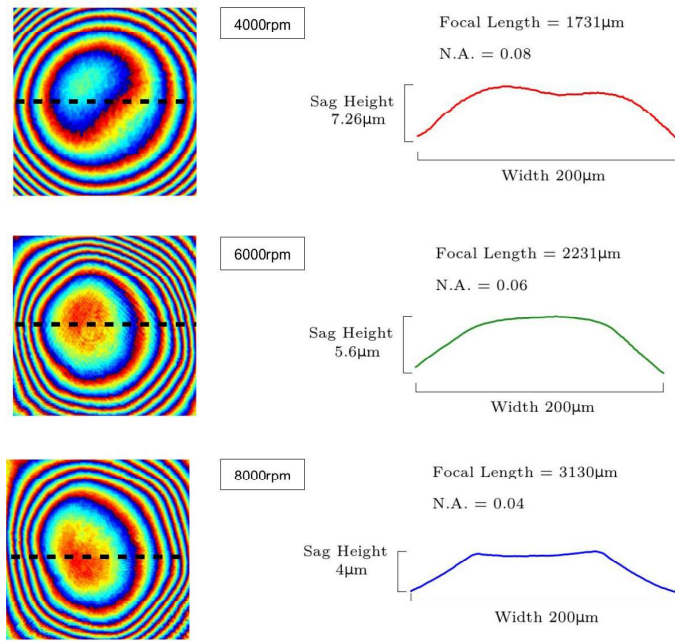
FIGURE 2.4: Optical characterization of PDMS microlenses. Three lenses spun at different velocities are shown. From the phase profiles (right) it is possible to retrieve the shape of the microlenses and quantify the optical parameters.
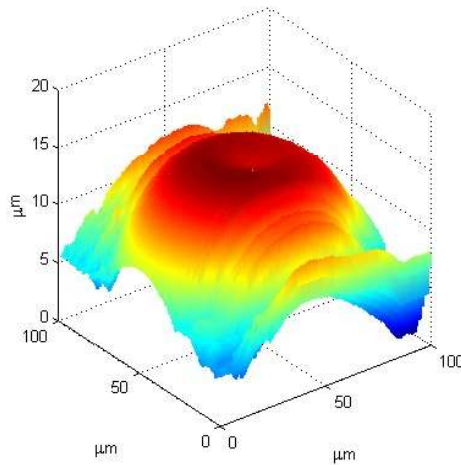
FIGURE 2.5: 3D representation of the unwrapped phase profile of a microlens (4000rpm).

The Optofluidic microscope introduced in 2006 represented a cutting-edge novelty in this direction, overcoming the resolution limits imposed by the finite size of the CCD recording elements [86]. However, phase-retrieval was not allowed, thus impairing the access to quantitative information.

On-chip flow cytometry of leukocyte cells was demonstrated with the design of a compact Digital In-Line Holography (DILH) microscope using a pulsed, fiber-coupled laser source [87], and since then a number of approaches based on DILH have been proposed. However, every strategy based on DILH, such as Holographic Optofluidic Microscopy, uses iterative algorithms to solve the twin image problem. However, these algorithms do not always guarantee the convergence to a solution, DILH-based techniques turn out not to be quantitative in a number of practical situations [88, 89]. Furthermore, the lensless approach constitutes an inner limitation to the available resolution.
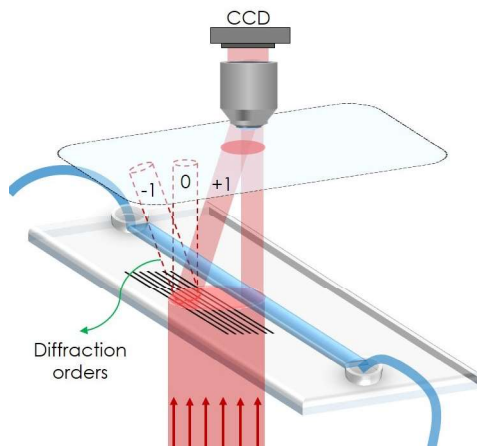
FIGURE 2.6: Representation of the wavefront division scheme used to develop the on-chip off-axis DH microscope

To get rid of the shortages deriving from the twin image superposition, here we propose the use of off-axis Digital Holography in place of the in-line configuration, and instead of avoiding the use of lenses, we show an alternative lens-based approach that integrates the imaging functions onboard chip[90].

Here we show a pocket module that allows performing off-axis Digital Holography microscopy with no need for an interferometer setup. We have engineered a commercial plastic chip for the scope, see see Fig.2.6. Our strategy is moving the complexity from the reconstruction algorithms and the external imaging apparatus to the chip itself, using custom optical components. We functionalized the chip with a photoresist grating and polymer lenses, to avoid the need for a reference arm of the interferometer as well as external optical components. Thanks to the single beam scheme, the system is robust
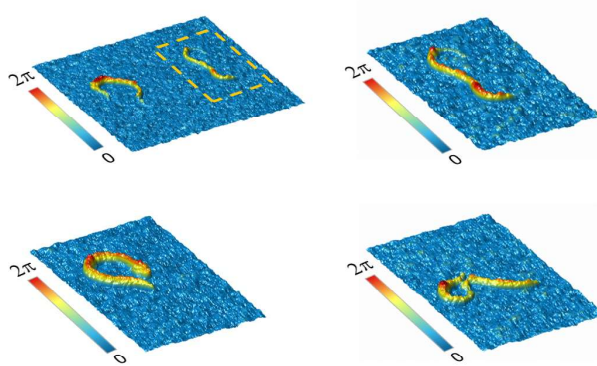
FIGURE 2.7: a) Phase maps of two early stage *C. elegans* worms. b-d) Time-lapse of the area in the dashed rectangle in a).

against vibrations and the stability of fringe patterns implies enhanced portability. Label-free imaging and quantitative phase contrast mapping of live samples is demonstrated, along with flexible refocusing capabilities. Thus, a liquid volume can be analyzed in one single shot, with no need for mechanical scanning systems.

The system can be used to perform DHM with a normal microscope or even as a standalone device. Phase imaging of live *C. elegans* worms at early embryonal stage is shown in Fig.2.7. In this case the sample was magnified using a 20x microscope objective and a 1:2 relay lens to form the image on the camera plane. The final magnification was 10x.

A sketch of the standalone setup is shown in Fig.2.8a, which illustrates the working principle. Pictures of a prototype of apparatus with all the embedded optical components are shown in Fig.2.8b. On the chip different portions are recognizable: a section with the polymeric diffraction grating (characterized by the reddish colouring of photoresist); a clean section, which is the imaging window; and finally a set of microlenses layered along the channel.

We tested the system using a polymer lens of 4.3mm focal length and set the distance between chip and camera to obtain a magnification M=15. The time sequence demonstrates the effectiveness of the pocket module with fully embedded optical components. DH flexible focusing capability can be exploited for three-dimensional tracking of a moving object inside a volume.

The 3D tracking of various worms moving inside the FoV is shown in Fig.9d-g and Movie 10. The estimation of the centre of mass of different objects on the image plane is possible also with non-holographic imaging techniques. Holographic imaging, however,

FIGURE 2.8: Pocket holographic module. The module is conceived starting from the parallel configuration of the holographic chip. Here, the presence of a microlens in correspondence of the microfluidic channel provides the required magnification (a). (b) A prototype implementation of the module, comprising of a CCD camera and the holographic chip with integrated microlenses.

permits to recover information on the third coordinate. This can be estimated by the propagation distance required to refocus the tracked object and automated by autofocusing algorithms.

Fig.2.9a shows three frames of the tracking of three different worms. In order to estimate the worms' centre of mass the same threshold is applied to all frames. The tracking on the image plane is performed assuming a maximum displacement of 100μm. The plot in Fig.2.9c, shows the three-dimensional trajectories of the worms in the observed volume. Similarly, Fig.2.9b and d show the 2D and 3D tracking of two worms moving at close distance.
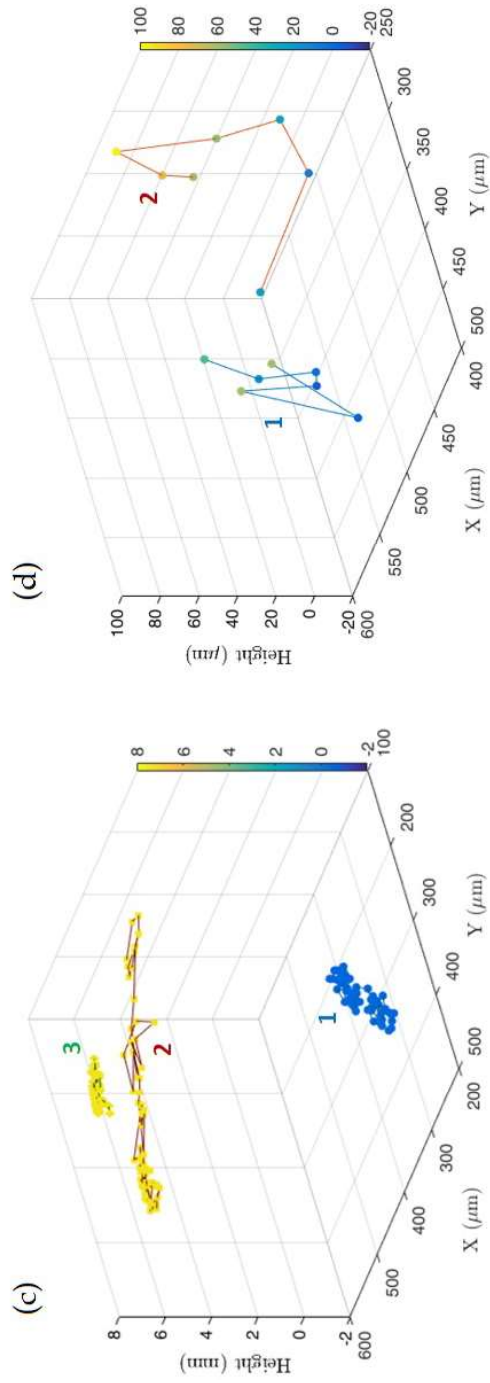
FIGURE 2.9: a-b) Tracking of different *C. elegans* worms swimming in the field-of-view at different heights. c-d) 3D tracking plots relative to the worms in (a) and (b), respectively.

Part II

DIGITAL HOLOGRAPHY OF TOTAL INTERNAL REFLECTION

3

TOTAL INTERNAL REFLECTION

WHEN light crosses the boundary between two dielectric media with different refractive indices, n_1 and n_2, it is partly reflected according to the Fresnel equations. If the refractive index $n_1 > n_2$, there is a critical angle, θ_c, where the reflectance becomes unity and light is totally reflected at the interface. In this case, the reflection coefficients become complex and there is no propagating light in the medium n_2, only an evanescent wave that exponentially decays along the propagating distance. Total internal reflection microscopy takes advantage of this phenomenon to illuminate a sample volume of only a few hundred nanometers at the interface with the substrate.

The thin layer of illumination is an *evanescent field* produced by an excitation light beam in a solid (e.g., a glass coverslip or tissue culture plastic) that is incident at a high angle upon the solid/liquid surface at which the sample (e.g., single molecules or cells) adheres. The incidence angle θ measured from the normal, must be greater than some *critical angle* for the beam to totally internally reflect rather than refract through the interface. TIR generates a very thin electromagnetic field in the liquid with the same frequency as the incident light, exponentially decaying in intensity with distance from the surface.
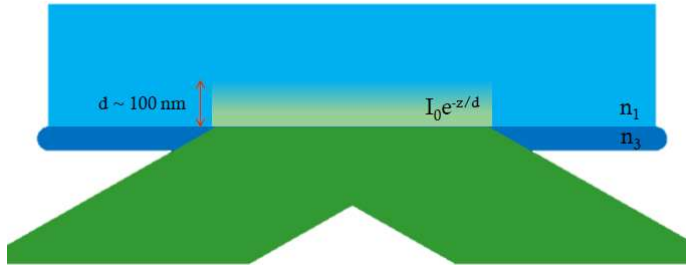
FIGURE 3.1: Depiction of the evanescent waves arising at the interface between two dielectric media in case of super-critical illumination.

3.1 CONCEPT AND THEORY

The simplest case of TIR is that of an *infinitely extended* plane wave incident upon a single interface (i.e., a beam width many times the wavelength of the light, which is a good approximation for unfocused or weakly focused light); see Fig.3.1. When a light beam propagating through a transparent medium 3 of high index of refraction (e.g., glass) encounters a planar interface with medium 1 of lower index of refraction (e.g., water), it undergoes total internal reflection for incidence angles θ measured from the normal to the interface) greater than the critical angle θ_c given by:

$$\theta_c = \sin^{-1}(n_1/n_3) \tag{3.1}$$

where n_1 and n_3 are the refractive indices of the liquid and the solid respectively.

Ratio n_1/n_3 must be less than unity for TIR to occur. (A refractive index n_2 will refer to an optional intermediate layer to be discussed below.) For *subcritical* incidence angles $\theta < \theta_c$, most of the light propagates through the interface into the lower index material with a refraction angle (also measured from the normal) given by Snell's Law. (Some of the incident light also internally reflects back into the solid). But for *supercritical* incidence angles $\theta > \theta_c$, all of the light reflects back into the solid.

Even in this case, some of the incident light energy penetrates through the interface and propagates parallel to the surface in the plane of incidence. The intensity I of the evanescent field at any position (measured as perpendicular distance z from the TIR interface) is the squared amplitude of the complex electric field vector E at that position:

$$I(z) = E(z) \cdot E^*(z). \tag{3.2}$$

For an infinitely wide beam, the intensity of the evanescent wave (measured in units of energy/area/sec) exponentially decays with z:

$$I(z) = I(0)e^{-z/d} , \tag{3.3}$$

where

$$d = \frac{\lambda_0}{4\pi}(n_3^2 \sin^2\theta - n_1^2)^{-1/2} = \frac{\lambda_0}{4\pi n_3}(\sin^2\theta - \sin^2\theta_c)^{-1/2} \,. \qquad (3.4)$$

The parameter λ_0 is the wavelength of the incident light in vacuum. Depth d is independent of the polarization of the incident light and decreases with increasing θ. Except for supercritical $\theta \to \theta_c$ (where $d \to \infty$), d is generally the order of λ_0 or smaller.

A physical picture of refraction at an interface shows TIR to be part of a continuum, rather than a sudden new phenomenon appearing at $\theta = \theta_c$. For small θ, the refracted light waves in the liquid are sinusoidal, with a certain characteristic period noted as one moves normally away from the surface. As θ approaches θ_c, that period becomes longer as the refracted rays propagate increasingly parallel to the surface. At exactly $\theta = \theta_c$, that period is infinite, since the wavefronts of the refracted light are themselves normal to the surface. This situation corresponds to $d = \infty$. As θ increases beyond θ_c, the period becomes mathematically imaginary. Physically, this corresponds to the exponential decay of (3.3).

In the real case of a finite incident beam, this can be expressed mathematically as an integral of infinite plane waves approaching at a range of incidence angles. In general, the intensity profile of the resulting evanescent field can be calculated from the mathematical form for the evanescent wave that arises from each infinite plane wave incidence angle, integrated over all the constituent incident plane wave angles. For a TIR Gaussian laser beam focused with a typically narrow angle of convergence, the experimentally observed evanescent illumination is approximately an elliptical Gaussian profile, and the polarization and penetration depth are approximately equal to those of a single infinite plane wave.

3.2 TOTAL INTERNAL REFLECTION MICROSCOPY

By using an objective with a sufficiently high NA, supercritical angle incident light can be cast upon the sample by illumination through the objective [91, 92]. Although an arc lamp can be used as the light source, the general features are best explained with reference to a laser source. The optical system has the following general features: The laser beam used for excitation is focused (by an external focusing lens) to a point at the back focal plane of the objective so that a collimated beam emerges from the objective, Fig.3.2. This insures that all the rays are incident upon the sample at the same angle θ with respect to the optical axis.

The point of focus in the back focal plane is adjusted to be off-axis. There is a one-to-one correspondence between the off-axis radial distance ρ and the angle θ. At a sufficiently high ρ, the critical angle for TIR can be exceeded. Further increases in ρ serve to reduce the characteristic evanescent field depth d in a smooth and reproducible man-
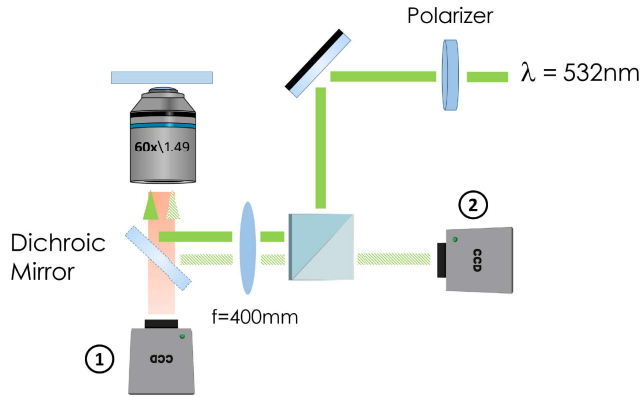
FIGURE 3.2: Schematic representation of TIR/TIRF setup. Camera 1 collects the fluorescence coming from the sample and that is separated from reflected light by the dichroic mirror. Reflected light, instead, is collected by camera 2.

ner. The beam can emerge into the immersion oil (refractive index n_{oil}) at a maximum possible angle θ_m measured from the optical axis) given by:

$$NA = n_{\text{oil}} \sin \theta_m \tag{3.5}$$

Since $n_3 \sin \theta_3$ is conserved (by Snell's Law) as the beam traverses through planar interfaces from one material to the next, the right side of (3.5) is equal to $n_3 \sin \theta_3$ (where subscript 3 refers to coverslip substrate upon which the cells grow). For total internal reflection to occur at the interface with an aqueous medium of refractive index n_1, θ_3 must be greater than the critical angle θ_c as calculated from

$$n_1 = n_3 \sin \theta_c \ . \tag{3.6}$$

From (3.5) and (3.6), it is evident that the NA must be greater than n_1, preferably by a substantial margin. This is no problem for an interface with water with n_1 = 1.33 and a NA = 1.4 objective. But for viewing the inside of a cell at n_1 = 1.38, a NA = 1.4 objective will produce TIR at just barely above the critical angle. The evanescent field in this case will be quite deep, and dense heterogeneities in the sample (such as cellular organelles) will convert some of the evanescent field into scattered propagating light.

Fortunately, objectives are now available with NA > 1.4. The highest aperture available are Olympus Olympus APO 100x/NA 1.65 and NA 1.7 APON100xHOTIRF; these work very well for objective-based TIRF on living cells. However, they require the use of expensive 1.78 refractive index coverslips made of special sapphire glass. These objective also require special n = 1.78 oil (Cargille) which is volatile and leaves a crystalline

residue. Zeiss, on the other hand, produced the alpha Plan-Apochromat 100x/1.57, which uses high-index (n=1.66) cover glasses and a special non-volatile immersion oil (n=1.66).

Several other objectives that are now available with NA ranging from 1.45 to 1.49, circumvent these problems. These objectives all use standard glass (n = 1.52) coverslips and standard immersion oil and yet still have an aperture adequate for TIRF on cells. The 1.49NA objectives are probably the method of choice for TIR except for cells which have particularly dense organelles. Dense organelles tend to scatter the evanescent field, and this effect is less prominent with the higher angles of incidence accessible through higher aperture objectives.

The angle of convergence/divergence of the laser beam cone at the back focal plane is proportional to the diameter of the illuminated region subsequently created at the sample plane. Large angles (and consequent large illumination regions) can be produced by use of a beam expander placed just upbeam from the focusing lens. The orientation of the central axis of the laser beam cone at the back focal plane determines whether the TIR-illuminated portion of the field of view is centered on the microscope objective's optical axis.

3.3 CONSIDERATIONS ON THE EXPERIMENTAL DESIGN

3.3.1 *Laser source*

A laser with a total visible output in the 100mW or greater range is more than adequate for most TIRF applications. Air cooled argon or diode lasers in the 10mW to 100mW are also usually adequate, but possibly marginal for dim samples or for samples where a weaker laser line (e.g., the 457nm line of argon) may be desired to excite a shorter wavelength fluorescent marker (such as cyan fluorescent protein, CFP).

Laser illumination can produce annoying interference fringes because optical imperfections in the beam path can shift the local phase of coherent light. For critical applications, several approaches can alleviate the problem.

One approach employs an optical fiber bundle in which individual fiber-to-fiber length differences exceed the laser light's coherence length. This produces an extended source at the output tip with point-to-point relative phases that are temporally randomized and defocused on the sample [93]. This elegant system, with no moving parts, produces a speckle pattern that changes so rapidly that it appears uniform down to the nanosecond time scale. Commercially available mode scramblers and rapid flexing of optical fibers may also reduce some fringing. Another set of methods uses a free laser beam rather than fibers. For example, a finely frosted glass surface or a plastic plate (such as tissue culture dish bottom), spinning laterally to the laser beam, temporally randomizes the phase and produces a fringe pattern that fluctuates and can be averaged over the duration of a camera exposure [94].
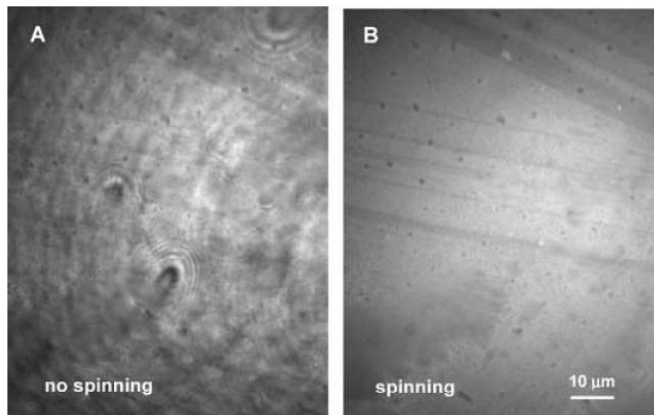
FIGURE 3.3: Effect of azimuthal spinning on TIRF images of diI adsorbed to a glass coverslip. a) Sample illuminated with a single azimuthal incidence angle; i.e., not spinning. Interference fringes are very evident. b) Same field of view with wedge spinning. The laser interference fringes are no longer visible. [95]

Interference fringes can be effectively suppressed by spinning the azimuthal angle of TIR incidence with electro-optical or mechano-optical devices such that the incident beam traces a circle where it focuses at the objective's BFP. Since only one azimuthal direction illuminates the sample at any instant but the spinning period is much shorter than the camera's exposure time or retinal image retention time, the interference fringes are superimposed in their intensities (rather than in their electric fields), giving the illusion of a much more uniform illumination field [95]. An example of the fringe suppression effect is shown in Fig.3.3. An alternative non-optical approach to suppressing fringes computes a normalization of sample digital images against a control digital image of a uniform concentration of fluorophores. This works well only if the fringes were not induced by the sample itself.

3.3.2 *Actual evanescent field depth*

The evanescent field characteristic depth in an actual sample may deviate from that predicted by (3.4), even if the incidence angle θ is well measured, for several reasons. Depth d depends on the refractive index of the liquid sample above the TIR surface, and this is not well known for samples such as cell cytoplasm. So far, no good way of accurately measuring the local evanescent field depth and profile in an actual heterogeneous sample has been proposed.

Measurements of evanescent depth in a homogeneous artificial sample with a refractive index that approximated the average in a heterogeneous sample can be done. In such

a sample, the characteristic time for diffusion of fluorescent beads through the evanescent field (possibly by TIR/FRAP or TIR/FCS) can be measured and (given a known diffusion coefficient) converted to a corresponding characteristic distance. However, this method gives only a single number for effective depth but does not provide unambiguous information about the possibly non-exponential intensity profile as a function of z.

In samples with heterogeneous refractive index, regions with higher index may not support TIR, whereas lower index regions do. Clearly, it is best to illuminate with as high an incidence angle as possible to be sure that all regions support TIR. Even if the incidence angle is sufficiently high to support TIR everywhere, irregularities and heterogeneities in the sample give rise to scattering of the evanescent field. This scattered light can excite fluorescence as it penetrates much more deeply into the liquid than does the evanescent light.

3.3.3 *The objective*

The TIR optics itself, particularly the high aperture objectives, can produce scattered light. Actual intensity profiles arising from objective-based TIR can be obtained observing a large spherical bead (e.g. $8\mu m$ diameter) with a refractive index matched to the surrounding liquid to avoid disruption and scattering. The bead can be fluorescence-labeled on its surface. At the image of the point of contact between the bead and the TIR substrate, the fluorescence is the brightest. It becomes dimmer with increasing distance in the TIR plane from the contact point.

Simple geometry then allows calculation of the fluorescence vs. z. In an actual test of this method in 1.45 NA and 1.65 NA objective-based TIRF [96], the evanescent field was found to account for about 90% of the intensity at $z = 0$, and the exponential decay depth agreed well with expectations based on angle and refractive index. However, a much slower decaying component, presumably from scattering within the objective, was also evident, and this component became dominant in the distant $z > 2d$ zone.

Modern objective lenses are invariably designed for infinite conjugate ratio, i.e. the object of observation is placed in the front focal plane and its image is formed at infinity. In order to obtain a real intermediate image a separate lens, called the tube lens, is used. The focal length of this lens F (which ranges from 165mm for Zeiss and 180mm for Olympus to 200mm for Leica and Nikon) together with the magnification of the objective M gives the focal length of the objective $f = F/M$.

One of the basic postulates of aberration-free lens design is that it has to obey the Abbe's sine condition. For a microscope objective treated as a thick lens this can be interpreted as the fact that its front principal surface is actually a sphere of radius f centered at the front focus. Any ray leaving the focus at an angle α to the optical axis is intercepted by this surface at the height $d = f \sin \alpha$ and emerges from the back focal plane

parallel to the axis at the same height. For immersion lenses this has to be multiplied by the refractive index of the immersion fluid n.

In most high NA objective lenses the back focal plane, also called the pupil plane, is located inside the lens and is not therefore physically accessible. Fortunately lens designers tend to put an aperture stop as close to this plane as possible, which greatly simplifies the task of identifying the pupil plane when reimaging it using an auxiliary lens. Any extra elements, such as phase rings in phase contrast lenses or variable aperture iris diaphragms, will also be located in the back focal plane.

The physical aperture of an objective lens D is related to its numerical aperture $n \sin \alpha$ via

$$D = \frac{2Fn \sin \alpha}{M} \qquad (3.7)$$

ultimately it is limited by the size of the objective thread. This is one of the reasons why some lens manufacturers have now abandoned the former golden standard of RMS thread and moved to larger thread sizes.

Testing objective lenses with highest NAs (1.4 for oil, 1.2 for water immersion) one peculiar aberration pattern is frequently encountered [97, 98]. The lens is well corrected over up to 90-95% of the aperture radius, but after that we see a runaway phase variation right to the edge. Speaking in Zernike terms residual spherical aberration components of very high order are observed. Because of this high-order it appears unlikely that the aberrations are caused by improper immersion fluid or some other trivial reasons. These would manifest themselves via low-order spherical as well. More realistically, this is a design flaw of the lens. It is quite possible that in many cases this is a very expensive empty aperture, which, although physically present, does not contribute to the resolving power of the lens.

4

HOLOGRAPHIC TOTAL INTERNAL
REFLECTION MICROSCOPY

H ERE is presented a simple, high-resolution, non-fluorescent imaging technique called holographic total internal reflection (HoloTIR) microscopy and demonstrates its potential application to biomedical imaging. In addition, a novel instrument is introduced that combines the simplicity of HoloTIR microscopy with the specificity afforded by total internal reflection fluorescence (TIRF) microscopy and allows simultaneous imaging with the two modalities. The key design issues necessary to apply these imaging modes in a single instrument are investigated and discussed. The application of TIR alone yielded high-resolution images of cell adherence to a poly-L-lysine modified substrate. Finally, images of fluorescently labelled cells were obtained in TIRF mode, simultaneously to images obtained of the same cell in HoloTIR mode. The estimation of focal adhesion area evaluated using TIRF data is compared with HoloTIR to demonstrate that the level of cell structure information obtainable with our holographic total internal reflection microscope is comparable with the TIRF technique and improved with respect to other label-free techniques.

4.1 TOTAL INTERNAL REFLECTION OF DIGITAL HOLOGRAPHY

Total internal reflection of light can be also be exploited for holographic measurements of interfaces. Digital Holography microscopy has the advantage of measuring both amplitude and phase information from the observed sample32–34. The only experimental requirement is the formation of an interference pattern at the image plane with a reference beam.

4.1.1 *General Considerations*

The reflection phase, φ, is only zero or π for the usual Fresnel reflection, while beyond the critical angle the reflection phase decreases continuously and monotonically from 0 to $-\pi$ for both cases of polarization. For a given angle of incidence, the phase of TIR-reflected light will vary with n_2.

When imaging a biological sample, such as a cell, the basal membrane acts as a third dielectric layer of refractive index n_3. If the distance between the membrane and the substrate is smaller than the thickness of the evanescent field, it disrupts the evanescent wave, changing locally the complex refractive index. Simulating the three-layer case with the Transfer matrix method, we can obtain the response function of the system [99, 100].

Consider reflection of light, of vacuum wavelength λ_0, across a boundary between two dielectric media with indices n_1 and n_2 . The reflection coefficients are given by the familiar Fresnel equations:

$$r_\perp = \frac{n_1 \cos\theta_1 - n_2 \cos\theta_2}{n_1 \cos\theta_1 + n_2 \cos\theta_2} \ ; \quad r_{//} = \frac{n_2 \cos\theta_1 - n_1 \cos\theta_2}{n_2 \cos\theta_1 + n_1 \cos\theta_2} \tag{4.1}$$

for the s-polarization ($r_\perp$) and the p-polarization ($r_{//}$), respectively.

For internal reflection, $n_1 > n_2$, if the angle of incidence θ_1 is larger than the critical angle θ_c, then the reflectance $R = |r|^2$ becomes unity in total internal reflection (TIR) and $\cos\theta$ is imaginary.

Defining

$$h_2 = n_2 \cos\theta_2 = i\sqrt{n_1^2 \sin^2\theta_1 - n_2^2} = i\eta_2 \ , \tag{4.2}$$

the reflection coefficients become complex:

$$r_\perp = \exp\left(-2i\phi_\perp\right); \quad \phi_\perp = \tan^{-1} \frac{\sqrt{n_1^2 \sin^2\theta_1 - n_2^2}}{n_1 \cos\theta_1} \tag{4.3}$$

$$r_{//} = \exp\left(-2i\phi_{//}\right); \quad \phi_{//} = \tan^{-1} \frac{n_1 \sqrt{n_1^2 \sin^2\theta_1 - n_2^2}}{n_2^2 \cos\theta_1} \tag{4.4}$$

There is no propagating wave in transmission, but a thin layer of evanescent wave exists that decays exponentially, $E_t \propto \exp\left(-k_0 \eta_2 z\right)$, where $k_0 = 2\pi\lambda$ and z is the distance from the interface.

As shown in the plot in Fig.4.1a a different behavior between reflectivity and phase response can be observed. Notably, the region of higher sensitivity for reflectivity is around 150nm, while phase sensitivity is higher in proximity of the surface, between 0 and 95nm, see Fig.4.2.

When studying cell adhesion, discriminating between focal contacts (10-15nm from substrate) and areas of close contacts (30nm from substrate) can be of key interest. This
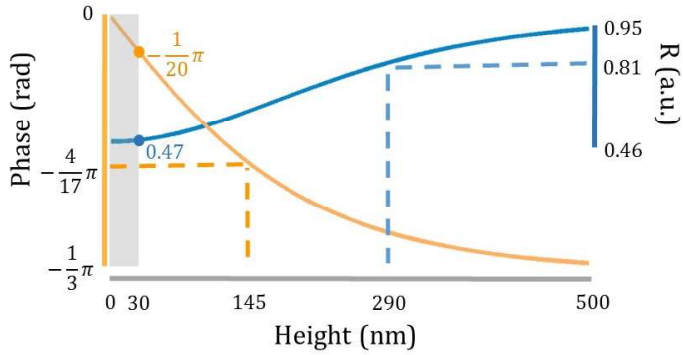
FIGURE 4.1: Three layer model for the theoretical response of HoloTIR system in aqueous medium in presence of adhering cells.
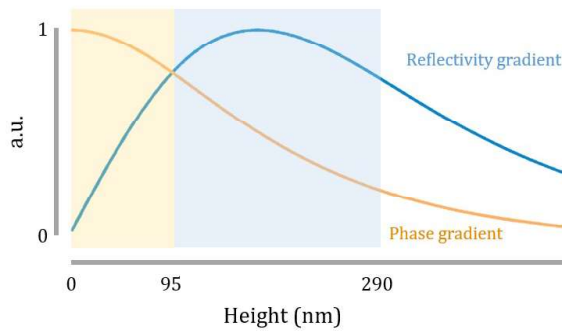
FIGURE 4.2: Comparison between the theoretical sensitivity of reflectivity and phase response of total internal reflection signal. A three-layer model is considered: glass, water, and cell. To show the signal sensitivity, normalized reflectivity and phase gradients are compared. Reflectivity has is maximum of sensitivity in the 95-290nm range (blue highlighted area), while rapidly losing accuracy beneath these distances. On the other hand, phase is most sensitive in correspondence of direct cell/glass contacts.
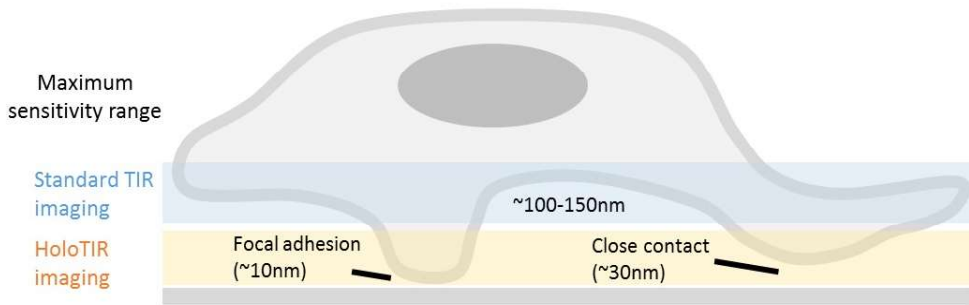
FIGURE 4.3: Cartoon illustrating the advantage of TIR phase microscopy for bio-imaging in comparison with standard TIR microscopy.

designates quantitative phase microscopy of total internal reflection as a new tool for the label-free investigation of cell adhesion, Fig.4.3.

4.1.2 *Objective-based HoloTIR Microscope*

In a classic TIR microscope, the illuminating light is focused at the back focal plane of a high numerical aperture objective by a lens of 200-400mm focal length. This lens is usually moved in order to focus light toward the border of the objective back focal plane until the total internal reflection condition at the sample interface is achieved.

The main differences between classic and holographic TIR microscopy is the presence of a beam-splitter placed before the focusing lens in order to create a reference beam. This reference beam is recombined through a second beam-splitter with the light totally reflected by the sample, forming a Mach-Zehnder interferometer. The presence of a sample modifies the phase front of the reflected light producing an interference pattern on the camera plane. A sketch of the experimental apparatus is depicted in Fig.4.4.

The numerical reconstruction of the interference pattern yields two images of the specimen: the amplitude and the phase images. However, the experimental setup introduces an offset that must be removed in order to obtain quantitative phase maps of the sample. One of the most diffused methods in digital holography is the double exposure technique, where the instrumental contributions are estimated by a reference hologram of a flat surface where no object is present [76]. A depiction of the reconstruction process is shown in Fig.4.5.

Two key aspects of the holographic setup are the laser source and the high numerical aperture objective. A laser source with a sufficiently high temporal coherence is important in order to have a fringe pattern with reasonable contrast. A high coherence permits, also, a greater versatility in the setup design, giving more freedom in the construction of
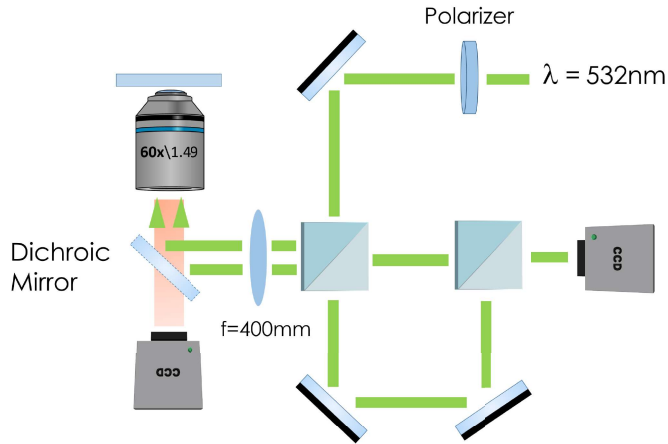
FIGURE 4.4: sketch of the experimental setup of HoloTIR microscopy.
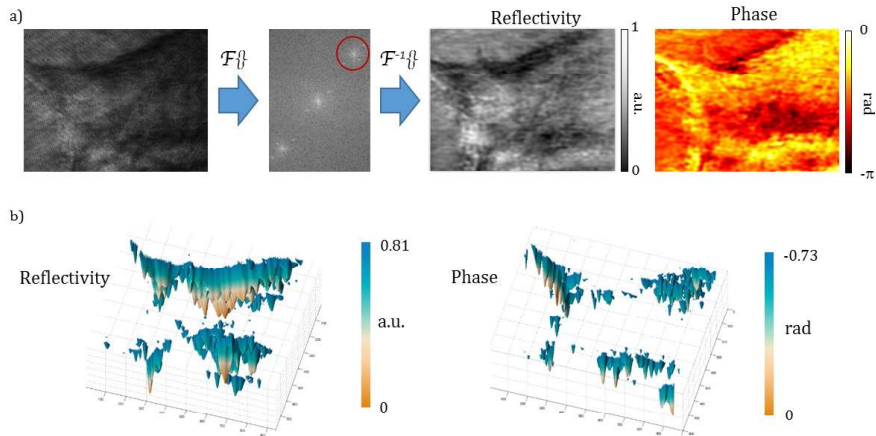
FIGURE 4.5: Numerical reconstruction of Holographic TIR images. (a) After the recording, the hologram is numerically processed to obtain amplitude and phase information of the wavefront coming from the sample. From the Fourier transform of the acquired image, the order +1 is isolated and anti-transformed. This operation yields the complex wavefront from which can be extracted reflectivity and phase images. (b-c) 3D depictions of reflectivity and phase information. In both images the signal detection limit was set as a threshold.
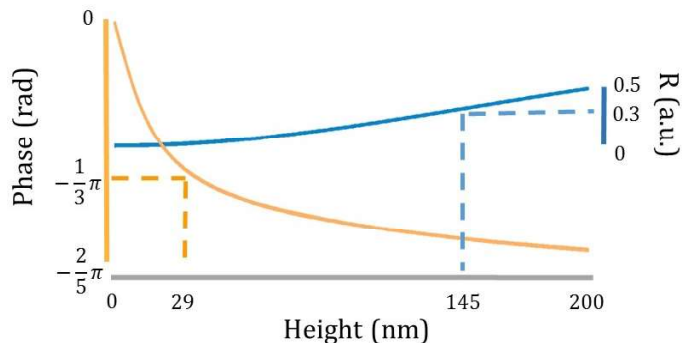
FIGURE 4.6: Theoretical response of HoloTIR system in aqueous medium in presence of polystyrene beads, n=1.6.

the interferometer. The high numerical objective, on the other hand, is crucial to obtain a uniform illumination and minimize optical aberrations. In order to achieve TIR illumination, objectives with numerical aperture greater than 1.4 are required. Such objectives, however, often present a decay of optical quality in correspondence of the edge of the back focal plane. This gives rise to imperfections in the illumination, the so-called objective fingerprint, which can partially disrupt the evanescent field. It is fundamental, then, to avoid such imperfections because they lower the effective numerical aperture of the objective [101]. To this end, for the imaging of biological samples is strongly recommended the use of good quality TIRF objectives with very high numerical aperture (NA>1.49).

4.1.3 *Testing the intensity and phase profile*

Firstly, we tested the HoloTIR setup with polystyrene fluorescent beads of 1μm diameter. The fluorescent polystyrene beads (Polysciences PolyFluor microspheres, 1μm diameter) were sonicated and platted on a PLL coated glass coverslip and let dry. After extensive washes, the coverslip with the adherent beads was imaged in both TIRF and HoloTIR mode.

The theoretical TIR response for a polystyrene bead (n=1.6) in water is shown in Fig.4.6. The sample was illuminated at an angle of 64 degrees and images were taken in both TIRF and HoloTIR configuration.

The 3D maps of a single bead obtained by fluorescence, reflectivity, and phase are shown in Fig.4.7. The maps were produced filtering all the signal within three standard deviations from the background noise.
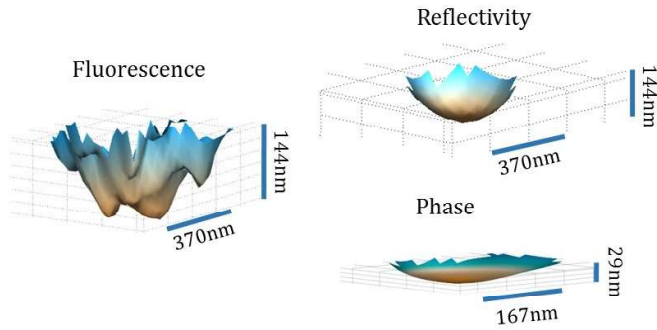
FIGURE 4.7: 3D mapping of the same fluorescent polystyrene bead with TIRF and HoloTIR microscopy.

The experimental penetration depth can be calculated knowing the bead's radius (r=0.5μm) and the camera pixel size (p=0,037μm):

$$d = r - \sqrt{r^2 - (pN/2)^2}$$

, where N is the diameter of the spherical cap in number of pixels. Both fluorescence and reflectivity images have a penetration depth of 144nm (N=20), which is in agreement with the theoretical value at 64 degrees. In the case of the phase map the sampling of the spherical surface is only a few pixels (N=9), due to the fast decay of phase response. Nevertheless, the measured penetration depth is 29nm, which, once again, is in accordance to the theoretical value in Fig.4.6.

4.2   LABEL FREE IMAGING OF CELL/SUBSTRATE CONTACTS

In the case of cells in water, it is worth noting from fig.1a deeper effective penetration depths for both reflectivity and phase measurements: 200 and 145nm, respectively. Such effective penetration depth were evaluated calculating the value where the system response of the 1/e= 37We expect different outcomes from reflectivity and phase images due to the different sensitivities, which vary with sample height in different but symmetrical ways, as shown in Fig.4.2. We can see, in fact, that reflectivity has greater sensitivity toward the detection limit while an almost flat response below the 90nm. On the other hand, phase response shows a higher sensitivity around 10nm, which rapidly decays after 50nm.

The study of cell/substratum contacts was performed using NIH-3T3 mouse embryonic fibroblast cells.
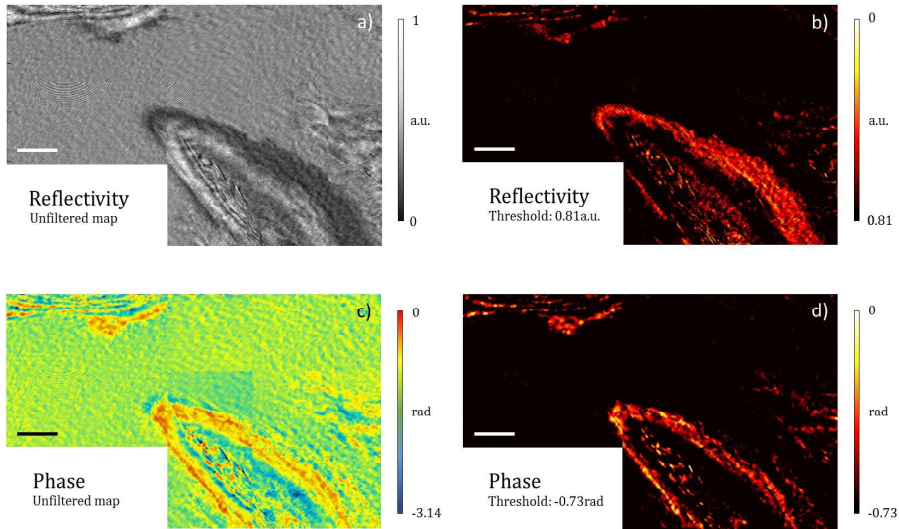
FIGURE 4.8: Numerical reconstruction of Reflectivity (a-b) and Phase (c- d) of an adhering NIH-3T3 fibroblast on glass substrate. Images (b) and (d) are filtered according to the theoretical penetration depth. Scale 10μm.

Amplitude and phase holographic reconstructions of a NIH-3T3 cell adhering on fibronectin are shown in Fig.4.8a and c. The same images, with a threshold corresponding to the penetration depth of reflectivity and phase response, are depicted in Fig.4.8b and d respectively. The images look slightly different because of the different penetration depths and sensitivities. While reflectivity shows a more complete view of the cell basal membrane, phase image is limited to closer distances and, hence, more appealing for contact areas identification and quantification [102].

4.2.1 Imaging of Cell adhesion on different substrates

In order to assess the effectiveness of HoloTIR microscopy, we studied cell adhesion of fibroblasts on different substrates: glass, fibronectin, and Poly-L-lysine (PLL). These are well-studied substrates, where the affinity of cell contacts is known [103–107].

WillCo-dish® Glass Bottom dishes (35 mm diameter) were used for cell attachment study. D-PLL at 0.1 mg/mL in phosphate buffered saline (PBS, pH 7.4) was add over the surface of glass dish and incubated for 1h at 37 °C. Then, the solution was removed and the dish washed three times with PBS and let dry before adding cell suspension. For FN

coating, a 100 μg/mL solution in PBS was add to the glass dish, incubated for 45 minutes at room temperature. Then, the coating solution was aspirated and the dish rinsed 3 times with PBS. The FN coating was not allowed to dry and cell suspension was immediately added. For the glass, used as control, the dish was used without any treatment.

The cell adhesion on surfaces was evaluated in vitro using mouse embryonic fibroblast (NIH-3T3). NIH-3T3 cells were grown in Petri dishes in Dulbecco's modified Eagle's medium (DMEM) containing 4.5 g/L D-glucose and supplemented with 10

Immunostaining with antitalin antibody was carried out in order to visualize further the actin-based cytoskeleton in the cell-cell and cell-substrate junctions. NIH-3T3 cells were incubated first in a primary antitalin antibody (Biorbyt Limited, UK) diluted in blocking solution for 1 h, and then in a secondary donkey antirabbit TRITC conjugated (Thermo Scientific, USA) at 1:200 dilution in blocking buffer solution for 45 min. The samples were washed three times in PBS between each antibody treatment.

We analyzed three samples for each substrate. Cell concentration was kept low in order to avoid cell overlapping and simplify cell counting. Multiple images were collected by XY scanning and successively reflectivity and phase reconstructions were stitched together, see Fig.4.9a-f. To study the presence of focal adhesion we counted the number of pixels per cell where the phase signal is in the range correspondent to distances lesser than 15nm ($\Delta\varphi$>-0.05rad). We did the same with reflectivity images (R<0.47). The histograms in Fig.4.9g report the estimated focal contact area per cell for each substrates. Percentage variations of the focal contact area respect to the glass substrate are also reported. From phase data, it is clear that cells adhering on fibronectin show a greater occurrence of focal contacts. On the other hand, cells on PLL show less focal contacts than those adhering on glass. These results are in accordance with those obtained by TIRF microscopy, where the presence of Talin clusters is measured, see Appendix A. This trend is not depicted by reflectivity data. As discussed in previous section, reflectivity response in the range of 0-50nm has a lower sensitivity compared to phase signal and signal fluctuations are not great enough to mark a clear distinction between close and focal contacts.

4.2.2 *Time-lapse imaging*

A major disadvantage of fluorescence microscopy is the difficulty of long-time recording. After prolonged exposure to excitation illumination, in fact, fluorescence markers tend to fluctuate in intensity and eventually photobleach. Another issue which affects time-lapse imaging is the photoxicity induced by elevated intensities necessary to excite fluorophores. Such issues are not present in HoloTIR microscopy: not using labels, in fact, there is no photobleaching and light levels can be set much lower than fluorescence microscopy, thus reducing phototoxicity.

Dynamics of focal contacts formation were observed by time-lapse imaging of a NIH fibroblast adhering on glass. The cell was added to the dish, let precipitate for 5 minutes,
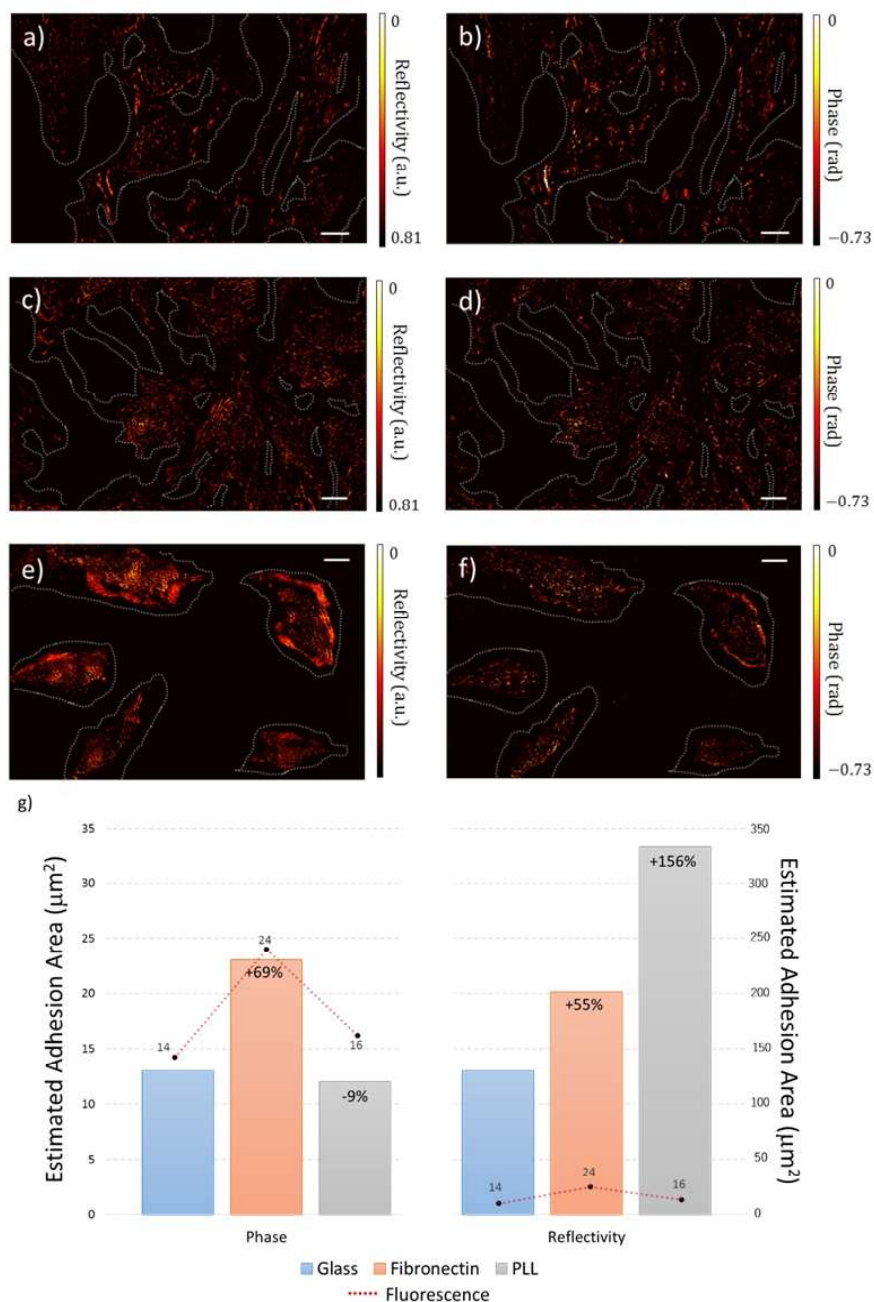
FIGURE 4.9: a-b) Reflectivity and phase-contrast images of adhering cells on non-functionalized glass. c-d) Reflectivity and phase-contrast images of adhering cells on fibronectin. e-f) Reflectivity and phase-contrast images of adhering cells on PLL. Scale 30μm. g) Estimated area of focal adhesion per cell obtained by phase and reflectivity-contrast images: both histograms are compared with fluorescence data of talin aggregation obtained using TIRF microscopy (dashed line).
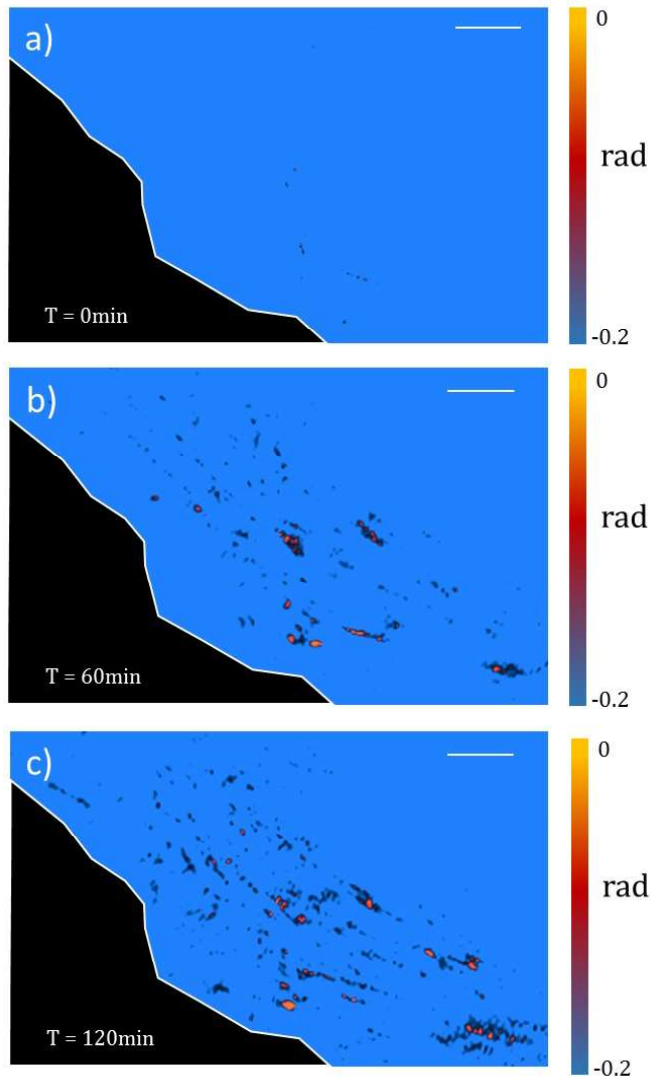
FIGURE 4.10: a-c) The formation of focal contacts on glass substrate is shown at three different adhesion stages: 0, 60, and 120min. In order to highlight focal contacts, only values above -0.2rad are shown. Scale 3μm.

and then imaged for 2 hours. Fig.4.10 shows focal contacts at three different moments of the adhesion process: 0, 1 hour and 2 hours. In order to maintain cell activity, both petri dish and microscope objective were heated at 37°C and 20μM of HEPES were added to stabilize the pH of the medium.

Part III

HOLOGRAPHIC SURFACE PLASMON RESONANCE

5

THE PRINCIPLES OF SURFACE PLASMON RESONANCE

S URFACE Plasmon Polaritons (SPPs, also simply SPs) are electromagnetic surface wave bound in the region between two dielectrics and a metallic or conducting layer. When external light energy resonantly induces the free electrons of the metal to oscillate at the interface, the radiant energy is absorbed and the metal displays a reflectivity minimum. This phenomenon, called Surface Plasmon Resonance (SPR), occurs at a certain incident angle depending on the index of refraction of the dielectric medium in contact with the metal surface. This means that changes in the refractive index of the dielectric affect the excitation of SPs along the metal. This is usually detected as a variation of reflectivity of the sample but also other parameters can be measured. The most common alternative is the measurement of the phase of the reflection coefficient. However, polarization and color are also used. The sensitivity of this technique is such that it is commonly used to develop sensors, e.g. for the monitoring of biomolecular interactions, as well as to build systems for two-dimensional imaging. The latter is generally referred as Surface Plasmon Resonance imaging (SPRi).
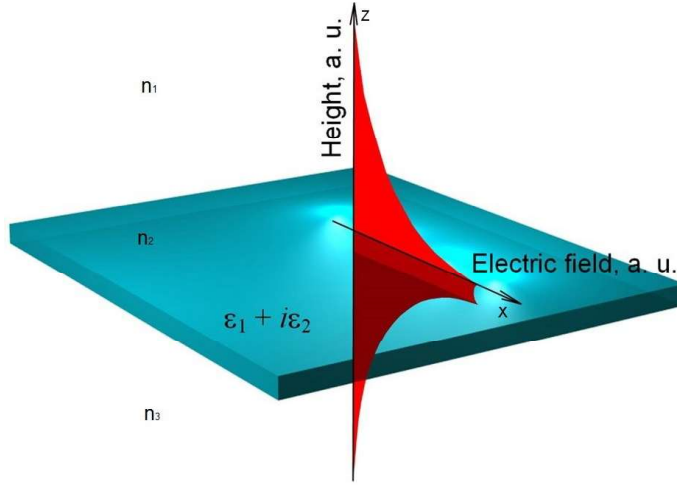
FIGURE 5.1: Excitation of surface plasmons in a three layer system, consisting of a thin metal slab sandwiched between two dielectrics

5.1 OVERVIEW OF SURFACE PLASMONIC RESONANCE

The simplest system on which SPs exist is between the interface of a relatively thin conducting layer located between two dielectric layers. This situation is depicted schematically in Fig.5.1. A condition for the existence of SPs is that the real part of the dielectric permittivity, ε, of the conducting layer is negative.

Physically SPs may be thought of as collective oscillations of charge carriers in the conducting layer, with the result that energy is transferred parallel to the interface [108]. In practice, noble metals such as gold and silver are excellent metals to support the propagation of SPs and indeed are used by the great majority of studies in the literature. Aluminum also supports SP propagation although the attenuation with this metal is very severe, since the positive imaginary part of the dielectric permittivity is relatively large.

5.1.1 *Dispersion relation*

For the sake of simplicity, let us consider a single TM-polarized SP wave bound at the interface between two (isotropic) semi-infinite media, as shown in Fig.5.1. The electric and magnetic fields associated with the SP wave in this case are given by:

$$\begin{aligned}
\mathbf{E}_j &= (E_{xj}, 0, E_{zj})e^{i(k_x x - \omega t) \pm (i k_z z)} \\
\mathbf{H}_j &= (0, H_{yj}, 0)e^{i(k_x x - \omega t) \pm (i k_z z)} \quad (j = 1, 2)
\end{aligned}$$

(5.1)

where j denotes the material (1 for the metal and 2 for the dielectric), the positive part of the z-axis is where lies in the dielectric. The first exponential term accounts for propagation along the interface (in positive x-direction), while the imaginary k_z describes the exponential decay in the z-direction. Since the SP wave is TM-polarized, there is no electric field component in the y-direction.

For the condition of continuity at the boundary, we have that:

$$E_{x1} = E_{x2}$$
$$H_{y1} = H_{y2} \tag{5.2}$$
$$\varepsilon_1 E_{z1} = \varepsilon_2 E_{z2}$$

This implies that $k_{x1} = k_{x2} = k_x$. The Maxwell relations applied on the waves in (5.1) lead to the following set of partial differential equations:

$$\frac{\partial E_{xj}}{\partial z} - ik_x E_{zj} - i\omega\mu_0 H_{yj} = 0$$
$$\mu_0 \frac{\partial H_{yj}}{\partial z} - \frac{i\omega\varepsilon_j}{c^2} E_{xj} = 0$$
$$\mu_0 \frac{\partial H_{yj}}{\partial x} - \frac{i\omega\varepsilon_j}{c^2} E_{zj} = 0 \tag{5.3}$$
$$\frac{\partial E_{zj}}{\partial z} - ik_x E_{xj} = 0$$

Equation 5.3, together with the boundary conditions (5.2), yield the following dispersion relation:

$$\frac{k_{z1}}{\varepsilon_1} + \frac{k_{z2}}{\varepsilon_2} = 0$$
$$k_{zj} = \sqrt{\frac{\omega^2\varepsilon_j}{c^2} - k_x^2} \tag{5.4}$$

that lead to the dispersion relation for SPs at a semi-infinite metal-dielectric interface:

$$k_x = \frac{\omega}{c}\sqrt{\frac{\varepsilon_1\varepsilon_2}{\varepsilon_1 + \varepsilon_2}} \, . \tag{5.5}$$

5.1.2 *Surface wave excitation*

A key property of SPs is that the k-vector is greater than the free space k-vector. This means that SPs cannot be excited from free space unless evanescent waves or a structured surface such as a grating is used.
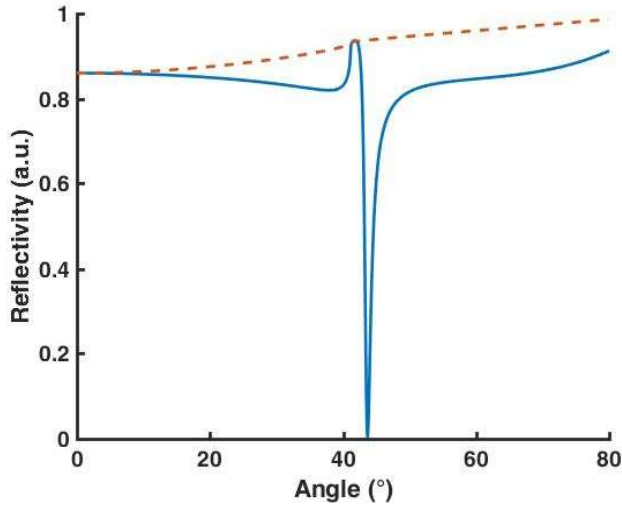
FIGURE 5.2: Modulus of the reflection coefficient for a three layer system consisting of glass, gold and air, described in Section 5.1.2. The wavelength considered is 633nm. Both p-polarization, solid line, and s-polarization, dashed line, are shown.

In order to overcome this problem light from a region of high refractive index can be used to illuminate the sample. The variation of reflection coefficient with incident angle from a thin metal film gives considerable insight into the behaviour of SPs. Fig.5.2 shows the modulus of the amplitude reflection coefficient for 633nm incident wavelength, for the system shown in Fig.5.1, when $n_1 = 1.52$, $n_2 = \varepsilon 1/2 = (-12.33 + 1.21i)^{1/2} = 0.17 + 3.52i$, and $n_3 = 1$. These values correspond to the refractive index of glass or coupling oil, gold and air. The thickness of the gold layer in the simulations is 43.5nm.

We see that for s-incident polarization the modulus of the reflectivity is described by a flat curve. On the other hand, for p-incident polarization there is a sharp dip at an incident angle, θ_p close to 43.6 degrees. This corresponds to the excitation of SPs that can only happen with p-incident polarization.

The reduction of reflection coefficient relates to the fact that when SPs are excited some of the energy is dissipated in ohmic losses in the film. Excitation of SPs at an angle of approximately 44 degrees implies that the k-vector of the SPs is greater than the free space k-vector.

From the position of the dip, it is possible to see that the k-vector of the SP is $n_1 \sin \theta_p \approx$ 1.05 times greater than the free space propagation constant.

The reflection coefficient for p-polarised light shown in Fig.5.2 is indicative of the excitation of SPs when losses are present. If, however, the refractive index of the metal film
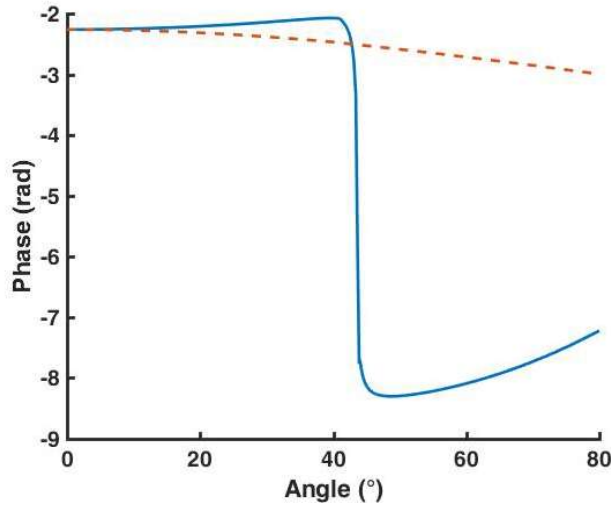
FIGURE 5.3: Phase of reflection coefficient corresponding to case described in Section 5.1.2. Note that the phase of the reflection coefficient for the p-polarization (solid line) is shifted by 2π radians respect to the s-polarization (dashed line).

is entirely imaginary the dip disappears, although SPs are still excited. The dip in the reflection coefficient is, thus, not an essential manifestation of the SP excitation.

The phase of the reflection coefficient, in fact, gives real evidence of the excitation of surface waves. We will show, actually, that it is the phase of the reflection coefficient the most interesting property of SP excitation for imaging applications.

Figure 5.3 shows the phase of the reflection coefficient for both s-polarised and p-polarised light. The phase behaviour of the s-polarised light, like the amplitude, shows little structure, but the phase variation of the p-polarised light shows a strong feature close to the angle θ_p. Around this angle the phase change is close to 2π radians. This is a more fundamental feature of SP excitation than the dip in the amplitude of the reflection coefficient.

5.2 OPTICAL PLASMON EXCITATION: KRETSCHMANN CONFIGURATION

The most popular way to excite and detect SPs is to use the Kretschmann configuration, see Fig.5.4. The metal film, usually gold or silver, is deposited on the hypotenuse of the prism and the light is incident along one of the other sides so it hits the metal film through the glass at an angle, θ, close to θ_p. The passage of the light through the glass increases the k-vector of the incident wave so that its component parallel to the surface matches that
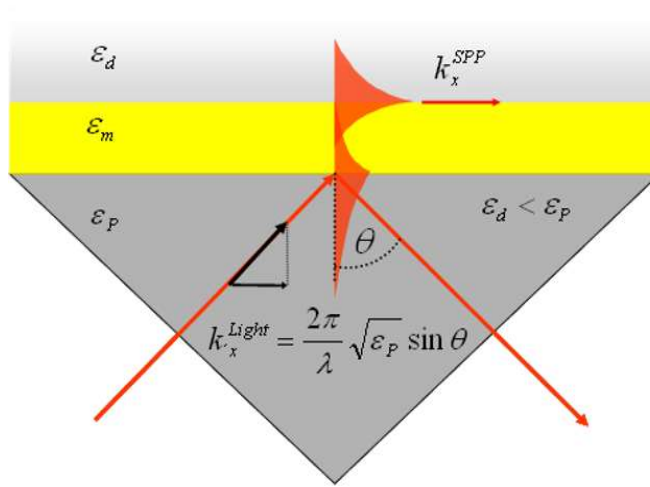
FIGURE 5.4: Schematic diagram showing wide-field SP optical exctitation on Kretschmann configuration.

of the SP. The changes in the reflected light enable the properties of materials absorbed on the layer to be sensitively monitored.

SPs find wide use as chemical and biosensors for application such as monitoring antibody-antigen reactions, cell attachment and toxicology (and indeed any areas where sensitivity to minute changes in the properties of an interface is required).

Standard Kretschmann based SP techniques are thus extremely powerful, they do, however, lack the spatial resolution required to image highly localised regions on, for instance, a cellular level. For this reason there has been substantial work to develop SP microscopy techniques that combine high lateral resolution with good surface sensitivity.

We saw in Section 5.1 that for two semi-infinite dielectric/metal layers the momentum of incident plane wave light can never match the surface plasmon momentum.

In order to have resonance, the x-component of the incident light wavevector needs to match the SP wavevector. This resonance condition can be expressed:

$$k_{SP} = \frac{\omega}{c} \sqrt{(\varepsilon_0)} \sin \theta \qquad (5.6)$$

in which ε_0 is the dispersion of the prism and θ the internal angle of incidence.

In order to satisfy the condition (5.6) it is required that

$$n_{\text{prism}} \sin \theta > n_a \sin \theta_a \, , \qquad (5.7)$$

where the subscript a denotes the ambient. The resonance condition can therefore only be fulfilled at values of θ greater than the critical angle of incidence, θ_c.

In 1968, Otto presented the ATR configuration for SP excitation through an air gap between a glass prism and a semi-infinite metal film [109]. In the same year, Kretschmann and Raether devised a setup in which the metal film was evaporated directly on the prism [110]. These two configurations are referred to as prism couplers and utilize the evanescent field of light reflected at the prism boundary to excite surface plasmons.

Among the prism couplers, the Kretschmann configuration is prevalent much thanks to its simplicity. The Otto configuration requires precise manufacture and positioning techniques in order to achieve perfectly parallel prism and metal surfaces with an exact and sub-micron wide gap in between. Direct evaporation of the metal film on a prism surface is on the contrary quite straightforward, but seldom used. Instead, an index matching oil or gel is used to optically couple gold coated glass slides to the prism. This allows for exchange of the functional gold film and reuse of the prism.

In addition, because the light is incident from below, avflow cell can be docked to the sensor surface, making the Kretschmann configuration well suited for application within biosensing wherein samples are sequentially injected over the surface.

The difficulty with Kretschmann based prism configurations arises from two principal factors:

- The prism means the system is not readily compatible with a conventional microscope configuration, for instance, imaging through the prism is difficult, especially when the plasmon is excited close to grazing incidence.

- The lateral resolution is poor compared to that achievable with optical microscopy, so that the range of applications will be restricted. In particular, applications in extremely important fields, such as cell biology, will be severely limited. For these reasons it is necessary to develop techniques capable of overcoming these limitations.

- Resolution in prism-based imaging is mainly governed by geometrical aberrations, which distort SPR images [111].

- Finally, the prism also limits the compatibility with conventional microscopes and causes the images to move when the incident angle is changed, thus limiting the use of angular scanning techniques.

5.3 THROUGH-THE-OBJECTIVE SP EXCITATION

Consider an aplanatic objective with a source of illumination in the back focal plane. Each point incident on this plane maps to an incident plane wave propagating in a direction whose k-vector parallel to the plane of incidence is proportional to the radial position of the source in the back focal plane. If the polarization of the beam incident on the back

focal plane is linear, the polarization state of the incident radiation varies from pure p-polarised to pure s-polarised. In general, the polarization is a combination of the two states, which can be determined by resolving with respect to the azimuthal angle, ϕ.

For an oil immersion lens with a numerical aperture greater than about 1.1 a fully illuminated objective lens will generate plane waves whose incident angle and polarization state can excite SPs on the sample provided the final dielectric has an index close to unity.

Since the k-vector of SPs with air backing is only a few percent greater than that in free space, even relatively inexpensive oil objectives have sufficient numerical aperture for imaging, since an NA of 1.25 which is very commonly available in low end objectives can be used very satisfactorily, especially for scanning applications at single wavelengths.

The goal of SP imaging is generally directed towards biological imaging in aqueous materials where the refractive index of the sample is, at least, 1.33 and usually a few percent more. For total internal reflection microscopy a numerical aperture greater than the refractive index of the final medium is generally satisfactory, although there are advantages in exceeding this by significant extent to reduce background signal from propagating waves, so a high quality immersion objective with numerical aperture of 1.4 or 1.45 is a good choice offering high numerical aperture, conventional immersion oil (n = 1.518) and inexpensive consumables.

For water based SP microscopy the situation is rather more problematic. For p-incident light impinging on a 43 nm thick gold surface with water, it can be seen that the angle of incidence where SPs are excited at 633nm is approximately 71.3 degrees. This means that a numerical aperture of approximately 1.44 is necessary to excite SPs. Even a 1.45NA objective does not have sufficient numerical aperture for SP imaging in water at visible wavelengths [112].

The solution is therefore either to use surface waves which are excited at smaller angles of incidence, such as SPs in gold at longer wavelengths, which on the other hand means increasing propagation length. The other approach is to use objectives with exceptionally high numerical apertures such as the Olympus 100x Apo with a numerical aperture of 1.65. To obtain such a numerical apertures high index immersion fluid and coverslips are required. The immersion fluid used has an index of 1.78 and this is about the highest index one can obtain before the fluids become seriously toxic. The coverslips used with this objective are sapphire.

Although the objective appears to function well the fluid and the coverslips make use of this objective less than ideal. The fluid is somewhat volatile using dissolved sulphur to increase the refractive index, the fluid therefore changes as the experiment proceeds making long term quantitative experiments inconvenient.

The other problem lies in the price of the coverslips that is nothing less than exhorbitant; it is possible to obtain well over 1000 conventional coverslips for the price of one sapphire version.

High numerical aperture lenses require a high index immersion media, since solids are available with much refractive higher indexes than liquids, the use of solid immersion lens (SILs) seems a natural means to achieve the high numerical aperture necessary for SP microscopy [113, 114].

6

In this chapter, we present a holographic setup for distortion-free simultaneous amplitude and phase SPR imaging (HoloSPRi). We built an inverted SPR microscope with a Mach-Zehnder interferometer placed in the detection-arm of the optical path. We can adopt this configuration because SPR excitation occurs only when the illuminating light is p-polarized, thus we can use the s-polarized component of light as reference beam. This way, we have realized a compact setup that can be easily implemented using conventional microscopes and which, minimizing the optical-path-difference between the two beams, suppresses the vibration noise during image detection [115].

Objective-based HoloSPRi technique offers the possibility of simultaneous detection of reflectivity and phase changes in SPR images. It extends, thus, the range of detectable samples and yields a higher throughput capacity in respect to both phase-contrast and amplitude-contrast imaging methods. In comparison with previous Holographic SPR imaging techniques, it avoids geometrical aberrations and limitations due to the use of a prism. Finally, the employment of a configuration similar to the widely used objective-type TIR, and the modular design keep it compatible with conventional microscopes, paving the way for an easy implementation with other optical techniques, from standard bright field microscopy to fluorescence.

6.1 IMAGING SURFACE PLASMON RESONANCE

If the optical detection unit of the SPR sensor is a Charge-Coupled Device (CCD) chip or any other type of array detector and the substrate is evenly illuminated with a large beam, the reflected light from the surface can be displayed as a two-dimensional image, in which each pixel depicts a part of the illuminated surface area. This type of sensor geometry is referred to as surface plasmon resonance imaging or surface plasmon microscopy and was first suggested by Knoll et al. in 1988 [37].

Another way of achieving lateral resolution is to narrow the illuminating beam and scan the substrate [38]. SPRi sensors can be based on intensity modulation in which case the wavelength and angle of incidence are fixed and the reflected intensities measured as functions of in plane position and/or time. The observed contrast in the SPR image is then obtained when different regions of the substrate have different refractive indices so that the resonance condition varies over the surface.

Alternatively, angular or wavelength spectra can be acquired for each depicted region of the substrate and the SPR angle or wavelength can be calculated to render an SPR map of the sample [116–118]60-61.

As for all optical microscopy techniques, the limit in resolution for SPRi is governed by diffraction. This means that the highest attainable lateral resolution is in the μm range, of the same order of magnitude as the wavelength of the light. Unfortunately, this only applies to the direction perpendicular to the plane of incidence.

In the direction of SP propagation, the resolution is limited by the plasmon propagation length. This is defined as the distance at which the intensity of the electric field has dropped to a value of $1/e$:

$$L_{SP} = \frac{1}{2\mathrm{Im}\{k_x\}} \, . \tag{6.1}$$

Since L_{SP} is inversely proportional to the sum of the radiative and internal damping (Γ_{rad} and Γ_i) and these in turn depend on the wavelength (from the dispersion relation), the propagation length will be different for different wavelengths.

METAL	WAVELENGTH (NM)	THICKNESS (NM)	L_{SP} IN AIR (μM)	L_{SP} IN WATER (μM)
gold	638	50	8.3	3.1
gold	532	50	0.5	0.2
copper	638	30	3.9	1.5

TABLE 1: Propagation length of SPs on gold and copper with different experimental conditions.
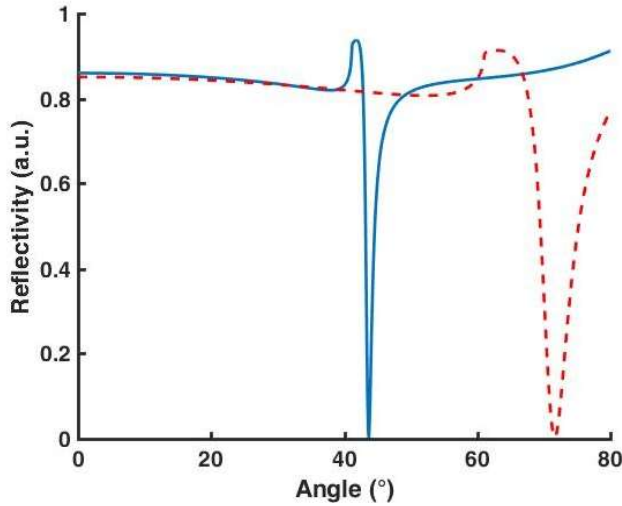
FIGURE 6.1: Amplitude of the reflection coefficient a gold layer of 50nm sputtered on glass, in air (slid line) and water (dashed line).

Table 1 shows that the propagation length for a wavelength of 638nm in an aqueous ambient is about an order of magnitude larger than the diffraction limit. This means that L_{SP} is the limiting factor in SPRi lateral resolution. Table 1 also shows that at lower wavelengths, in water, it is possible to get very close to the diffraction limit. This, however, comes at the price of an higher angle of incidence required to excite the plasmon resonance, see Fig.6.1.

6.1.1 Contrast mechanisms in SPR microscopy

In intensity mode SPRi the choice of wavelength and incidence angle have a large impact on the sensitivity and dynamic range.

In order to obtain contrast in an SPR image, it is necessary to select angles and wavelengths that lie on one of the flanks of the resonance curve. This can be attained with a multitude of combinations of wavelength and incidence angle.

In most cases, one strives to obtain as low an angle of incidence as possible. This is because the oblique angle in a simple SPRi configuration distorts the image, thereby leading to a reduced lateral resolution.

Since the SPR angle decreases with wavelength, it is then recommendable to work in the far red of the visible spectra.

Most CCD detectors, however, are designed to be less sensitive in the infrared posing a restraint on the choice of wavelength. The main reason for choosing shorter wavelengths lie, however, in the desire to have as short a propagation length as possible, as discussed in Section 6.1. The trade-off is then between propagation length and image distortion both of which affect the lateral resolution negatively.

In the Kretschmann geometry, with a wave length of 633nm in aqueous ambient, propagation lengths lie in the 10 μm range. This resolution is quite acceptable for most applications within biosensing but a limitation for imaging applications.

In terms of sensitivity or contrast in SPR imaging, many considerations need to be taken into account. First of all, SPR is sensitive to both bulk refractive index change and changes in refractive index or thickness of adsorbed thin films. This means that there are at least two separate sources that can give rise to contrast in an SPR image; local differences in refractive index or adsorbed molecules.

In most biosensing applications, the change in bulk refractive index is equal over the substrate and it is only molecular binding events that give rise to contrast. In this case, a relevant model system is the growth in thickness of a thin film adsorbed on the gold surface, or an increase in refractive index of an already present film.

Defining sensitivity as the slope of the calibration curve, for the cases described above:

$$S_n = \frac{\partial \Delta R}{\partial n_a} \ , \tag{6.2}$$

$$S_d = \frac{\partial \Delta R}{\partial d_f} \ , \tag{6.3}$$

$$S_{n_f} = \frac{\partial \Delta R}{\partial n_f} \ , \tag{6.4}$$

where n_a denotes refractive index of the ambient (bulk), d_f and n_f , thickness and refractive index of a surface film.

Figure 6.2 shows calculated reflectivity for different thicknesses of a gold layer sandwiched between glass and water. These calculations were made at a wavelength of 633nm. A dip in reflectivity is present only in a limited region of the plot, which means that a reasonable contrast is obtained only at certain conditions. In this case, the ideal thickness of the gold layer is around 50nm.

The numerical gradient of amplitude of the reflection coefficient plotted in Fig.6.3 shows a minimum in sensitivity in correspondence of the critical angle, θ_c. The maximum change in reflected intensity, conversely, is reached and the illumination at a slightly lower angle than θ_c. This is in agreement with theoretically derived findings by Yeatman et al. who found that the highest sensitivity (defined in terms of the slope of the SPR curve) is obtained at an angle offset from the resonance by $\Delta \phi = -\omega/\sqrt{3}$, where ω is the width of the resonance dip [119]. When sensitivity increases, however, the dynamic
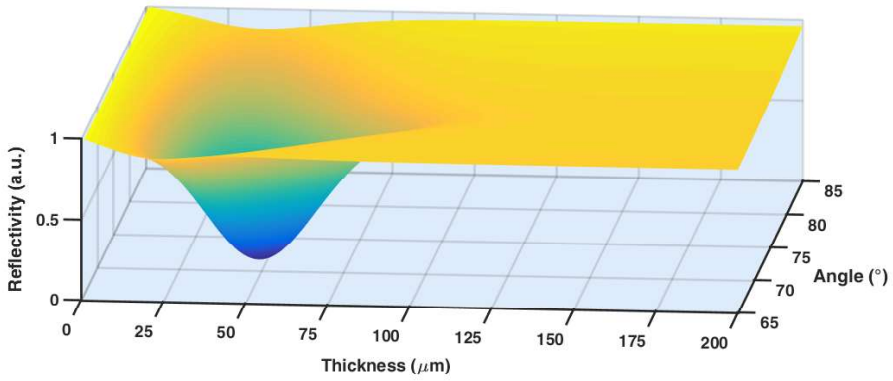
FIGURE 6.2: 3D plot showing the correlation between reflectivity, thickness of the gold layer and angle of incidence of light on the metal. The plot has been obtained by numerical simulation fixing the wavelength at 633nm and considering the gold placed between glass and water.
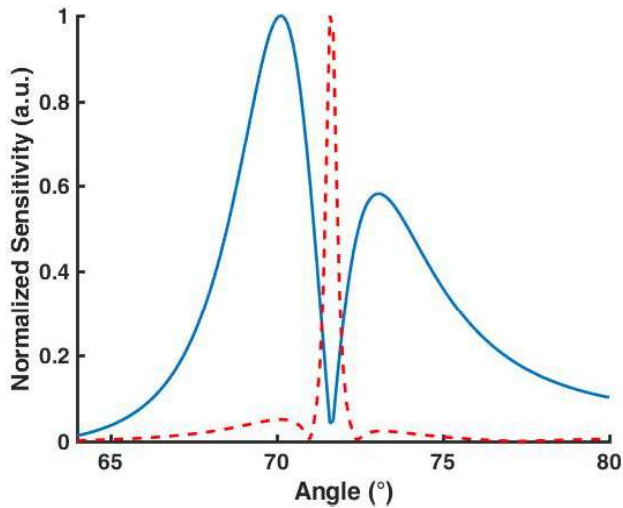
FIGURE 6.3: Comparison of the normalized sensitivity of SPR amplitude (solid line) and phase (dashed line) signal.

range of the SPR signal decreases, making a relinquishment in sensitivity beneficial for the dynamic range of the SPRi sensor.

On the other hand, the gradient of the phase of the reflection coefficient, Fig.6.3, has a different behavior. Actually, amplitude and phase gradients show a complementary range of sensitivity. This implies that measuring the complex reflection coefficient results in an extension of the dynamic range without loss of sensitivity.

6.2 HOLOGRAPHIC SPR MICROSCOPE

6.2.1 *Experimental Setup*

We designed the HoloSPRi microscope as an inverted microscope [120], see Fig.6.4. A 633nm He-Ne laser is coupled into a single-mode optical fiber (core size $c = 4\mu m$). The fiber output is collimated with a fiber collimator (OZ optics, f_c = 18mm) and then expanded using two plano-convex lenses (f_1 = 100mm and f_2 = 200mm). The estimated divergence angle is

$$DA = \frac{c}{f_c}\frac{f_1}{f_2} = 0.11\text{mrad} .$$

$$(6.5)$$

Light is converted to p-polarization by a linear polarizer. The beam passes through a *lambda*/2 plate, where polarization can be rotated, and then is focused by an achromatic lens (f_L = 200mm) to the back focal plane of a high numerical aperture objective (Nikon Plan Apo 60x NA 1.49), and finally emerges from the objective as a parallel beam. The radius of the focal spot is estimated

$$\Delta d = \frac{DA}{2}f_L = 11\mu m.$$

$$(6.6)$$

In the detection arm, a polarizing cube is placed to laterally split the s- and p-polarization components of reflected light. The s-polarized beam, carrying no information, acts as the reference arm of the interferometer. It passes through another $\lambda/2$ plate, which rotates its polarization by 90 degrees, converting it in a p-polarized beam, allowing, in this way, the interference with the object beam, and, thus, the formation of the holographic images. The interference pattern of the two beam is recorded in a CCD camera (UI-1550SE, 1.92MPix, pixel size: 2.8μm) and analyzed by numerical processing. The exit angle θ of the laser beam from the objective is changed using a linear translation stage and calculated by the sine condition of an aplanatic optical system:

$$d = f_{ob}\sin(\theta) ,$$

$$(6.7)$$
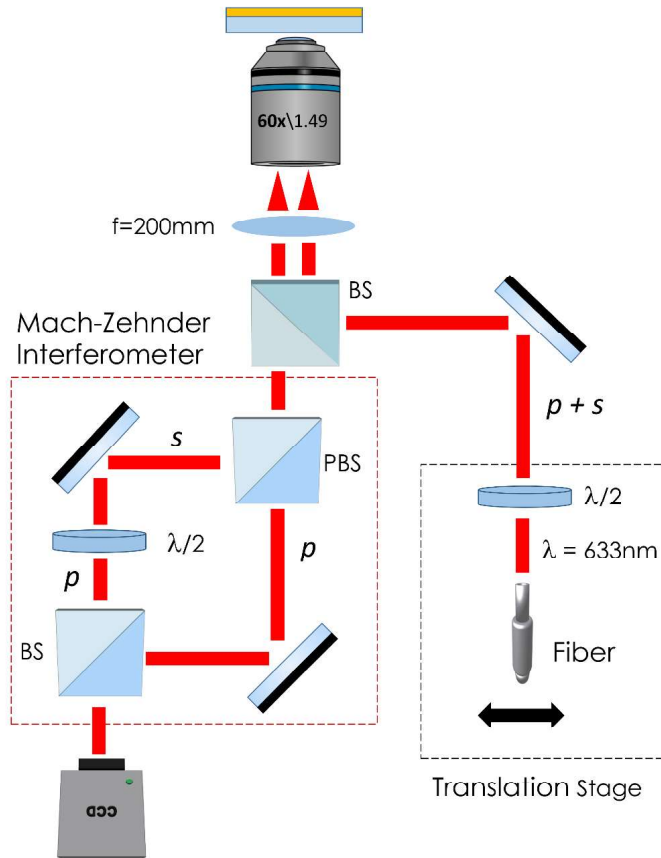
FIGURE 6.4: HoloSPR Imaging Setup. BS: Beam Splitter cube. PBS: Polarizing Beam Splitter cube. $\lambda/2$: Half-wave plate.

where d is the lateral displacement of the stage and f the objective focal length. The error in θ due to the finite focal spot size at the objective back focal plane is given by:

$$\Delta\theta = \frac{1}{\sqrt{1 - \sin^2\theta}} \frac{\Delta d}{f_{ob}} \; . \tag{6.8}$$

In our setup at 45° the expected error is $\Delta\theta$ = 4.8mrad.

6.2.2 Numerical reconstruction

The recorded intensity $I_H(x_H, y_H)$ at the hologram plane is the square module of the amplitude superposition of the object and reference waves. It is given by:

$$I_H(x_H, y_H) = |O_0(x_H, y_H)|^2 + |R_0|^2 + O_0^*(x_H, y_H)R_0 + O_0(x_H, y_H)R_0^* \tag{6.9}$$

The first two terms represent the intensities of the reference and object waves, respectively. They do not provide spatial information about the object optical field and form the zero-order term. The last two terms provide spatial frequency of the recorded hologram and are responsible for the virtual and real images, respectively. We reconstructed holograms by numerically propagating the optical field along the z direction using the angular spectrum method, which has a significant advantage in that it has no minimum reconstruction distance requirement. If $E(x, y; 0)$ is the wavefront at plane z=0, the angular spectrum $A(\xi, \eta; 0) = FE(x, y; 0)$ at this plane is obtained by taking the Fourier transform, where F denotes the Fourier transform; ξ and η are the corresponding spatial frequencies of x and y directions, respectively; and z is the propagation direction of the object wave. The new angular spectrum A at plane z=d is calculated from $A(\xi, \eta; 0)$ as:

$$A(\xi, \eta; d) = A(\xi, \eta; 0) \cdot \exp\{j\frac{2\pi d}{\lambda}[1 - (\lambda\xi)^2 - (\lambda\eta)^2]^2\} \tag{6.10}$$

The reconstructed complex wavefront at plane z=d is found by taking the inverse Fourier transform as

$$E(x, y; d) = F^{-1}A(\xi, \eta; d) \tag{6.11}$$

where $F^{-1}\{\}$ denotes the inverse Fourier transform. The intensity image $I(x, y; d)$ and phase image $\phi(x, y; d)$ are simultaneously obtained from a single digital hologram by calculating the square module of the amplitude and the argument of the reconstructed complex wavefront [121]:

$$I(x, y; d) = |E(x, y; d)|^2 \tag{6.12}$$

$$\phi(x, y; d) = \arctan\left(\frac{\text{Im}[E(x, y; d)]}{\text{Re}[E(x, y; d)]}\right) \tag{6.13}$$
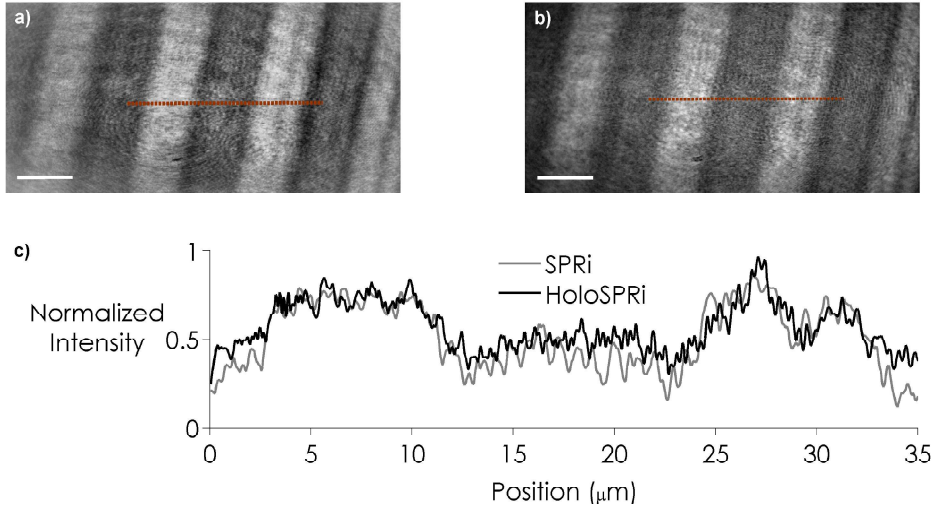
FIGURE 6.5: The Amplitude Reconstruction accurately matches the Original Image. a) Conventional SPR image of Photoresist Pattern. b) Amplitude reconstruction. c) Comparison between the intensity profiles of the two images in correspondence of the dashed line. Scale bar 10μm.

The resolution of the reconstructed images from the angular spectrum method is the same as that in the hologram plane [122]. We can assume that the reflectivity is 1 when the amplitude of object wave is a maximum so the reflectivity of amplitude r can be defined as the normalization of $I(x, y; d)$ [123].

6.2.3 *Testing imaging performance*

The setup uses an oil immersion objective having a NA of 1.49. Using this objective, when the incident light is shifted to the edge of the objective back aperture, it will reach the sample at an angle that is larger than the critical angle up to a nominal maximum angle of 79.6°. The large angle coverage allows adjusting the SPR excitation conditions to obtain the image contrast and sensitivity that best fits a wide range of samples.

Comparison with standard through-the-objective SPRi. In order to evaluate the reliability of the amplitude contrast images obtained by numerical reconstruction, we compared them with conventional amplitude contrast SPR images (recorded turning off the reference beam) using Photoresist patterns on gold surface as a sample, Fig.6.5a,b. The incident angle was fixed close to the SPR minimum angle of air interface. The comparison of the intensity profiles in correspondence of the photoresist shows no significant differences between the two images, proving, thus, the reliability of the numerical reconstruction,
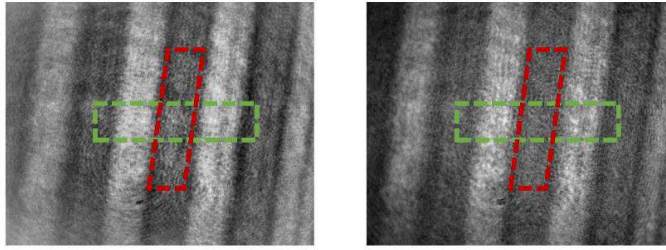
FIGURE 6.6: Evaluation of the SNR of two reflectivity maps obtained by standard (left), and holographic (right) SPRi.
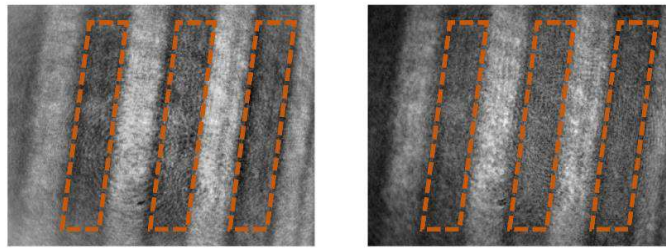
FIGURE 6.7: Comparison of speckle noise between two reflectivity maps obtained by standard (left), and holographic (right) SPRi.

Fig.6.5c. Furthermore, the reduction of coherent noise in the reconstruction returns an increase of 20% in signal-to-noise ratio (SNR) for HoloSPRi and a Speckle Index improvement of 39%.

For each image we evaluated the SNR comparing the variance of the signal in two 750x150 pixels area at the center of the images taken along the direction perpendicular and parallel to the lines, respectively green and red areas in Fig.6.6. Given the absence of photoresist in between the lines, we consider the variance in red areas dominated by noise. We assume a homogenous noise distribution all over the image.

The comparison of speckle noise was also carried out calculating the standard deviation in low signal zones, see Fig.6.7. The holographic reconstruction yields a speckle index 39% lower than SPR image. All the calculations are reported in Table.
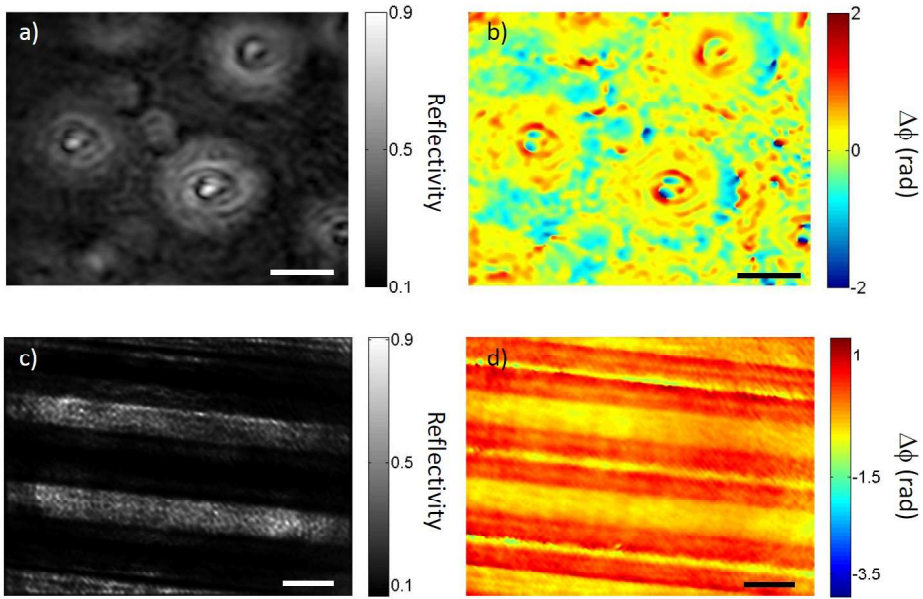
FIGURE 6.8: Digital holography allows simultaneous retrieval of am-plitude and phase contrast images. Photore-sist domes pattern: am-plitude-contrast image, a), and phase-contrast image, b). Photore-sist lines pattern: amplitude-contrast image, c), and phase-contrast image, d). Scale bar 10μm.

6.3 EXPERIMENTAL RESULTS

6.3.1 *Simultaneous amplitude and phase-contrast SPR imaging*

SPR imaging can be useful when it comes to measure the thickness of a film on a surface. It has, in fact, a resolution in the axial direction of few nanometers, which it is helpful to reveal small features such as unevenness in flat surfaces or imperfections in a specific pattern. We used HoloSPRi to obtain simultaneous amplitude and phase contrast images of two polymeric patterns [120]. The first pattern was made by domes of 10μm diameter while the second one was made by a series of lines with a spacing of 10μm, Fig.6.8a-d.

Standard 10x10mm glass substrates have been cleaned in acetone and 5 minutes in an ultrasound bath. After that, they have been coated with gold 50nm thin by means of mag-netron sputtering then a positive photoresist (Microresist mp-1210) has been spin coated on the gold surface. Finally, conventional mask lithography has been used to pattern 10um wide lines and domes.

Not ideal conditions in the photolithographic process can give rise to irregularities in the pattern and the presence of local defects in the polymeric film. We took advantage of

this to show how such irregularities can be clearly observed with SPR imaging and how amplitude and phase contrast images underline different features of the same sample. Fig.6.8c and d are a clear example of this issue. Indeed, while the phase map in Fig.6.8d seems neater in comparison with the amplitude map in Fig.6.8c, it also shows three sharp lines whereas in the latter there is no signal. This is due to an ambiguity in SPR response, which can be mostly overcome, with a wise choice of the experimental conditions, by the simultaneous collection of amplitude and phase images obtained with HoloSPRi.

6.3.2 *Quantitative Surface Mapping*

The complementarity of information given by amplitude and phase in SPR imaging is not only limited to the determination of ambiguities in image interpretation but it extends further to sensitivity. In principle, then, it is possible to take advantage of this feature and to merge both amplitude and phase information to construct a synthetic 3D map with enhanced sensitivity.

As already shown in Section 6.1, the excitation of SPs on a metal layer implies a change in intensity and phase of the reflection coefficient for p-polarized light. This change is described by Fresnel equations. However, neither reflectivity nor phase are bijective functions of sample height. This hinders the possibility to retrieve a 3D profile starting from SPR data without any previous knowledge of the sample. Fortunately, we can overcome this limit providing both reflectivity and phase data of the same sample.

As a proof-of-concept, here we show how the 3D profile of a polymeric film placed above the gold substrate can be retrieved which uses both reflectivity and phase information can improve the profile accuracy. We placed the sample on the microscope and changed the angle of incidence of light, θ, until an area of low reflectivity appeared, Fig.6.9. This occurred at $\theta = 45$ which is higher than the SPR critical angle for air ($\theta = 43, 6$) proving that a thin layer of photoresist is present throughout the imaged area and the minimum height is around 5nm. This can be deduced from the behavior of the refractive index with the thickness of the photoresist layer depicted in Fig.6.10, which was simulated using Fresnel equations with experimental parameters, see Appendix B.

Evaluating photoresist height, then, we can reject all values lower than 5nm. Thus, reflectivity is a locally bijective function of height for values lower than 0.8, blue area in Fig.6.10, viceversa where reflectivity is higher than 0.8, height can be unambiguously retrieved from phase data, red area in Fig.6.10. Following this rule we obtained a synthetic 3D map of the sample, see Fig.6.11.

A profile obtained by profilometry measurements (Dektak XT 2011) of the photoresist lines was compared with a profile from an amplitude-contrast, phase-contrast and synthetic map respectively, see Fig.6.12.

Correlation analysis and square-error-analysis are summarized in Table 2. They show a good fit in the case of the profile retrieved from holographic measurements and, by the
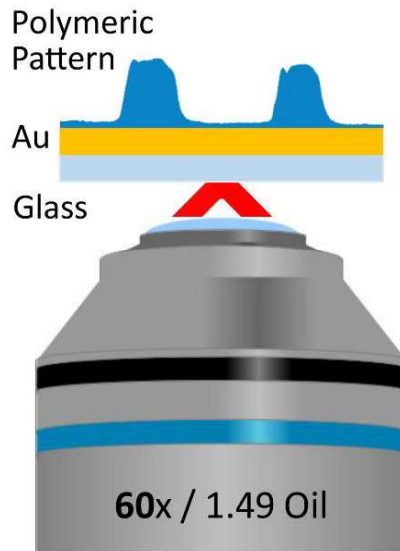
FIGURE 6.9: Mapping of a polymeric pattern by HoloSPRi: schematic depiction of the experiment.
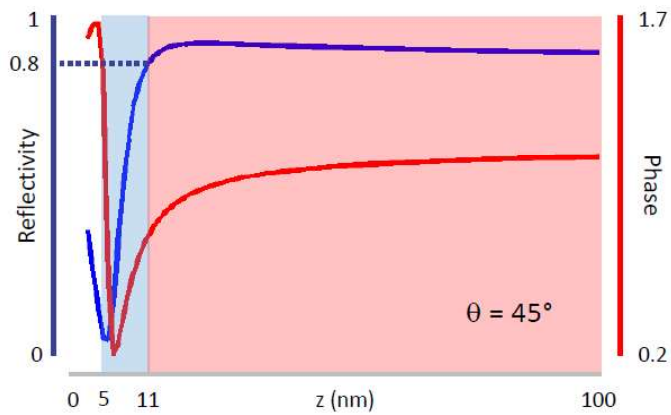
FIGURE 6.10: Simulation of the response of the SPR signal in the case of the experiment depicted in Fig.6.9. Amplitude (blue) and phase (red) of the reflection coefficient as a function of the film thickness.
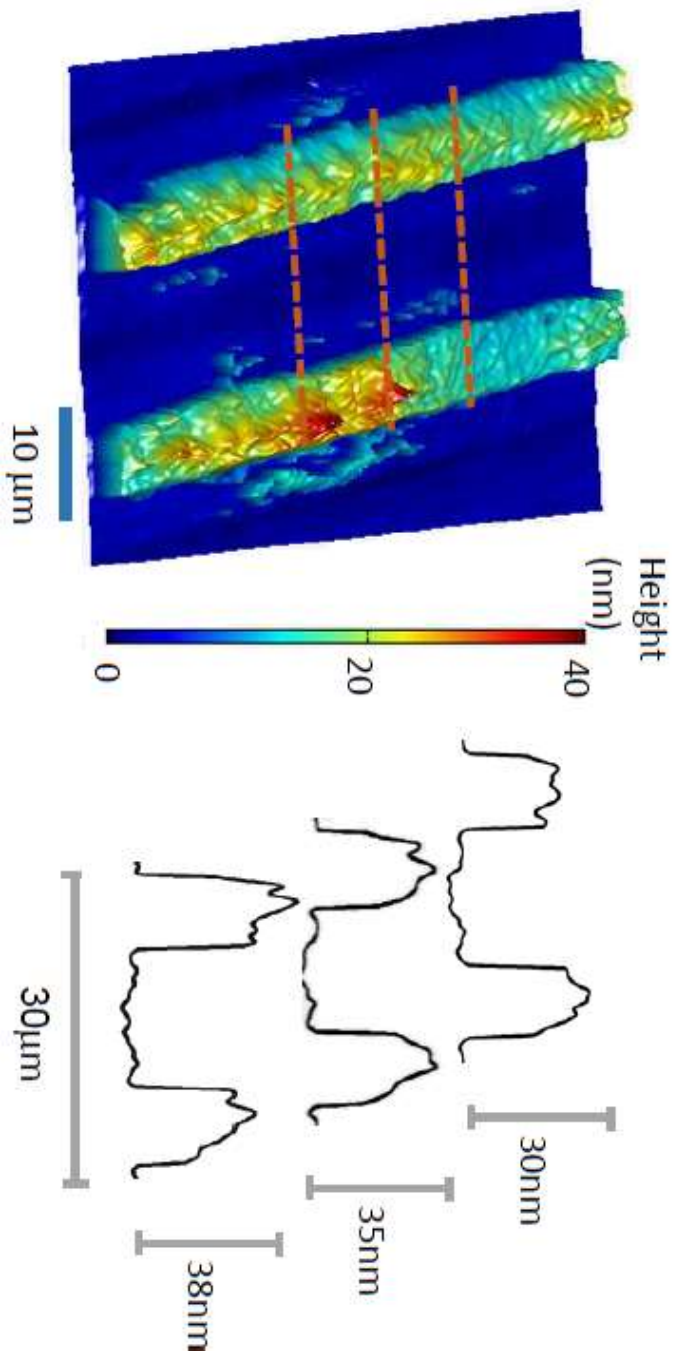
Figure 6.11: Synthetic 3D map of photoresist lines obtained merg-ing the amplitude and phase-contrast images in Fig.6.8a,b (left). Plot of the profiles corre-sponding to the dashed lines at the center of the map (right).
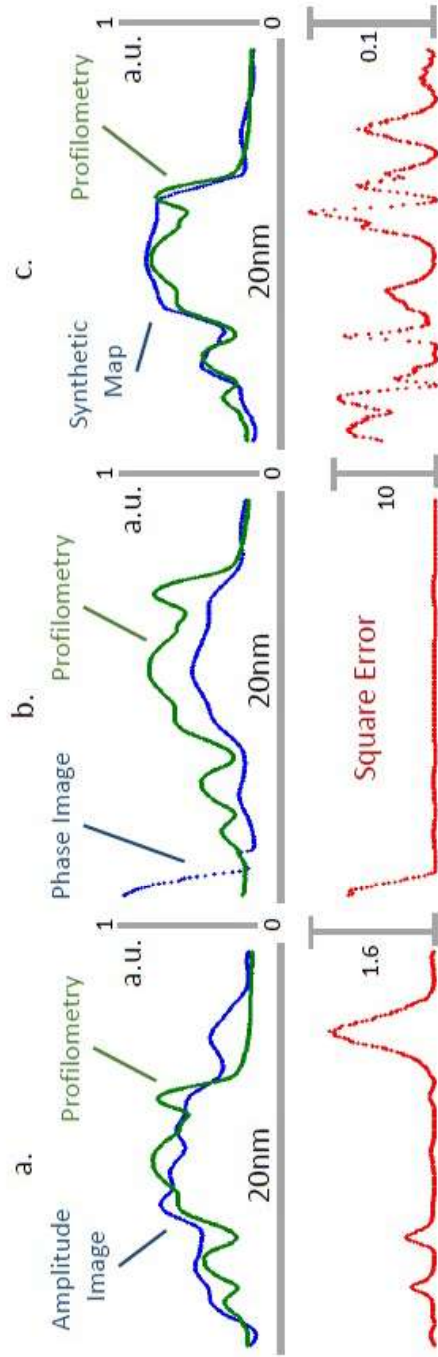
FIGURE 6.12: Profiles of a photoresist line obtained by amplitude (a) and phase-contrast (b) images and from the synthetic map (c). All three profiles are compared with one measured by profilometry (blue line). In red: Square errors relative to each profile calculated pixel by pixel.

way, a better agreement respect to the profiles calculated using only amplitude or phase data.

PROFILE	CORRELATION COEFFICIENT	SQUARE ERROR		
		MEAN	MODE	MAX
Amplitude	0.83	0.19	2.53×10^{-9}	1.6
Phase	0.47	0.47	9.06×10^{-7}	10
Synthetic	0.94	0.03	1.70×10^{-7}	0.1

TABLE 2: Comparison of profiles obtained from an amplitude-contrast, phase-contrast and synthetic maps with a profile obtained by profilometry.

6.3.3   *Kinetic measurements of droplet evaporation*

Simultaneous acquisition of amplitude and phase contrast images can be useful also in kinetic measurements. We have monitored, then, the evaporation of a drop of DMEM (Dulbecco's Modified Eagle Medium) in real time. The droplet was deposited on the surface of a gold-coated coverslip illuminated at an incident angle of about 60 degrees and a series of holograms of the evaporating droplet were taken every 0.42s. Fig.6.13a-d show the amplitude and phase reconstructions at the beginning and the end of measurements. The refractive index of a solution approximately shows a linear behavior with concentration. While evaporation takes place, the solute concentration rises, producing an increase of refractive index. This increase can be detected by SPR imaging to obtain a qualitative behavior of concentration in time, see Fig.6.13e.
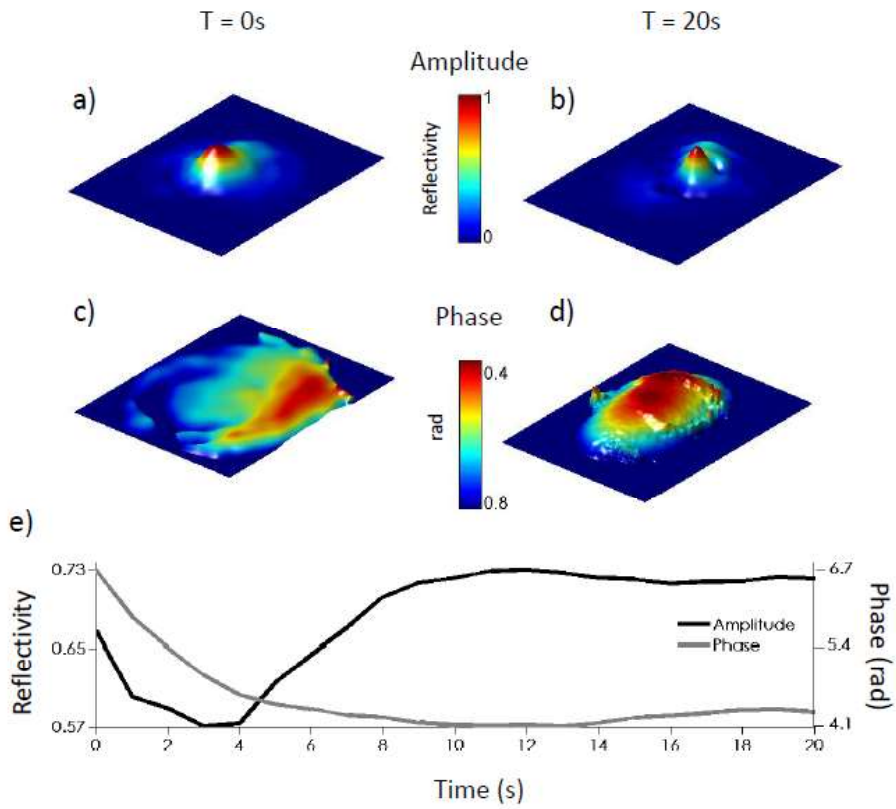
FIGURE 6.13: Evaporation of a DMEM droplet. Reconstructions of the amplitude and phase-contrast SPR images at T=0s, a) and c) re-spectively, and T=20s, b) and d) respectively. e) Reflectivity and Phase were calculated at the center of the droplet.

CONCLUSIONS

C URRENTLY, high-resolution information on the interactions of living cells with bio-materials is achieved mainly through SPRi or TIRF Microscopy. The former is a well-known label-free technique, while the latter is widely spread in the field of fluorescence imaging.

Since its invention in 1988, SPRi has become a powerful tool to image subtle interfacial features by means of refractive index contrast. Detecting changes in refractive index allows the monitoring of biomolecular interactions as well as two-dimensional imaging. The high sensitivity of SPRi has made it a good tool to study thin films or to measure the rate of biomolecular binding events, usually on DNA or protein microarrays,

On the other side, TIRF allows for selective illumination of a very thin region directly above the substrate and provides very high-contrast images of sub-micron particles and the cell membrane. Nevertheless, quantitative measurements of cell/substrate distances require the implementation of complex setups.

To study cell contact formation and affinity with biomaterials prism-less TIR microscopy would be optimal. It has a short penetration length, comparable to super-resolution techniques, combined with high throughput capabilities, due to the fact that it does not require cell labeling. However, it is seldom used in live cell imaging, mainly because its resolution along the third dimension it is still limited for practical applications. This is why usually other techniques, namely TIRF or SPRi, are preferred.

This doctoral project was devoted to the development and application of novel DHM setups to different fields of applications, such as characterization of polymeric materials, microfluidics, and cell biology. A main focus, however, was given to the study and implementation of digital holography of total internal reflection. Here we have shown the devices that were developed and the improvements that they mark over the state-of-art label-free evanescent wave microscopy. In particular, the grater sensitivity of quantitative phase imaging, especially within the first 50-100nm from the interface, which is the most interesting separation range from a biological point of view.

In summary, we have designed and built a two novel microscopy techniques for quantitative phase imaging of total internal reflection. We have used the HoloTIR microscope to study the formation of focal contacts of fibroblasts on three substrates with different levels of affinity for cell adhesion. It is has been demonstrated that detection sensitivity of HoloTIR is suitable for label-free study of focal contacts and, likely, of cell/substrate interaction in general. Also the simplicity of implementation and relative low cost, due to the requirement of less optical components, make HoloTIR a reasonable alternative, or

even an addition, to TIRF microscopy for mapping cell/substratum topography. It can be especially valuable to study the biocompatibility of a different functionalized substrates, where large amounts of data are required and the option of long time-lapse imaging is an asset.

The study of cell adhesion on different substrates evidenced an actual sensitivity enhancement for HoloTIR microscopy. Experimental data show a more accurate detection of focal contacts in comparison with conventional TIR microscopy.

HoloTIR microscopy, moreover, has the advantages of being relatively easy to implement on commercial microscopes, and generally cheaper than its fluorescence counterpart. There is no requirement, in fact, for any fluorescent marker and, consequently, for expensive filters or cameras. Sample preparation time is reduced with a resulting improvement of data throughput and the absence of labels avoids the photobleaching issues for time-lapse imaging. Furthermore, illuminating light is mostly recovered by the camera, which allows for low-light imaging with subsequent reduction of phototoxicity damage for long time exposures of biological samples [44,45].

Objective-based HoloSPRi technique offers the possibility of simultaneous detection of reflectivity and phase changes in SPR images. It extends the range of detectable samples and yields a higher throughput capacity in respect to both phase-contrast and amplitude-contrast imaging methods. This is because SPRi methods usually must scan the sample in order to retrieve quantitative information. We have shown that with HoloSPRi is possible to perform quantitative measurements without any angular or planar scanning, thanks to the fact that the whole complex reflection coefficient is measured. In comparison with previous attempts of Holographic SPR imaging, it avoids geometrical aberrations and limitations due to the use of a prism. Finally, the employment of a configuration similar to the widely used objective-type TIR, and the modular design keep it compatible with conventional microscopes, paving the way for an easy implementation with other optical techniques, from standard bright field microscopy to fluorescence

Further developments can include methods to overcome the limitations of HoloTIR and HoloSPRi. A major concern, for example, is the uniformity of illumination. Non-ideal illumination patterns can be due to imperfections in the objective such as image fingerprinting or limited effective numerical aperture [101], that is why a high numerical aperture TIRF objective is highly recommended. Also the average-only knowledge of cell refractive index is a source of indetermination in distance assessment. All these issues, however, are shared also with TIRF microscopy, where they are solved by means of azimuthal and incident angle scanning [124–127]. These same strategies can be perfectly applied to the label-free setup, where they can be also used to improve the lateral resolution [48, 128], paving the way for future developments towards label-free 3D super-resolution microscopy for the imaging of interfaces.

Part IV

APPENDIX

A

ESTIMATION OF FOCAL ADHESION AREA

A.1 LABEL-FREE MEASUREMENTS

Once reconstructed the holographic acquisitions, both reflectivity and phase-contrast images were filtered with a threshold corresponding to the total internal reflection detection limit. From the theoretical curves reported in Fig.4.1, the threshold values correspond to 0.81a.u. and -0.73rad for reflectivity and phase respectively. The actual magnification of the HoloTIR setup is 120x. This means that entire cells do not fall into a single field of view. Hence, in order to obtain a wider field of view of the samples, more images were acquired moving the sample of a known distance. This distance was set at 20μm to ensure an appropriate overlapping when the images were stitched together.

A.2 TIRF MEASUREMENTS

To quantify the focal adhesion area of fibroblasts, we imaged talin clusters at the basal membrane with TIRF microscopy. For each image the fluorescence background was removed and the number of remaining bright pixels calculated. Finally, the area of focal adhesion was estimated considering that each pixel represents an area of $0.005\mu m^2$. Sample fluorescence images are depicted in Fig.A.2.

The cell adhesion on surfaces was evaluated in vitro using mouse embryonic fibroblast (NIH-3T3). NIH-3T3 cells were grown in Petri dishes in Dulbecco's modified Eagle's medium (DMEM) containing 4.5 g/L D-glucose and supplemented with 10% FBS (fetal bovine serum), 100 units/mL penicillin, and 100 μg/mL streptomycin. Subsequently, they were harvested from the tissue culture flasks by incubation with a 0.05% trypsin–EDTA solution for 5 min. The cells were then centrifuged, resuspended in a complete medium, and then seeded on coated surfaces (FN and PLL) and on WillCo-dish® Glass Bottom dish at a density of 1x104 cells/mL, at 37 °C and in humidified 5% CO2 atmosphere. The cell adhesion and spreading was observed over 24h. After incubation, the medium was aspirated and the samples were rinsed with PBS and fixed in 4% paraformaldehyde solution for 10 minutes at room temperature. The samples were then washed and permeabilized with 0.1% Triton X-100 in PBS for 5 min and blocking solution (1% BSA in PBS) for 30 min. Immunostaining with antitalin antibody was carried out in order to visualize further the
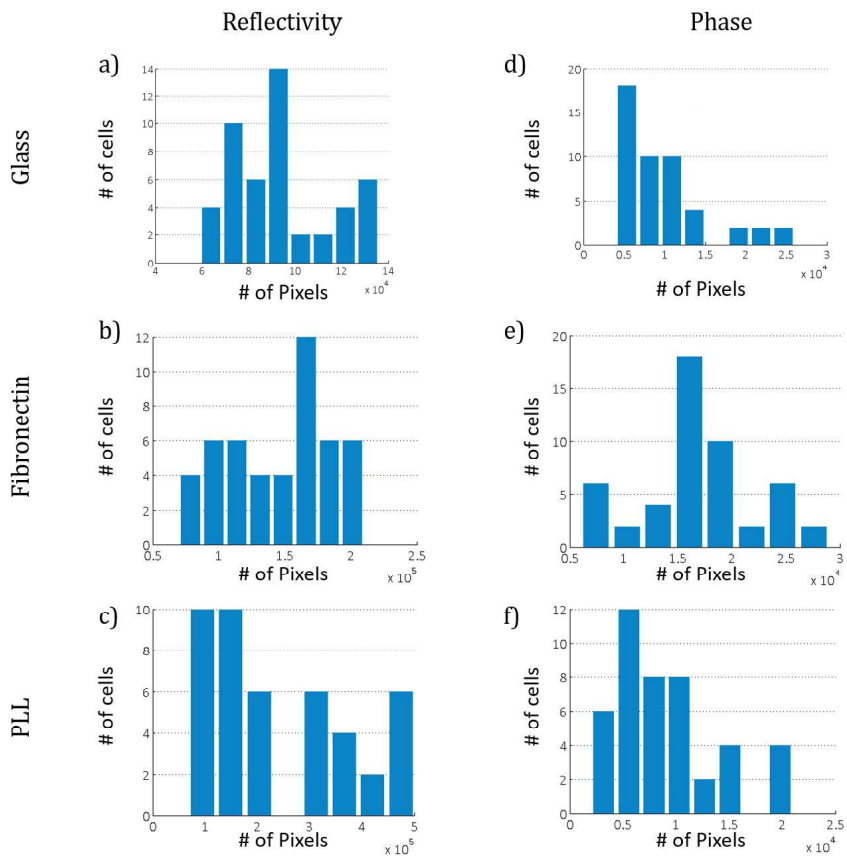
FIGURE A.1: Estimation of focal adhesion area from reflectivity data of cells on glass (a), fibronectin (b), and PLL (c). Focal adhesion area estimation obtained by phase data of cells on glass (d), fibronectin (e), and PLL (f).
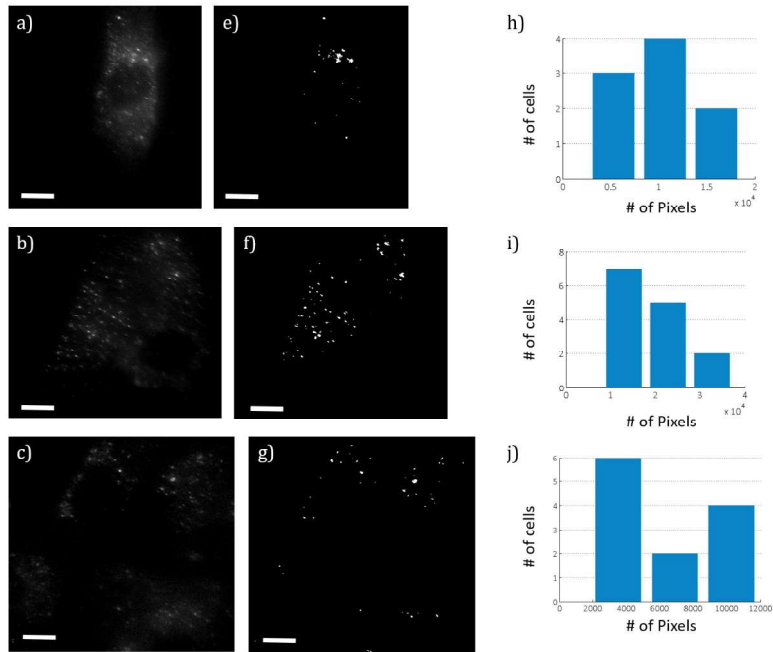
FIGURE A.2: TIRF images of talin aggregates on glass (a), fibronectin (b), and PLL (c) were acquired. In order to estimate the extent of focal adhesion on the different substrates the background was calculated and subtracted from each image (e-g). The Focal adhesion area distribution for each substrate is plotted in (h-j).

actin-based cytoskeleton in the cell-cell and cell-substrate junctions. NIH-3T3 cells were incubated first in a primary antitalin antibody (Biorbyt Limited, UK) diluted in blocking solution for 1 h, and then in a secondary donkey antirabbit TRITC conjugated (Thermo Scientific, USA) at 1:200 dilution in blocking buffer solution for 45 min. The samples were washed three times in PBS between each antibody treatment.

B

A generic optical layout for SPRi is composed by:

- a microscope objective or prism;
- a coverslide;
- a gold film;
- a layer of sample;
- a certain buffer.

The sequence of the optical media from objective to buffer are denoted by medium 0, 1, 2, 3 and 4. The directions of the coordinate system are denoted by x and z.

The symbol R represents the total reflection ratio of the light system. It is clear that R is the function of the light wavelength λ, the dielectric constant $\varepsilon_i (i = 0, 1, \ldots, 4)$ of the media and the medium thickness $d_i (i = 0, 1, \ldots, 4)$. The critical incident angle is $\theta_c = \arcsin(n_1/n_0)$, which is wheere total internal reflection occurs. Under the total internal reflection condition, the light intensity does not fall to zero across the interface, instead there is an evanescent wave with an amplitude decaying exponentially normal to the interface. Below a certain angle of incidence, θ_{SPR}, SPs at the interface of the metal and dielectric are excited by the evanescent wave. θ_{SPR} represents a resonance angle corresponding to a peak of a SPR spectrum.

According to the geometry of the SPR system, it is possible to describe the relation between the reflection coefficient $r_{0,4}$ and the thickness of the layer of sample, d_3.

$$r_{i,4}(\theta) = \frac{r_{i,i+1}(\theta) + r_{i+1,4}(\theta)\exp(2jd_{i+1}k_{i+1}^z(\theta))}{1 + r_{i,i+1}(\theta) \cdot r_{i+1,4}(\theta)\exp(2jd_{i+1}k_{i+1}^z(\theta))} \quad (i = 2, 1, 0) \qquad \text{(B.1)}$$

where

$$r_{i,i+1}(\theta) = \frac{\xi_{i+1}(\theta) - \xi_i(\theta)}{\xi_{i+1}(\theta) + \xi_i(\theta)} \quad (i = 0, 1, 2, 3) \qquad \text{(B.2)}$$

$$\xi_i(\theta) = \frac{\varepsilon_i}{k_i^z(\theta)} \quad (i = 0, 1, \ldots, 4) \qquad \text{(B.3)}$$
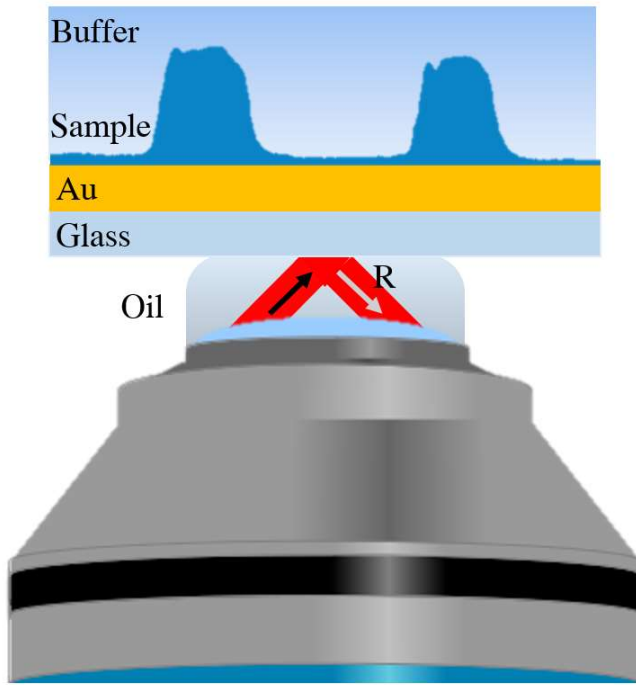
Figure B.1: A schematic view of the optical system of SPRi.

$$k_i^z(\theta) = \frac{2\pi}{\lambda} \sqrt{\varepsilon_i - \varepsilon_0 \sin^2(\theta)} \qquad (B.4)$$

In the practical case, almost all the parameters of the system are constant. If we fix the angle of incidence we can retrieve from Equation B.1 the behavior of reflection coefficient $r_{0,4}$ with thickness of the sample layer, d_3. From the reflection coefficient both amplitude, i.e. reflectivity, $R(\theta)$ and phase, $\phi(\theta)$, can be retrieved:

$$R(\theta) = |r_{0,4}(\theta)|^2 \quad , \quad \phi(\theta) = \Im r_{0,4}(\theta) \,. \qquad (B.5)$$

LIST OF FIGURES

LIST OF TABLES

BIBLIOGRAPHY

[1] Laurent Blanchoin, Rajaa Boujemaa-Paterski, Cécile Sykes, and Julie Plastino. "Actin dynamics, architecture, and mechanics in cell motility." In: *Physiological reviews* 94.1 (2014), pp. 235–63. ISSN: 1522-1210. DOI: 10.1152/physrev.00018.2013. URL: http://www.ncbi.nlm.nih.gov/pubmed/24382887.

[2] Song Li, Jun-Lin Guan, and Shu Chien. "Biochemistry and biomechanics of cell motility." In: *Annual review of biomedical engineering* 7 (2005), pp. 105–150. ISSN: 1523-9829. DOI: 10.1146/annurev.bioeng.7.060804.100340.

[3] Christopher S Chen. "Mechanotransduction - a field pulling together?" In: *Journal of cell science* 121.Pt 20 (2008), pp. 3285–92. ISSN: 0021-9533. DOI: 10.1242/jcs.023507. URL: http://www.ncbi.nlm.nih.gov/pubmed/18843115.

[4] Andrew S. LaCroix, Katheryn E. Rothenberg, and Brenton D. Hoffman. "Molecular-Scale Tools for Studying Mechanotransduction." In: *Annual Review of Biomedical Engineering* 17.1 (2015), annurev–bioeng–071114–040531. ISSN: 1523-9829. DOI: 10.1146/annurev-bioeng-071114-040531. URL: http://www.annualreviews.org/doi/10.1146/annurev-bioeng-071114-040531.

[5] Tyler D. Ross, Brian G. Coon, Sanguk Yun, Nicolas Baeyens, Keiichiro Tanaka, Mingxing Ouyang, and Martin A. Schwartz. "Integrins in mechanotransduction." In: *Current Opinion in Cell Biology* 25.5 (2013), pp. 613–618. ISSN: 09550674. DOI: 10.1016/j.ceb.2013.05.006. arXiv: NIHMS150003. URL: http://dx.doi.org/10.1016/j.ceb.2013.05.006.

[6] David F. Williams. "On the mechanisms of biocompatibility." In: *Biomaterials* 29.20 (2008), pp. 2941–2953. ISSN: 01429612. DOI: 10.1016/j.biomaterials.2008.04.023.

[7] Soo Ryoon Ryoo, Young Kwan Kim, Mi Hee Kim, and Dal Hee Min. "Behaviors of NIH-3T3 fibroblasts on graphene/carbon nanotubes: Proliferation, focal adhesion, and gene transfection studies." In: *ACS Nano* 4.11 (2010), pp. 6587–6598. ISSN: 19360851. DOI: 10.1021/nn1018279.

[8] Valentina Marchesano, Oriella Gennari, Laura Mecozzi, Simonetta Grilli, and Pietro Ferraro. "Effects of Lithium Niobate Polarization on Cell Adhesion and Morphology." In: *ACS Applied Materials & Interfaces* 7.32 (2015), pp. 18113–18119. ISSN: 1944-8244. DOI: 10.1021/acsami.5b05340. URL: http://pubs.acs.org/doi/abs/10.1021/acsami.5b05340.

[9]   J S Burmeister, L a Olivier, W M Reichert, and G a Truskey. "Application of total internal reflection fluorescence microscopy to study cell adhesion to biomaterials." In: *Biomaterials* 19.4-5 (1998), pp. 307–25. ISSN: 0142-9612. DOI: 10.1016/S0142-9612(97)00109-9. URL: http://www.ncbi.nlm.nih.gov/pubmed/9677147.

[10]   C S Izzard and L R Lochner. "Cell-to-substrate contacts in living fibroblasts: an interference reflexion study with an evaluation of the technique." In: *Journal of cell science* 21.1 (1976), pp. 129–159. ISSN: 0021-9533.

[11]   Frederick Lanni, Alan S Waggoner, and D Lansing Taylor. "Structural Organization of Interphase 3T3 Fibroblasts Studied by Total Internal Reflection Fluorescence Microscopy." In: (1985), pp. 1091–1102.

[12]   Wen-tien Chen and S J Singer. "Immunoelectron Microscopic Studies of the Sites of Cell- Substratum and Cell-Cell Contacts in Cultured Fibroblasts." In: *The journal of cell biology* 95 (1982), pp. 205–222. DOI: 10.1083/jcb.95.1.205.

[13]   T Funatsu, Y Harada, M Tokunaga, K Saito, and T Yanagida. "Imaging of single fluorescent molecules and individual ATP turnovers by single myosin molecules in aqueous solution." In: *Nature* 374.6522 (1995), pp. 555–559. ISSN: 0028-0836. DOI: 10.1038/374555a0. URL: http://www.ncbi.nlm.nih.gov/pubmed/7700383http://www.nature.com/nature/journal/v374/n6522/abs/374555a0.html.

[14]   Yasushi Sako and Takeshi Uyemura. "Total Internal Reflection Fluorescence Microscopy for Single-molecule Imaging in Living Cells Total internal reflection fluorescence micro- scopy for detecting single-molecules in living cells." In: *Cell Structure and Function* 27 (2002), pp. 357–365. ISSN: 03867196. DOI: 10.1247/csf.27.357.

[15]   Daniel Axelrod. "Total Internal Reflection Fluorescence Microscopy in Cell Biology." In: 2 (2001), pp. 764–774.

[16]   Joshua Z Rappoport and Sanford M Simon. "Real-time analysis of clathrin-mediated endocytosis during cell migration." In: *J Cell Sci* 116 (2003), pp. 847–855. ISSN: 0021-9533 (Print) 0021-9533 (Linking). DOI: 10.1242/jcs.00289. URL: http://www.ncbi.nlm.nih.gov/pubmed/12571282http://jcs.biologists.org/content/116/5/847.full.pdf.

[17]   D Axelrod. "Cell-substrate contacts illuminated by total internal reflection fluorescence." In: *The Journal of cell biology* 25.23 (1981), p. 4228. ISSN: 0003-6935. URL: http://www.ncbi.nlm.nih.gov/pubmed/24019187http://jcb.rupress.org/content/89/1/141.abstract.

[18]   Alison J. North. "Seeing is believing? A beginners' guide to practical pitfalls in image acquisition." In: *Journal of Cell Biology* 172.1 (2006), pp. 9–18. ISSN: 00219525. DOI: 10.1083/jcb.200507103.

[19]   Claire M Brown. "Fluorescence microscopy - avoiding the pitfalls." In: *Journal of Cell Science* 120.10 (2007), pp. 1703–1705. ISSN: <null>. DOI: 10.1242/jcs.03433. URL: http://dx.doi.org/10.1242/jcs.03433{\%}5Cnpapers2://publication/uuid/759DE9EB-603A-4B32-B29C-24BD6059A59C.

[20]   Melanie M Frigault, Judith Lacoste, Jody L Swift, and Claire M Brown. "Live-cell microscopy - tips and tools." In: *Journal of cell science* 122.Pt 6 (2009), pp. 753–67. ISSN: 0021-9533. DOI: 10.1242/jcs.033837. URL: http://www.ncbi.nlm.nih.gov/pubmed/19261845.

[21]   Raghuveer Parthasarathy and Jay T Groves. "Optical techniques for imaging membrane topography." In: *Cell biochemistry and biophysics* 41 (2004), pp. 391–414. ISSN: 1085-9195. DOI: 10.1385/CBB:41:3:391.

[22]   Ai Ping Zhu, Ning Fang, Mary B. Chan-Park, and Vincent Chan. "Adhesion contact dynamics of 3T3 fibroblasts on poly (lactide-co-glycolide acid) surface modified by photochemical immobilization of biomacromolecules." In: *Biomaterials* 27.12 (2006), pp. 2566–2576. ISSN: 01429612. DOI: 10.1016/j.biomaterials.2005.11.039.

[23]   King Lam Hui, Chenlu Wang, Brian Grooman, Jessica Wayt, and Arpita Upadhyaya. "Membrane Dynamics Correlate with Formation of Signaling Clusters during Cell Spreading." In: *Biophysical Journal* 102.7 (2012), pp. 1524–1533. ISSN: 00063495. DOI: 10.1016/j.bpj.2012.02.015. URL: http://linkinghub.elsevier.com/retrieve/pii/S0006349512002172.

[24]   A. S. G. Curtis. "A Study by Interference Reflection Microscopy." In: *Journal of Cell Biology* 20.1 (1964), pp. 199–215. ISSN: 0021-9525. DOI: 10.1083/jcb.20.2.199.

[25]   H Verschueren. "Interference reflection microscopy in cell biology: methodology and applications." In: *Journal of cell science* 75 (1985), pp. 279–301. ISSN: 0021-9533.

[26]   D Gingell, O S Heavens, and J S Mellor. "General electromagnetic theory of total internal reflection fluorescence: the quantitative basis for mapping cell-substratum topography." In: *Journal of cell science* 87 (Pt 5) (1987), pp. 677–93. ISSN: 0021-9533. URL: http://www.ncbi.nlm.nih.gov/pubmed/3667723.

[27]   Alexander W Peterson, Michael Halter, Alessandro Tona, Kiran Bhadriraju, and Anne L Plant. "Surface plasmon resonance imaging of cells and surface-associated fibronectin." In: *BMC cell biology* 10 (2009), p. 16. ISSN: 1471-2121. DOI: 10.1186/1471-2121-10-16.

[28]   Victor Yashunsky, Vladislav Lirtsman, Michael Golosovsky, Dan Davidov, and Benjamin Aroeti. "Real-time monitoring of epithelial cell-cell and cell-substrate interactions by infrared surface plasmon spectroscopy." In: *Biophysical Journal* 99.12 (2010), pp. 4028–4036. ISSN: 00063495. DOI: 10.1016/j.bpj.2010.10.017. URL: http://dx.doi.org/10.1016/j.bpj.2010.10.017.

[29] Wei Wang, Yunze Yang, Shaopeng Wang, Vinay J. Nagaraj, Qiang Liu, Jie Wu, and Nongjian Tao. "Label-free measuring and mapping of binding kinetics of membrane proteins in single living cells." In: *Nature Chemistry* 4.10 (2012), pp. 846–853. ISSN: 1755-4330. DOI: 10.1038/nchem.1434.

[30] Yunze Yang, Hui Yu, Xiaonan Shan, Wei Wang, Xianwei Liu, Shaopeng Wang, and Nongjian Tao. "Label-Free Tracking of Single Organelle Transportation in Cells with Nanometer Precision Using a Plasmonic Imaging Technique." In: *Small* (2015), n/a–n/a. ISSN: 16136810. DOI: 10.1002/smll.201403016. URL: http://doi.wiley.com/10.1002/smll.201403016.

[31] Stefan a Meyer, Eric C Le Ru, and Pablo G Etchegoin. "Combining surface plasmon resonance (SPR) spectroscopy with surface-enhanced Raman scattering (SERS)." In: *Analytical chemistry* 83.6 (2011), pp. 2337–44. ISSN: 1520-6882. DOI: 10.1021/ac103273r. URL: http://www.ncbi.nlm.nih.gov/pubmed/21322587.

[32] Stefan a. Meyer, Baptiste Auguié, Eric C. Le Ru, and Pablo G. Etchegoin. "Combined SPR and SERS microscopy in the Kretschmann configuration." In: *Journal of Physical Chemistry A* 116.3 (2012), pp. 1000–1007. ISSN: 10895639. DOI: 10.1021/jp2107507.

[33] B. P. Nelson, T. E. Grimsrud, M. R. Liles, R. M. Goodman, and R. M. Corn. "Surface plasmon resonance imaging measurements of DNA and RNA hybridization adsorption onto DNA microarrays." In: *Analytical Chemistry* 73.1 (2001), pp. 1–7.

[34] Lauren K. Wolf, Dominic E. Fullenkamp, and Rosina M. Georgiadis. "Quantitative angle-resolved SPR imaging of DNA-DNA and DNA-drug kinetics." In: *Journal of the American Chemical Society* 127.49 (2005), pp. 17453–17459.

[35] Jennifer S. Shumaker-Parry, M. Hadi Zareie, Ruedi Aebersold, and Charles T. Campbell. "Microspotting Streptavidin and Double-Stranded DNA Arrays on Gold for High-Throughput Studies of Protein-DNA Interactions by Surface Plasmon Resonance Microscopy." In: *Analytical Chemistry* 76.4 (2004), pp. 918–929.

[36] Chi Lok Wong and Malini Olivo. "Surface Plasmon Resonance Imaging Sensors: A Review." In: *Plasmonics* 9.4 (2014), pp. 809–824. ISSN: 1557-1955. DOI: 10.1007/s11468-013-9662-3. URL: http://link.springer.com/10.1007/s11468-013-9662-3.

[37] B Rothenhäusler and W Knoll. "Surface plasmon microscopy." In: *Nature* 339.6221 (1988), pp. 186–186. ISSN: 0028-0836. URL: http://www.nature.com/nature/journal/v332/n6165/abs/332615a0.html.

[38] E. Yeatman and E. A. Ash. "Surface plasmon microscopy." In: *Electronics Letters* 23.20 (1987), pp. 1091–1092. URL: http://www.nature.com/nature/journal/v332/n6165/abs/332615a0.html.

[39]   CE Jordan, AG Frutos, AJ Thiel, and RM Corn. "Surface plasmon resonance imaging measurements of DNA hybridization adsorption and streptavidin/DNA multilayer formation at chemically modified gold surfaces." In: *Analytical Chemistry* 69.24 (1997), pp. 4939–4947. URL: http://pubs.acs.org/doi/abs/10.1021/ac9709763.

[40]   Bryce P. Nelson, Anthony G. Frutos, Jennifer M. Brockman, and Robert M. Corn. "Near-Infrared Surface Plasmon Resonance Measurements of Ultrathin Films. 1. Angle Shift and SPR Imaging Experiments." In: *Analytical Chemistry* 71.18 (1999), pp. 3928–3934. ISSN: 0003-2700. DOI: 10.1021/ac990517x. URL: http://pubs.acs.org/doi/abs/10.1021/ac990517x.

[41]   AV Kabashin and PI Nikitin. "Interferometer based on a surface-plasmon resonance for sensor applications." In: *Quantum Electronics* 653 (1997), pp. 653–655. URL: http://www.turpion.org/php/paper.phtml?journal{_}id=qe{\&}paper{_}id=1013.

[42]   H.P. Ho and W.W. Lam. "Application of differential phase measurement technique to surface plasmon resonance sensors." In: *Sensors and Actuators B: Chemical* 96.3 (2003), pp. 554–559. ISSN: 09254005. DOI: 10.1016/S0925-4005(03)00638-5. URL: http://linkinghub.elsevier.com/retrieve/pii/S0925400503006385.

[43]   Y D Su, S J Chen, and T L Yeh. "Common-path phase-shift interferometry surface plasmon resonance imaging system." In: *Optics letters* 30.12 (2005), pp. 1488–90. ISSN: 0146-9592. URL: http://www.ncbi.nlm.nih.gov/pubmed/16007783.

[44]   Yu Xinglong, Wang Dingxin, Wei Xing, Ding Xiang, Liao Wei, and Zhao Xinsheng. "A surface plasmon resonance imaging interferometry for protein micro-array detection." In: *Sensors and Actuators B: Chemical* 108.1-2 (2005), pp. 765–771. ISSN: 09254005. DOI: 10.1016/j.snb.2004.12.089. URL: http://linkinghub.elsevier.com/retrieve/pii/S0925400505000420.

[45]   Lei Xu, Xiaoyuan Peng, Jianmin Miao, and Anand K. Asundi. "Studies of Digital Microscopic Holography with Applications to Microstructure Testing." In: *Applied Optics* 40.28 (2001), p. 5046. ISSN: 0003-6935. DOI: 10.1364/AO.40.005046. URL: http://ao.osa.org/abstract.cfm?URI=ao-40-28-5046.

[46]   Björn Kemper and Gert von Bally. "Digital holographic microscopy for live cell applications and technical inspection." In: *Applied Optics* 47.4 (2008), A52. ISSN: 0003-6935. DOI: 10.1364/AO.47.000A52. URL: http://ao.osa.org/abstract.cfm?URI=ao-47-4-A52.

[47]   Jonas Kühn, Frédéric Montfort, Tristan Colomb, Benjamin Rappaz, Corinne Moratal, Nicolas Pavillon, Pierre Marquet, and Christian Depeursinge. "Submicrometer tomography of cells by multiple-wavelength digital holographic microscopy in reflection." In: *Optics Letters* 34.5 (2009), p. 653. ISSN: 0146-9592. DOI: 10.1364/OL.34.000653. URL: http://ol.osa.org/abstract.cfm?URI=ol-34-5-653.

[48] Yann Cotte, Fatih Toy, Pascal Jourdain, Nicolas Pavillon, Daniel Boss, Pierre Magistretti, Pierre Marquet, and Christian Depeursinge. "Marker-free phase nanoscopy." In: *Nature Photonics* 7.2 (2013), pp. 113–117. ISSN: 1749-4885. DOI: 10.1038/nphoton. 2012.329. URL: http://www.nature.com/doifinder/10.1038/nphoton.2012.329.

[49] Vittorio Bianco, Francesco Merola, Lisa Miccio, Pasquale Memmolo, Oriella Gennari, Melania Paturzo, Paolo Antonio Netti, and Pietro Ferraro. "Imaging adherent cells in the microfluidic channel hidden by flowing RBCs as occluding objects by a holographic method." In: *Lab on a chip* 14.14 (2014), pp. 2499–504. ISSN: 1473-0189. DOI: 10.1039/c4lc00290c. URL: http://www.ncbi.nlm.nih.gov/pubmed/24852283.

[50] G Coppola, P Ferraro, M Iodice, S De Nicola, a Finizio, and S Grilli. "A digital holographic microscope for complete characterization of microelectromechanical systems." In: *Measurement Science and Technology* 15.3 (2004), pp. 529–539. ISSN: 0957-0233. DOI: 10.1088/0957-0233/15/3/005. URL: http://stacks.iop.org/0957-0233/15/i=3/a=005?key=crossref.8d629f8115e3b17286f782e0a47ed802.

[51] WM Ash and MK Kim. "Digital holography of total internal reflection." In: *Optics express* 16.13 (2008), pp. 9811–9820. URL: http://www.opticsinfobase.org/abstract.cfm?uri=oe-16-13-9811.

[52] Alejandro Calabuig, Marcella Matrecano, Melania Paturzo, and Pietro Ferraro. "Common-path configuration in total internal reflection digital holography microscopy." In: *Optics letters* 39.8 (2014), pp. 2471–4. ISSN: 1539-4794. URL: http://www.ncbi.nlm.nih.gov/pubmed/24979021.

[53] Cuiying Hu, Jingang Zhong, and Jiawen Weng. "Digital holographic microscopy by use of surface plasmon resonance for imaging of cell membranes." In: *Journal of biomedical optics* 15.5 (2011), p. 56015. ISSN: 1560-2281. DOI: 10.1117/1.3497564. URL: http://www.ncbi.nlm.nih.gov/pubmed/21054109.

[54] Loïc Laplatine, Loïc Leroy, Roberto Calemczuk, Dieudonné Baganizi, Patrice N. Marche, Yoann Roupioz, and Thierry Livache. "Spatial resolution in prism-based surface plasmon resonance microscopy." In: *Optics Express* 22.19 (2014), p. 22771. ISSN: 1094-4087. DOI: 10.1364/OE.22.022771. URL: http://www.opticsinfobase.org/abstract.cfm?URI=oe-22-19-22771.

[55] D Gabor. *A new microscopic principle.* 1948. DOI: 10.1038/161777a0.

[56] D Gabor. "Microscopy by Reconstructed Wave Fronts: II." In: *Proceedings of the Physical Society. Section B* 64.6 (1951), pp. 449–469. ISSN: 0370-1301. DOI: 10.1088/0370-1301/64/6/301. URL: http://www.scopus.com/inward/record.url?eid=2-s2.0-36149056147{\&}partnerID=40{\&}md5=e26e7615d9f3c421032401f5cf196673{\%}5Cnhttp://iopscience.iop.org/0370-1301/64/6/301/pdf/0370-1301{_}64{_}6{_}301.pdf{\%}5Cnhttp://www.ncbi.nlm.nih.gov/pubmed/14775684{\%}5Cnhttp://stacks.iop.

[57]   Emmett N Leith and Juris Upatnieks. "Reconstructed wavefronts and communi-
       cation theory." In: *JOSA* 52.10 (1962), pp. 1123–1130.

[58]   Joseph W Goodman and RW Lawrence. "Digital image formation from electroni-
       cally detected holograms." In: *Applied physics letters* 11.3 (1967), pp. 77–79.

[59]   M. A. Kronrod, N. S. Merzlyakov, and L. P. Yaroslavskii. "Reconstruction of a Holo-
       gram with a Computer." In: *Soviet Physics Technical Physics* 17 (Aug. 1972), p. 333.

[60]   Levent Onural and Peter D Scott. "Digital decoding of in-line holograms." In: *Op-
       tical engineering* 26.11 (1987), pp. 261124–261124.

[61]   G Liu and PD Scott. "Phase retrieval and twin-image elimination for in-line Fres-
       nel holograms." In: *JOSA A* 4.1 (1987), pp. 159–165.

[62]   James R Fienup. "Phase retrieval algorithms: a comparison." In: *Applied optics*
       21.15 (1982), pp. 2758–2769.

[63]   Levent Onural and Mehmet Tankut Özgen. "Extraction of three-dimensional object-
       location information directly from in-line holograms using Wigner analysis." In:
       JOSA A 9.2 (1992), pp. 252–260.

[64]   Ulf Schnars and Werner Jüptner. "Direct recording of holograms by a CCD target
       and numerical reconstruction." In: *Applied optics* 33.2 (1994), pp. 179–181.

[65]   Fook Chiong Cheong, Bhaskar Jyoti Krishnatreya, and David G Grier. "Strategies
       for three-dimensional particle tracking with holographic video microscopy." In:
       Optics express 18.13 (2010), pp. 13563–13573.

[66]   Pietro Ferraro, Sergio De Nicola, Giuseppe Coppola, Andrea Finizio, Domenico
       Alfieri, and Giovanni Pierattini. "Controlling image size as a function of distance
       and wavelength in Fresnel-transform reconstruction of digital holograms." In: *Op-
       tics Letters* 29.8 (2004), pp. 854–856.

[67]   Christopher J Mann, Lingfeng Yu, Chun-Min Lo, and Myung K Kim. "High-resolution
       quantitative phase-contrast microscopy by digital holography." In: *Optics Express*
       13.22 (2005), pp. 8693–8698.

[68]   Daniel Carl, Björn Kemper, Günther Wernicke, and Gert von Bally. "Parameter-
       optimized digital holographic microscope for high-resolution living-cell analysis."
       In: *Applied optics* 43.36 (2004), pp. 6536–6544.

[69]   Sungkyu Seo, Ting-Wei Su, Anthony Erlinger, and Aydogan Ozcan. "Multi-color
       LUCAS: Lensfree on-chip cytometry using tunable monochromatic illumination
       and digital noise reduction." In: *Cellular and Molecular Bioengineering* 1.2-3 (2008),
       p. 146.

[70] Pascal Picart and Julien Leval. "General theoretical formulation of image formation in digital Fresnel holography." In: *Journal of the Optical Society of America A* 25.7 (2008), p. 1744. ISSN: 1084-7529. DOI: 10.1364/JOSAA.25.001744. URL: https://www.osapublishing.org/abstract.cfm?URI=josaa-25-7-1744.

[71] Joseph W Goodman. *Introduction to Fourier optics.* Roberts and Company Publishers, 2005.

[72] Thomas M Kreis, Werner PO Jueptner, and Juergen Geldmacher. "Principles of digital holographic interferometry." In: *SPIE's International Symposium on Optical Science, Engineering, and Instrumentation.* International Society for Optics and Photonics. 1998, pp. 45–54.

[73] Jorge Garcia-Sucerquia, Wenbo Xu, Stephan K Jericho, Peter Klages, Manfred H Jericho, and H Jürgen Kreuzer. "Digital in-line holographic microscopy." In: (2006). ISSN: 0003-6935. DOI: 10.1364/AO.45.000836.

[74] Mohendra Roy, Dongmin Seo, Sangwoo Oh, Ji Woon Yang, and Sungkyu Seo. "A review of recent progress in lens-free imaging and sensing." In: *Biosensors and Bioelectronics* 88 (2017), pp. 130–143. ISSN: 18734235. DOI: 10.1016/j.bios.2016.07.115. URL: http://dx.doi.org/10.1016/j.bios.2016.07.115.

[75] E Cuche, P Marquet, and C Depeursinge. "Simultaneous amplitude-contrast and quantitative phase-contrast microscopy by numerical reconstruction of Fresnel off-axis holograms." In: *Applied optics* 38.34 (1999), pp. 6994–7001. ISSN: 0003-6935. DOI: 10.1364/AO.38.006994.

[76] Pietro Ferraro, Sergio De Nicola, Andrea Finizio, Giuseppe Coppola, Simonetta Grilli, Carlo Magro, and Giovanni Pierattini. "Compensation of the inherent wave front curvature in digital holographic coherent microscopy for quantitative phase-contrast imaging." In: *Applied Optics* 42.11 (2003), p. 1938. ISSN: 0003-6935. DOI: 10.1364/AO.42.001938. URL: https://www.osapublishing.org/abstract.cfm?URI=ao-42-11-1938.

[77] Tristan Colomb, Etienne Cuche, Florian Charrière, Jonas Kühn, Nicolas Aspert, Frédéric Montfort, Pierre Marquet, and Christian Depeursinge. "Automatic procedure for aberration compensation in digital holographic microscopy and applications to specimen shape compensation." In: *Applied optics* 45.5 (2006), pp. 851–863.

[78] Emilio Sánchez-Ortiga, Pietro Ferraro, Manuel Martínez-Corral, Genaro Saavedra, and Ana Doblas. "Digital holographic microscopy with pure-optical spherical phase compensation." In: *Journal of the Optical Society of America. A, Optics, image science, and vision* 28.7 (2011), pp. 1410–1417. ISSN: 1084-7529. DOI: 10.1364/JOSAA.28.001410.

[79] Sang Joon Lee Kyung Won Seo, Yung Seok Choi, Eun Seok Seo. "Aberration compensation for objective phase curvature in phase holographic microscopy: comment." In: *Optics letters* 37.3 (2012), p. 4976. ISSN: 1539-4794. DOI: 10.1364/OL.39.000417. URL: http://www.ncbi.nlm.nih.gov/pubmed/24487828.

[80] Ana Doblas, Emilio Sánchez-Ortiga, Manuel Martínez-Corral, Genaro Saavedra, Pedro Andrés, and Jorge Garcia-Sucerquia. "Shift-variant digital holographic microscopy: inaccuracies in quantitative phase imaging." In: *Opt. Lett.* 38.8 (2013), pp. 1352–1354. ISSN: 1539-4794. URL: http://ol.osa.org/abstract.cfm?URI=ol-38-8-1352.

[81] Manuel Martínez-Corral and Genaro Saavedra. "The resolution challenge in 3D optical microscopy." In: *Progress in Optics* 53 (2009), pp. 1–67.

[82] Sara Coppola et al. "Twofold Self-Assembling of Nanocrystals Into Nanocomposite Polymer." In: *IEEE Journal of Selected Topics in Quantum Electronics* 22.1 (2016), pp. 1–7. ISSN: 1077-260X. DOI: 10.1109/JSTQE.2015.2449657. URL: http://ieeexplore.ieee.org/document/7132694/.

[83] F Merola, M Paturzo, S Coppola, V Vespini, and P Ferraro. "Self-patterning of a polydimethylsiloxane microlens array on functionalized substrates and characterization by digital holography." In: *Journal of Micromechanics and Microengineering* 19.12 (2009), p. 125006.

[84] IA Grimaldi, S Coppola, F Loffredo, F Villani, C Minarini, V Vespini, L Miccio, S Grilli, and P Ferraro. "Printing of polymer microlenses by a pyroelectrohydrodynamic dispensing approach." In: *Optics letters* 37.13 (2012), pp. 2460–2462.

[85] Catherine P Whitby, Xun Bian, and Rossen Sedev. "Spontaneous liquid marble formation on packed porous beds." In: *Soft Matter* 8.44 (2012), pp. 11336–11342.

[86] George M Whitesides. "The origins and the future of microfluidics." In: *Nature* 442.7101 (2006), pp. 368–73. ISSN: 1476-4687. DOI: 10.1038/nature05058. URL: http://www.ncbi.nlm.nih.gov/pubmed/16871203.

[87] Jamil El-Ali, Peter K Sorger, and Klavs F Jensen. "Cells on chips." In: *Nature* 442.7101 (2006), pp. 403–411. ISSN: 0028-0836. DOI: 10.1038/nature05063.

[88] Paul Yager, Thayne Edwards, Elain Fu, Kristen Helton, Kjell Nelson, Milton R Tam, and Bernhard H Weigl. "Microfluidic diagnostic technologies for global public health." In: *Nature* 442.7101 (2006), pp. 412–418. ISSN: 0028-0836. DOI: 10.1038/nature05064. URL: http://www.nature.com/doifinder/10.1038/nature05064.

[89] Sangeeta N Bhatia and Donald E Ingber. "Microfluidic organs-on-chips." In: *Nat Biotech* 32.8 (2014), pp. 760–772. ISSN: 1087-0156. DOI: 10.1038/nbt.2989[doi]. arXiv: 1408.1149. URL: http://dx.doi.org/10.1038/nbt.2989{\%}0Ahttp://10.0.4.14/nbt.2989.

[90] Vittorio Bianco, Biagio Mandracchia, Valentina Marchesano, Vito Pagliarulo, Federico Olivieri, Melania Paturzo, and Pietro Ferraro. "Endowing a plain fluidic chip with micro-optics : a holographic microscope slide." In: *Light: Science Applications* (). DOI: 10.1038/lsa.2017.55.

[91] Daniel Axelrod. "Selective imaging of surface fluorescence with very high aperture microscope objectives." In: *Journal of biomedical optics* 6.1 (2001), pp. 6–13.

[92] Andrea L Stout and Daniel Axelrod. "Evanescent field excitation of fluorescence by epi-illumination microscopy." In: *Applied optics* 28.24 (1989), pp. 5237–5242.

[93] S Inoue, RA Knudson, M Goda, K Suzuki, C Nagano, N Okada, H Takahashi, K Ichie, M Iida, and K Yamanaka. "Centrifuge polarizing microscope. I. Rationale, design and instrument performance." In: *Journal of microscopy* 201.3 (2001), pp. 341–356.

[94] Jeffrey R Kuhn and Thomas D Pollard. "Real-time measurements of actin filament polymerization by total internal reflection fluorescence microscopy." In: *Biophysical journal* 88.2 (2005), pp. 1387–1402.

[95] Alexa L Mattheyses, Keith Shaw, and Daniel Axelrod. "Effective elimination of laser interference fringing in fluorescence microscopy by spinning azimuthal incidence angle." In: *Microscopy research and technique* 69.8 (2006), pp. 642–647.

[96] Alexa L Mattheyses and Daniel Axelrod. "Direct measurement of the evanescent field profile produced by objective-based total internal reflection fluorescence." In: *Journal of biomedical optics* 11.1 (2006), pp. 014006–014006.

[97] R Juskaitis and T Wilson. "A method for characterizing longitudinal chromatic aberration of microscope objectives using a confocal optical system." In: *Journal of microscopy* 195.1 (1999), pp. 17–22.

[98] Stefan W Hell, Pekka E Hänninen, Ari Kuusisto, Martin Schrader, and Erkki Soini. "Annular aperture two-photon excitation microscopy." In: *Optics communications* 117.1-2 (1995), pp. 20–24.

[99] Max; Born and Emil Wolf. *Principles Of Optics*. Ed. by Cambridge University Press. 7th. 2003.

[100] Sophocles J Orfanidis. *Electromagnetic Waves and Antennas*. Vol. 2. Rutgers U. 2004, pp. 313–321. ISBN: 9780750649476. DOI: 10.1016/B978-075064947-6/50011-3. arXiv: arXiv:1011.1669v3. URL: http://www.ece.rutgers.edu/{~}orfanidi/ewa/.

[101] Maia Brunstein, Maxime Teremetz, Karine Hérault, Christophe Tourain, and Martin Oheim. "Eliminating unwanted far-field excitation in objective-type TIRF. Part I. identifying sources of nonevanescent excitation light." In: *Biophysical journal* 106.5 (2014), pp. 1020–32. ISSN: 1542-0086. DOI: 10.1016/j.bpj.2013.12.049. URL: http://www.ncbi.nlm.nih.gov/pubmed/24606927.

[102] Biagio Mandracchia, Oriella Gennari, Valentina Marchesano, Melania Paturzo, and Pietro Ferraro. "Label free imaging of cell-substrate contacts by holographic total internal reflection microscopy." In: *Journal of Biophotonics* 8 (2016), pp. 1–8. ISSN: 1864063X. DOI: 10.1002/jbio.201600177. URL: http://doi.wiley.com/10.1002/jbio.201600177.

[103] R Carlsson, E Engvall, a Freeman, and E Ruoslahti. "Laminin and fibronectin in cell adhesion: enhanced adhesion of cells from regenerating liver to laminin." In: *Proceedings of the National Academy of Sciences of the United States of America* 78.4 (1981), pp. 2403–2406. ISSN: 0027-8424. DOI: 10.1073/pnas.78.4.2403.

[104] Elisabetta Ada Cavalcanti-Adam, Tova Volberg, Alexandre Micoulet, Horst Kessler, Benjamin Geiger, and Joachim Pius Spatz. "Cell spreading and focal adhesion dynamics are regulated by spacing of integrin ligands." In: *Biophysical journal* 92.8 (2007), pp. 2964–74. ISSN: 0006-3495. DOI: 10.1529/biophysj.106.089730. URL: http://www.sciencedirect.com/science/article/pii/S0006349507710998.

[105] Rui Chen, Van Duong Ta, and Han Dong Sun. "Single mode lasing from hybrid hemispherical microresonators." In: *Scientific reports* 2 (2012), p. 244. ISSN: 2045-2322. DOI: 10.1038/srep00244. URL: http://www.pubmedcentral.nih.gov/articlerender.fcgi?artid=3337539{\&}tool=pmcentrez{\&}rendertype=abstract.

[106] Damien Cuvelier, Manuel Thery, Yeh-Shiu Chu, Sylvie Dufour, Jean-Paul Thiery, Michel Bornens, Pierre Nassoy, and L Mahadevan. "The universal dynamics of cell spreading." In: *Curr Biol* 17.8 (2007), pp. 694–699. ISSN: 09609822. DOI: 10.1016/j.cub.2007.02.058. URL: http://www.hubmed.org/display.cgi?uids=17379524.

[107] Daniel; Mazia, Gerald; Schatten, and Winfield Sale. "Adhesion of cells to surfaces coated with polilysine." In: *Journal of Cell Biology* 66.3 (1975), pp. 198–200.

[108] Heinz Raether. *Surface plasmons on smooth surfaces.* Springer, 1988.

[109] Andreas Otto. "Excitation of nonradiative surface plasma waves in silver by the method of frustrated total reflection." In: *Zeitschrift für Physik* 216.4 (1968), pp. 398–410.

[110] Erwin Kretschmann and Heinz Raether. "Notizen: radiative decay of non radiative surface plasmons excited by light." In: *Zeitschrift für Naturforschung A* 23.12 (1968), pp. 2135–2136.

[111] Bo Liedberg and Pentti Tengvall. "Molecular gradients of ω-substituted alkanethiols on gold: preparation and characterization." In: *Langmuir* 11.10 (1995), pp. 3821–3827.

[112] Sophia Hober and Mathias Uhlén. "Human protein atlas and the use of microarray technologies." In: *Current opinion in biotechnology* 19.1 (2008), pp. 30–35.

[113]   Scott Marshall Mansfield and GS Kino. "Solid immersion microscope." In: *Applied physics letters* 57.24 (1990), pp. 2615–2616.

[114]   BD Terris, HJ Mamin, D Rugar, WR Studenmund, and GS Kino. "Near-field optical data storage using a solid immersion lens." In: *Applied Physics Letters* 65.4 (1994), pp. 388–390.

[115]   P.I Nikitin, a.N Grigorenko, a.a Beloglazov, M.V Valeiko, a.I Savchuk, O.a Savchuk, G Steiner, C Kuhne, a Huebner, and R Salzer. "Surface plasmon resonance interferometry for micro-array biosensing." In: *Sensors and Actuators A: Physical* 85.1-3 (2000), pp. 189–193. ISSN: 09244247. DOI: 10.1016/S0924-4247(00)00386-1. URL: http://linkinghub.elsevier.com/retrieve/pii/S0924424700003861.

[116]   Jong Seol Yuk, Hyun-Soo Kim, Jae-Wan Jung, Se-Hui Jung, Seung-Joon Lee, Woo Jin Kim, Jeong-A Han, Young-Myeong Kim, and Kwon-Soo Ha. "Analysis of protein interactions on protein arrays by a novel spectral surface plasmon resonance imaging." In: *Biosensors & bioelectronics* 21.8 (2006), pp. 1521–1528. ISSN: 0956-5663. DOI: 10.1016/j.bios.2005.07.009.

[117]   Jong Seol Yuk, Duk-Geun Hong, Hyo-Il Jung, and Kwon-Soo Ha. "Application of spectral SPR imaging for the surface analysis of C-reactive protein binding." In: *Sensors and Actuators B: Chemical* 119.2 (2006), pp. 673–675. ISSN: 09254005. DOI: 10.1016/j.snb.2006.01.031.

[118]   JM Brockman. "Surface plasmon resonance imaging measurements of ultrathin organic films." In: *Annual review of physical …* (2000), pp. 41–63. URL: http://www.annualreviews.org/doi/abs/10.1146/annurev.physchem.51.1.41.

[119]   EM Yeatman. "Resolution and sensitivity in surface plasmon microscopy and sensing." In: *Biosensors and Bioelectronics* 11.617 (1996). URL: http://www.sciencedirect.com/science/article/pii/0956566396832982.

[120]   B. Mandracchia, V. Pagliarulo, M. Paturzo, and P. Ferraro. "Surface plasmon resonance imaging by holographic enhanced mapping." In: *Analytical Chemistry* 87.8 (2015), pp. 4124–4128. ISSN: 15206882. DOI: 10.1021/acs.analchem.5b00095.

[121]   B. Mandracchia, V. Pagliarulo, M. Paturzo, and P. Ferraro. "Through-the-objective holographic surface plasmon resonance imaging for quantitative measurement of thin film thickness." In: *Progress in Biomedical Optics and Imaging - Proceedings of SPIE*. Vol. 9718. 2016. ISBN: 9781628419528. DOI: 10.1117/12.2218419.

[122]   Lingfeng Yu and Myung K Kim. "Wavelength-scanning digital interference holography for tomographic three-dimensional imaging by use of the angular spectrum method." In: *Optics letters* 30.16 (2005), pp. 2092–2094. ISSN: 0146-9592. DOI: 10.1364/OL.30.002092.

[123] Shiping Li and Jingang Zhong. "Simultaneous amplitude-contrast and phase-contrast surface plasmon resonance imaging by use of digital holography." In: *Biomedical optics express* 3.12 (2012), pp. 3190–3202. ISSN: 2156-7085. DOI: 10.1364/BOE.3.003190. URL: http://www.pubmedcentral.nih.gov/articlerender.fcgi?artid=3521296{\&}tool=pmcentrez{\&}rendertype=abstract.

[124] Jérôme Boulanger, Charles Gueudry, Daniel Münch, Bertrand Cinquin, Perrine Paul-Gilloteaux, Sabine Bardin, Christophe Guérin, Fabrice Senger, Laurent Blanchoin, and Jean Salamero. "Fast high-resolution 3D total internal reflection fluorescence microscopy by incidence angle scanning and azimuthal averaging." In: *Proceedings of the National Academy of Sciences of the United States of America* 111.48 (2014), pp. 17164–9. ISSN: 1091-6490. DOI: 10.1073/pnas.1414106111. arXiv: arXiv:1408.1149. URL: http://www.pubmedcentral.nih.gov/articlerender.fcgi?artid=4260613{\&}tool=pmcentrez{\&}rendertype=abstract.

[125] B P Olveczky, N Periasamy, and A S Verkman. "Mapping fluorophore distributions in three dimensions by quantitative multiple angle-total internal reflection fluorescence microscopy." In: *Biophysical journal* 73.5 (1997), pp. 2836–47. ISSN: 0006-3495. DOI: 10.1016/S0006-3495(97)78312-7. URL: http://www.sciencedirect.com/science/article/pii/S0006349597783127.

[126] K. Stock, R. Sailer, W. S L Strauss, M. Lyttek, R. Steiner, and H. Schneckenburger. "Variable-angle total internal reflection fluorescence microscopy (VA-TIRFM): Realization and application of a compact illumination device." In: *Journal of Microscopy* 211.1 (2003), pp. 19–29. ISSN: 00222720. DOI: 10.1046/j.1365-2818.2003.01200.x.

[127] Maia Brunstein, Karine Hérault, and Martin Oheim. "Eliminating unwanted far-field excitation in objective-type TIRF. Part II. Combined evanescent-wave excitation and supercritical-angle fluorescence detection improves optical sectioning." In: *Biophysical Journal* 106.5 (2014), pp. 1044–1056. ISSN: 00063495. DOI: 10.1016/j.bpj.2013.12.051.

[128] Philipp von Olshausen and Alexander Rohrbach. "Coherent total internal reflection dark-field microscopy: label-free imaging beyond the diffraction limit." In: *Optics Letters* 38.20 (2013), p. 4066. ISSN: 0146-9592. DOI: 10.1364/OL.38.004066. URL: http://www.opticsinfobase.org/abstract.cfm?URI=ol-38-20-4066.

ACKNOWLEDGMENTS